Cavity plasmonics

Exploring narrow-gap plasmonic coupled systems to boost, localize and exploit nanometric light-matter interactions

Marie-Elena Kleemann

Cavendish Laboratory
University of Cambridge

This dissertation is submitted for the degree of "Doctor of Philosophy"

Murray Edwards College

November 2018

“ Man sieht nur mit dem Herzen gut,
Das Wesentliche ist für die Augen unsichtbar.”

- Antoine de Saint-Exupéry

This thesis is dedicated to the memory of my beloved mum,
you truly saw the world with your heart.

Declaration

This dissertation is the result of my own work and includes nothing which is the outcome of work done in collaboration except as declared in the Preface and specified in the text. It is not substantially the same as any that I have submitted, or, is being concurrently submitted for a degree or diploma or other qualification at the University of Cambridge or any other University or similar institution except as declared in the Preface and specified in the text. I further state that no substantial part of my dissertation has already been submitted, or, is being concurrently submitted for any such degree, diploma or other qualification at the University of Cambridge or any other University or similar institution except as declared in the Preface and specified in the text. It does not exceed the prescribed word limit for the relevant Degree Committee.
Cambridge, 02. November 2018

Marie-Elena Kleemann

Abstract

Cavity Plasmonics - Exploring narrow-gap plasmonic coupled systems to boost, localize and exploit nanometric light-matter interactions. **Marie-Elena Kleemann**

The core of this thesis explores the optical response and tuneability of plasmonic cavities. At its heart stands the nanoparticle on mirror construct (NPoM) -a robust plasmonic cavity formed via self-assembly. It consists of a nanoparticle placed on top of an underlying metal substrate separated by a nanometre thin spacer material. Plasmonic cavities have the ability to confine light beyond the diffraction limit via collective charge oscillations at dielectric-metal interface.

This thesis explores different ways to boost, localize and exploit nanometric light-matter interactions in the NPoM configuration. Due to their large field enhancement reaching values of the order of 10^4 and mode volumes as small as 40 nm^3 they form a versatile sensing platform. A custom-built polarization dark-field microscope is used to probe the morphology of the NPoM cavities on sub-nanometre length scales. Comparing the experimental results to boundary element method (BEM) simulations the NPoM system is fully characterized and the influence of the cavity morphology and faceting of the NPoM is investigated. A spectral splitting in the polarization signature of narrow gap systems ($<$1 nm) is directly related to the asymmetry and orientation of the plasmonic cavity, revealing its orientation and asymmetry which is otherwise inaccessible for conventional imaging techniques.

Furthermore, laser irradiation is employed to induce atomistic re-sculpturing processes of the cavity morphology, actively tuning the plasmonic modes. Two regimes of growth are identified: facet growth using hard spacer materials and conductive bridging using soft or porous spacer materials. The latter is used to monitor the controlled formation of conductive bridges in memristive devices. Finally, incorporating mono- and multi-layers of 2D materials into the plasmonic cavities, light-matter interaction is studied on the nanoscale. Stable room-temperature excitons of WSe_2 allow the strong-coupling regime to be reached in ambient conditions. Exploiting the large field enhancement of the NPoM cavity and tuning its plasmon modes over the exciton resonance reveals the typical anti-crossing signature of a strongly coupled system. This combination of ultra-small mode volumes of plasmonic cavities and large coupling strength of 2D materials offers a promising route to realistic exciton devices and allows a glimpse into the quantum world at room temperature.

List of Publications

1. M.-E. Kleemann, R. Chikkaraddy, E. M. Alexeev, D. Kos, C. Carnegie, W. Deacon, A. Casalis De Pury, C. Grosse, B De Nijs, J. Mertens, A. I. Tartakovskii, and J. J. Baumberg. Strong-coupling of WSe 2 in ultra-compact plasmonic nanocavities at room temperature. Nature Communications, 8(1), 2017

2. J. Mertens, M.-E. Kleemann, R. Chikkaraddy, Prineha Narang, and J. J. Baumberg. How Light Is Emitted by Plasmonic Metals. Nano Letters, 17(4), 2017

3. M.-E. Kleemann, J. Mertens, X. Zheng, S. Cormier, V. Turek, F. Benz, R. Chikkaraddy, W. Deacon, A. Lombardi, V. V. Moshchalkov, G. A.E. Vandenbosch, and J. J. Baumberg. Revealing Nanostructures through Plasmon Polarimetry. ACS Nano, 11(1), 2017

4. R. Chikkaraddy, X. Zheng, F. Benz, L. J. Brooks, B. de Nijs, C. Carnegie, M.-E. Kleemann, J. Mertens, R. W. Bowman, Guy A. E. Vandenbosch, V. V. Moshchalkov, and J. J. Baumberg. How Ultranarrow Gap Symmetries Control Plasmonic Nanocavity Modes: From Cubes to Spheres in the Nanoparticle-on- Mirror. ACS Photonics, 4(3), 2017

5. W. M. Deacon, A. Lombardi, F. Benz, Y. del Valle-Inclan Redondo, R. Chikkaraddy, B. de Nijs, M.-E. Kleemann, J. Mertens, and J. J. Baumberg. Interrogating Nano-junctions using Ultra-confined Acousto-Plasmonic Coupling. Phys. Rev. Lett. 119(2), 2017

6. J. Mertens, A. Demetriadou, R. W. Bowman, F. Benz, M.-E. Kleemann, C. Tserkezis, Y. Shi, H. Y. Yang, O. Hess, J. Aizpurua, and J. J. Baumberg. Tracking Optical Welding through Groove Modes in Plasmonic Nanocavities. Nano Lett., 16(9), 2016

7. M.-E. Kleemann, A. Salmon, A. Demetriadou, W. M. Deacon, C. Carnegie, M. Kamp, B. de Nijs, J.J. Baumberg, Filling Nanogaps with light: Controlled light-induced bridge formation in plasmonic dimers (*in preparation*)

8. B. de Nijs, C. Carnegie, I. Szabo, D.-B. Grys,R. Chikkaraddy, M. Kamp, S. Barrow, C. Readman, M.-E. Kleemann, O. Scherman, E. Rosta, Edina, J.J. Baumberg Inhibiting Analyte "Theft" in SERS Substrates: Quantitative sub-Nanomolar Drug Detection (*sumbitted*)

Acknowledgment

My PhD has been an exciting journey with many ups and downs. I would not have made it through the downs and I most definitely would not have enjoyed the ups as much without the support of countless people. First and foremost, I would like to thank my supervisor Jeremy Baumberg for giving me the opportunity to take part in his research group. His guidance, encouragement as well as endless enthusiasm and curiosity for science has been a tremendous help during my PhD. With his open minded mentality and easy going character he created a working environment that provided a space for many fruitful discussions and made hard work in the lab enjoyable. It has been a great privilege to be able to benefit from all those never ending ideas that he came up with and I have learned so much more than I could ever write down within this thesis.

My gratitude goes to Will Deacon, who was there from day one to help me make it through my PhD, Cloudy Carneigie, Yago Valle-Inclan Redondo and Rohit Chikkaraddy who always had time for discussions either scientifically or many other topics. I am also grateful to Giuliana DiMartino, Sean Cormier, Dean Kos, Junyang Huang, Bart de Nijs, Marlous Kamp, Andrew Salmon and Chris Grosse for the many inspiring discussions as well as endless hours in the lab together. A special thanks goes to Jan Mertens, Felix Benz, Alexander Dreismann, Anna Lombardi, Hamid Ohadi and Richard Bowman who helped me to get started with my PhD when I first joined the group. Last but not least I would like to thank Charlie Readman, Orr Beer, Ana Andres-Arroyo, Alexander Casalis de Pury, Phillip Köehler, Vlad Turek, Jack Griffiths, Demelza Wright, Ilja Manyakin, David-Benjamin Grys Omid Siddiqui, for the great atmosphere in the group, the fun lunchtimes and the many more joyful hours outside of work.

I would like to express my special thanks to all my collaborations. I extremely enjoyed working with Xuezhi Zheng (KU Leuven), Sasha Tartarkovski and Evgeny Alexeev (University of Sheffield), Angela Demetriadou (Univeristy of Bermingham) and Prineha Narang (Harvard University).

I greatly appreciate the constant support of our amazing group secretary, Angela Campbell. Her support was invaluable. Many thanks to computer officer Colin Edwards and our lab technician Anthony Barnett for help with any lab-related or gardening issues, and just for a really great company.

I am deeply grateful to my family, especially my siblings Gregor and Katharina for their constant support through out this journey and for never stopping to believe in me. I would not have made it without you. Finally, I would like to thank my mum Monika. You

are my constant inspiration in both science and life. If I have ever achieved anything, it is you who should take the credit for it.

Contents

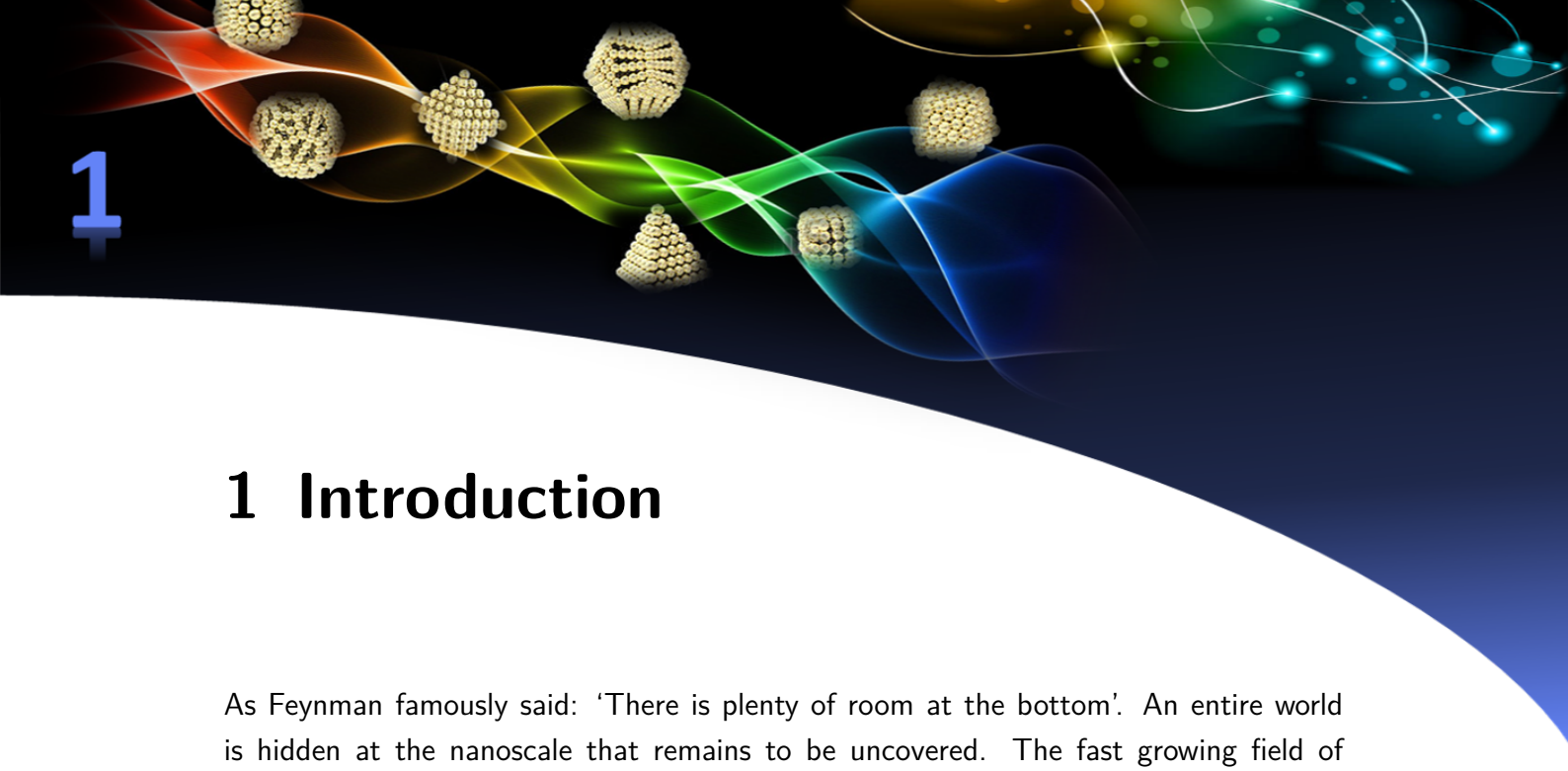

1 Introduction

As Feynman famously said: 'There is plenty of room at the bottom'. An entire world is hidden at the nanoscale that remains to be uncovered. The fast growing field of nanophotonics seeks to unravel some of it's secrets. A major challenge in the field is the difficulty to 'see' at these scales. Typically visible light is used to influence and image matter on much larger scales than the dimension given by its wavelength. Familiar effects such as reflection, transmission, absorption and scattering define the way we perceive the world. To better perceive the nanoworld, where dimensions are much smaller than the wavelength of light, new ways to localize, enhance and control light at those scales are needed.

Noble metal nanostructures are promising examples to gain control over light-matter interactions way below the diffraction limit. When light hits a metallic nanoparticle surface it induces resonant charge oscillations of the free electrons at the surface. This effect is called 'plasmon resonance' and builds the foundation of an entire field within nanophotonics. The resonance condition is strongly influenced by the material properties as well as the surrounding environment. Furthermore, it is accompanied by a large field enhancement at the surface of the nanoparticle. While this local field enhancement can be tailored by changing the size or shape of the nanoparticle, highest field enhancements are expected for plasmonic coupled structures, where the strength of interaction and field enhancement is set by the distance between two metal nanocomponents.

The strongly enhanced fields can be used to dramatically amplify a range of phenomena involving optical absorption and re-radiation and therefore open up unexplored opportunities for nanometric sensing applications and imaging techniques with atomic resolution. The reliable fabrication of such plasmonic coupled systems with nanometer gap distances has proven to be rather challenging and a promising version is given by the nanoparticle on mirror geometry (NPoM). The NPoM consists of a gold nanoparticle placed on top of a gold substrate with a spacer layer sandwiched in between. The gap enclosed between the nanoparticle and the induced image charge in the underlaying mirror acts as a plasmonic cavity, enhancing light-matter interactions at the nanoscale.

Using plasmonic cavities to explore different ways to boost, localize and exploit nanometric light-matter interactions is the central questions of this thesis.
A polarization dark-field microscope was developed to probe plasmonic nanostructures with atomistic resolution and in real time. The influence of cavity morphology and faceting, surrounding environment and spacer material of NPoMs was investigated experimentally. A characteristic polarization signature of narrow gap systems ($<$1 nm) was found to be directly related to the asymmetry and orientation of the plasmonic cavity hidden underneath the nanoparticle and inaccessible for conventional imaging techniques. Comparison to boundary element simulations (BEM) two sets of plasmonic modes were identified: tightly confined cavity modes and radiative antenna modes.
The high sensitivity to atomic scale morphological changes of the cavity was then used to monitor light-induced reconstruction processes in real-time. Two regimes were identified: a regime of facet growth, typically seen for "hard spacers", such as WSe_2 and a conductive bridging regime, for molecular "soft spacers".
Finally the large field enhancement of plasmonic cavities was exploited to achieve room temperature strong coupling by incorporating multi layers of WSe_2 into NPoM constructs.

Thesis Outline

Addressing the fundamental questions of light-matter interaction in plasmonic cavities the thesis is divided here in the following way:
Chapters 2 and **3** summarize the fundamental properties of light-matter interactions and the experimental means to study these on the nanoscale. Starting with a classical approach, electric field enhancements, plasmonic localization and coupling are introduced and discussed. Optical cavities, in particular plasmonic cavities, which are used to boost light-matter interactions are reviewed and the different regimes of light-matter interaction are derived. A brief introduction to atomically thin materials used as a spacer material for plasmonic cavities is provided. The experimental sections centre around the development of dark-field microscopy as a non-invasive imaging technique to study plasmonic nanostructures in real-time and with nanometer resolution. The last part of this chapter describes the numerical methods and sample preparation methods used within this thesis.
In **Chapter 4** plasmonic coupled systems are investigated. A brief overview of fabrication methods that yield controlled sub-nanometer gap systems is given and the nanoparticle on mirror geometry (NPoM) is introduced. The fundamental optical properties of NPoM constructs are discussed and the influence of nanoparticle size, refractive index and gap distance are characterized systematically by numerical simulations and measured dark-field scattering spectra. The concept of plasmonic coupling between spherical nanopar-

ticles is extended by nanoparticle faceting and its influence on the optical properties are discussed in depth.

In **Chapter 5** the effect of nanoparticle faceting is explored experimentally using polarization dependent dark-field scattering. A complex interplay of highly confined cavity modes and radiative antenna modes is found, which reveals the cavity morphology hidden underneath the nanoparticle. As these modes are set by geometry of the NPoM constructs and highly sensitive to changes in the morphology **Chapter 6** explores the tuneability of the system. Ultra violet (UV) laser irradiation is used to cause atomistic restructuring of the plasmonic cavity, tuning its optical response. Different spacer materials are studied showing large effects on the restructuring and facet growth dynamics during laser irradiation.

In **Chapter 7** the tuenablity and exquisite field enhancement offered by plasmonic cavities are combined to reach the regime of strong light-matter coupling. Incorporating multilayer WSe_2 stacks with stable excitons inside the plasmonic cavity with mode volumes as small as 40 nm^3, room-temperature strong-coupling is achieved. The cavity resonance is tuned by UV laser irradiation to allow for optimal coupling and the typical spectral signature of an anti-crossing in the dispersion is revealed.

Finally, **Chapter 8** summarizes the findings of the previous chapters and gives an outlook on future experiments targeted to facilitate plasmon-mediated re-sculpturing processes and all optical switching.

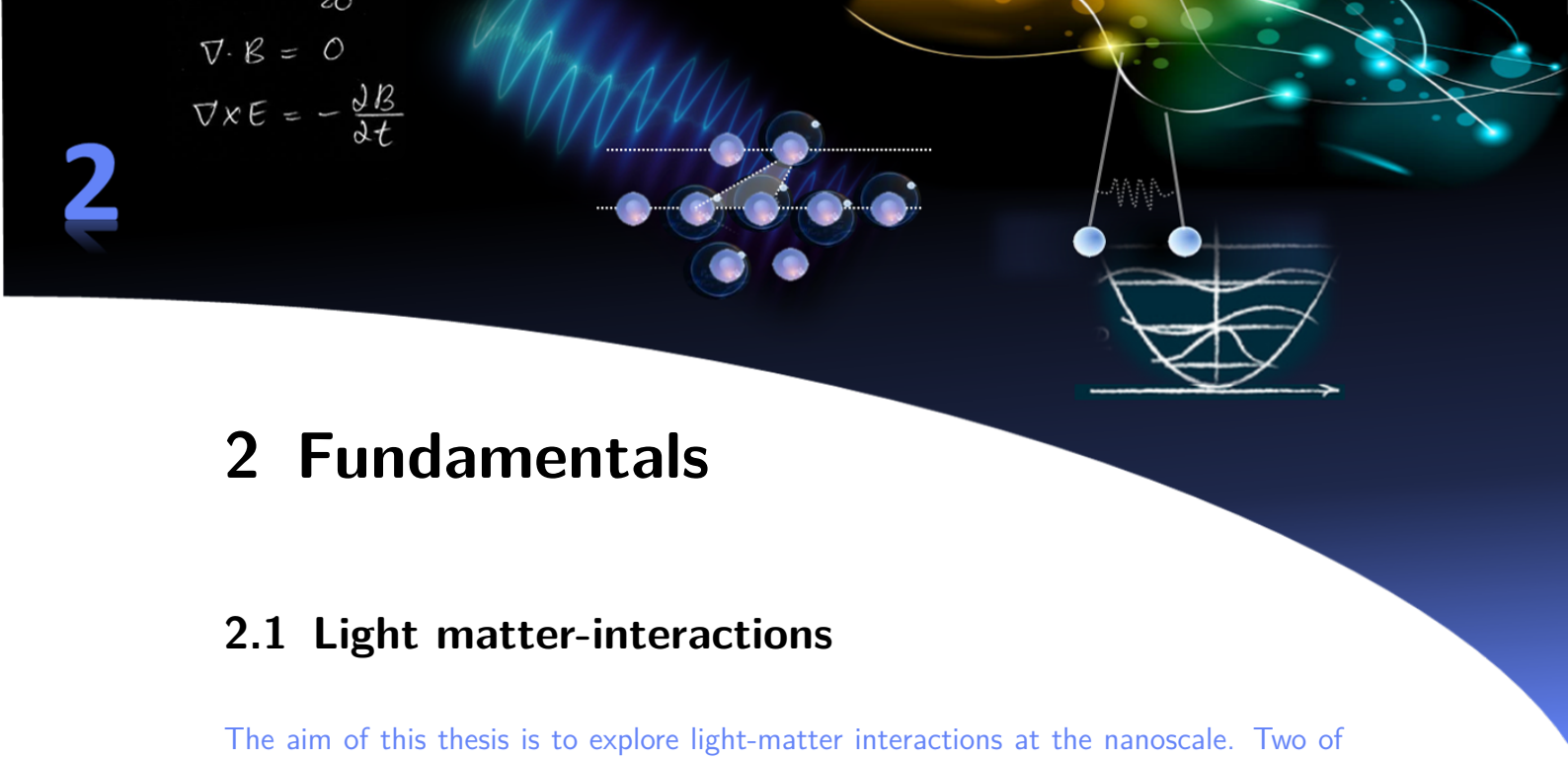

2 Fundamentals

2.1 Light matter-interactions

The aim of this thesis is to explore light-matter interactions at the nanoscale. Two of the key questions that need to be addressed before diving into all the fascinating phenomena at the nanoscale in depth, are how light behaves at those length scales and how it can be confined below the diffraction limit. Other important issues to understand are the physical consequences of strongly confined light. These questions and the unique properties of plasmonic metals that enable high field confinement will be discussed in the following chapter.

Using Maxwell equations as a classical framework, the fundamental equations describing light-matter interactions are derived. Based on the Drude-model, which describes the optical properties of metals, the light-matter interaction for plasmonic metals and specifically for plasmonic nanostructures is discussed. The framework is then extended to describe plasmonic coupling and enhancement.
In order to understand the limits of light-matter interactions, the transition from the weak to the strong coupling regime is revised. A classical description of two harmonic oscillators is introduced to define key parameters of the strong coupling regime.

2.1.1 Maxwell Equations

The four Maxwell equations are the fundamental equations of light-matter interactions in the classical regime. They describe the interaction of electromagnetic waves with matter[1]:

$$\nabla \cdot \vec{D} = \rho_{ext} \qquad \text{Coulomb's Law} \qquad (2.1)$$

$$\nabla \cdot \vec{B} = 0 \qquad \text{Gauss's Law} \qquad (2.2)$$

$$\nabla \times \vec{E} = -\partial_t \ \vec{B} \qquad \text{Faradays's Law} \qquad (2.3)$$

$$\nabla \times \vec{H} = \partial_t \ \vec{D} + \vec{j}_{ext} \qquad \text{Ampere's Law.} \qquad (2.4)$$

The vector fields $\vec{E}$ (electrical field), $\vec{D}$ (dielectric displacement), $\vec{B}$ (magnetic induction), $\vec{H}$ (magnetic field) as well as the scalar entities ρ_{ext} (external charge density) and $\vec{j}_{ext}$ (external current density) make up the fundamental of electrodynamics in vacuum.

Substituting equation (2.2) in (2.3) one obtains a general expression for propagating electromagnetic waves in vacuum:

$$\nabla^2 \vec{E} - \varepsilon\mu \frac{\partial^2}{\partial t^2} \vec{E} = 0 \qquad (2.5)$$

A possible solution of this wave equation is a harmonic plane wave:

$$\vec{E} = \vec{E}_0 e^{-i(\vec{k}\cdot\vec{r} - \omega t)} \qquad (2.6)$$

with $\vec{E}_0$ defining the amplitude and oscillation direction and $\vec{k}$ the propagation direction. Inserting the plane wave solution (2.6) into the wave equation results in the Helmholz equation:

$$\nabla^2 \vec{E} + k^2 \vec{E} = 0. \qquad (2.7)$$

The presence of matter changes the electromagnetic fields drastically. This is taken into account by including the magnetisation $\vec{M}$ and polarisation $\vec{P}$[1] .

$$\vec{D} = \varepsilon_0 \vec{E} + \vec{P}, \qquad \text{Polarisation} \qquad (2.8)$$

$$\vec{H} = \frac{1}{\mu_0} \vec{B} - \vec{M}. \qquad \text{Magnetisation} \qquad (2.9)$$

where μ_0 and ε_0 are the magnetic permeability and the electric permittivity in vacuum. $\vec{P}(\omega)$ and $\vec{M}(\omega)$ are each frequency-dependent functions of the induced currents and

charges caused by incident electromagnetic fields. For linear isotropic and homogeneous media the material equations (2.8) and (2.9) can be simplified as:

$$\vec{D} = \varepsilon_0 \varepsilon(\omega)\vec{E}, \tag{2.10}$$

$$\vec{H} = \frac{1}{\mu_0 \mu}\vec{B}. \tag{2.11}$$

Here μ is the permittivity of the medium and is set to 1 in non-magnetic media for all this thesis. ε is the dielectric permittivity and generally depends on frequency ω and space r. The dielectric function directly links the macroscopic polarisation $\vec{P}$ to the electromagnetic field and therefore contains the response of the medium. In general ε and μ are tensors, but in typical linear, isotropic and homogeneous media they simplify to scalar functions. Furthermore, in many cases, where the incident wavelength is larger than the characteristic size of the medium (such as the unit cell), "local-effects" resulting in a spatial dispersion can be neglected. As a result the response of the medium is dominated by the frequency dependence[2]

$$\varepsilon(\omega) = \varepsilon_1(\omega) + i\varepsilon_2(\omega) \tag{2.12}$$

In general the dielectric function is a complex function, where the imaginary part $(i\varepsilon(\omega))$ takes into account material absorption and losses. It therefore links to the reflection and transmission properties of a medium as followed $n(\omega) = \sqrt{\varepsilon}$:

$$\varepsilon_1(\omega) = n^2 - \kappa^2, \tag{2.13}$$

$$\varepsilon_2(\omega) = 2n\kappa. \tag{2.14}$$

with κ, n being the extinction coefficient and refractive index. The absorption coefficient $A(\omega) = 2\kappa/c$ is further linked to the the Lambert Beer law:

$$I(z) = I_0 \exp(-A(\omega)z) = I_0 \exp\left(-\frac{2\kappa(\omega)z}{c}\right), \tag{2.15}$$

which is widely used to identify molecular properties. In most cases the dielectric function is a non-trivial function depending on the frequency of the incident light as well as symmetry of the medium.

2.1.2 Light Matter Interaction with Metals

2.1.2.1 Dielectric Function of Metals

A large part of this thesis is based on the interaction of electromagnetic radiation with metals, in which case the dielectric function is dominated by the contribution of the loosely bound "free" electrons. For metals the conduction band is partially filled up to the Fermi level. Therefore, the electrons in the conduction band and the electrons of lower energy bands transitioning to the conduction band (interband transitions) contribute to the optical response in the visible region. A common model that describes the dielectric function of metals analytically is the *Drude model*, which spans the entire visible range. The Drude model describes metals as a combination of a constant background which consists of the positively charged ion cores making up a rigid lattice and a high density (10^{23} cm^{-3}) electron gas of mobile electrons in the conduction band. If exposed to an external electrical field the electrons with charge q_0 undergo harmonic oscillations. The displacement from their equilibrium position $\vec{r}$ can be simplified to a driven harmonic oscillator with the electrical field $\vec{E}(\omega)$ as driving force[3]:

$$m_e \frac{d^2\vec{r}}{dt^2} + m_e \overbrace{\left(\frac{v_F}{l}\right)}^{\gamma} \frac{d\vec{r}}{dt} = -q_0 \vec{E}_0 e^{-i\omega t} \tag{2.16}$$

with m_e being the electron mass. The Fermi velocity v_F and the mean free path l contribute to the damping term γ. In an isotropic medium the displacement r of an electron with respect to its equilibrium lattice position leads to a micrsocopic dipole moment $\vec{p} = q_0 r$. Solving equation (2.16) with the ansatz $r = r_0 e^{-i\omega t}$ the dipole moment can be calculated. On the macroscopic scale this leads to a net polarisation P of N displaced electrons per volume V:

$$P = -\frac{N q_0 r}{V} = \frac{n q_0^2}{m_e} \frac{1}{\omega^2 + i\gamma\omega} E \tag{2.17}$$

where n is the electron density N/V. From the macroscopic polarisation P the dielectric function of metals $\varepsilon(\omega)$ results :

$$\varepsilon(\omega) = 1 + \frac{P}{\varepsilon_0 E} = 1 - \frac{n q_0^2}{\varepsilon_0 m_e} \frac{1}{\omega^2 + i\gamma\omega} = 1 - \frac{\omega_p^2}{\omega^2 - i\gamma\omega} \tag{2.18}$$

Here the bulk plasma frequency $\omega_p = \frac{n q_0^2}{\varepsilon_0 m_e}$ is a material parameter and describes the eigenfrequency of the oscillating electron cloud in the metal. The dielectric function derived through the Drude model describes metals as free electron gases. It does not

take into account interband transition of electrons in lower energy bands (gold $\leq$ 500 nm, silver $\leq$ 300 nm) and is therefore limited to longer wavelength (λ>500 nm). For shorter wavelengths the energy is high enough to excite electrons from the valence band into the conduction band, which leads to an increase in the absorption and therefore in the imaginary part of the dielectric function. To get a more accurate description for metals at shorter wavelengths the interband transitions need to be accounted for as well as the additional offset ε_∞. This stems from the highly polarisable environment in noble metals and ranges from $1 \leq \varepsilon_\infty \leq 10$ depending on the metal. The interband transition can be similarly accounted for as the conduction band electrons in the Drude model. An additional restoring force $m^*\omega_0 x$ is added to the equation stemming from the more bound electrons in the valence band. The full Drude-Lorentz model is shown in Figure 2.1:

$$\varepsilon(\omega) = \varepsilon_\infty - \frac{\omega_p^2}{\omega^2 + i\gamma\omega} + \sum_i A_i \omega_i \left(\frac{e^{i\phi_i}}{\omega_i - \omega - i\gamma_i} + \frac{e^{-i\phi_i}}{\omega_i + \omega - i\gamma_i} \right) \tag{2.19}$$

with A_i, ω_i, γ_i and ϕ_i being the transition strength, energy, damping and phase relation. It should be noted here that the real part of the dielectric function $\mathrm{Re}\left[(\varepsilon(\omega))\right]$ is negative

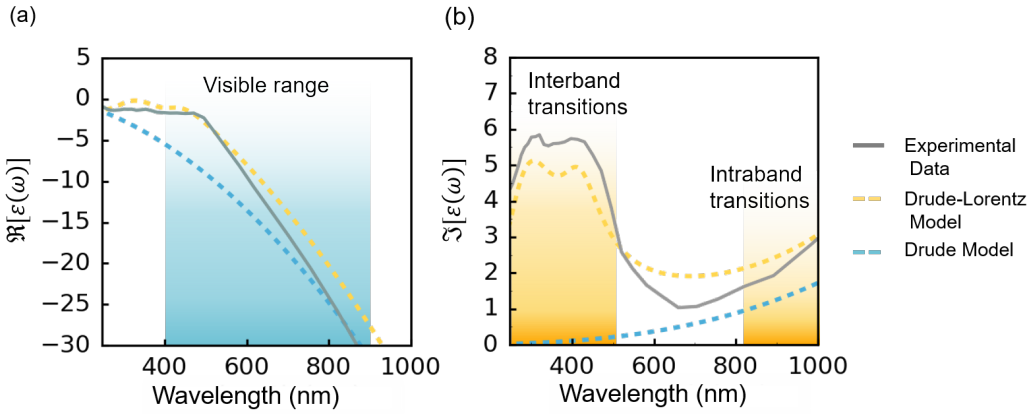

Figure 2.1: **Dielectric function of gold** Comparison of the Drude-model (blue dashed lines), Drude-Lorentz model (orange dashed lines) and measured dielectric function (Johnson and Christy[4], solid grey line). (a) Real and (b) imaginary part of the dielectric function $\varepsilon(\omega)$ of gold.

in the visible due to the 180 degree phase delay between the incident electromagnetic field and the electron oscillation. This causes the typical reflective character of metals and prevents the penetration of light. This very small skin depth of light entering the metal leads to interesting phenomena at a metal interface, which will be discussed in the following section.

2.1.2.2 Introduction to Plasmonics

So far bulk plasma oscillations were considered, which propagate through the metal. In the presence of a planar boundary, new modes arise, so called surface plasmon polariton modes (SPPs). These surface charge oscillations travel across the interface and rapidly decay perpendicular to the interface. As a consequence they lead to large field enhancements with very small mode volumes, confining light below the diffraction limit. These surface effects can be even further enhanced by reducing the dimension of the metal structure. Localised Surface plasmons (LSP) arise at nanoparticle surfaces where the modes are spatially confined to the surface of the nanostructure and do not propagate. Many of these compelling features are highly desired for nanoscale sensing as well as self-assembly techniques and will be explained in detail in the following sections.

2.1.2.3 Surface Plasmon Polaritons

Surface plasmons are surface charge oscillations that are located at a metal-dielectric interface. These modes travel along the interface, where the electric field decays exponentially away from the interface (Figure 2.2 a):

$$\vec{E} = \vec{E}(z)e^{(ik_x x - \omega t)} \tag{2.20}$$

As a solution of the Maxwell equation these modes require continuity of the dielectric displacement ($\varepsilon\vec{E}$) normal to the interface and the magnetic field component tangential to the interface in the absence of surface charges. Therefore under the assumption of temporal harmonic fields, $\vec{E} = \vec{E}_0 e^{(i\omega t)}$, the following relations for the two perpendicular polarisations can be written[2]:
Transverse electric polarization (with $[H_{d,x} = H_{m,x}$ and $E_{d,y} = E_{m,y}]_{z=0}$):

$$\begin{aligned} \frac{\mu_0}{\omega} k_{d,z} E_{d,y} &= -\frac{\mu_0}{\omega} k_{m,z} E_{m,y} \\ \rightarrow E_y(k_{d,z} + k_{m,z}) &= 0. \end{aligned} \tag{2.21}$$

Transverse magnetic polarization (with $[E_{d,x} = E_{m,x}$, $D_{d,z} = D_{m,z}$ and $H_{d,y} = H_{m,y}]_{z=0}$):

$$\begin{aligned} ik_{d,x} H_{d,y} = ik_{m,x} H_{m,y} \quad \text{and} \quad i\frac{k_{d,z}}{\varepsilon_d} H_{d,y} &= i\frac{k_{m,z}}{\varepsilon_m} H_{m,y} \\ \rightarrow k_{d,x} = k_{m,x} \quad \text{and} \quad \frac{k_{d,z}}{k_{m,z}} + \frac{\varepsilon_d}{\varepsilon_m} &= 0. \end{aligned} \tag{2.22}$$

where ε_d, ε_m and k_d, k_m are the dielectric functions and k-vectors of the metal and dielectric material respectively (see Figure 2.2a). From the first relation (2.21) it is evident, that for positive k this equation only has one solution: $E_y = 0$. Therefore s-polarized surface plasmon polaritons do not exist.
Furthermore, inserting the magnetic fields into the Helmholz equation (2.7) and considering the continuity of the H_y from the second relation (2.22) the following relations are deduced:

$$k_{z,m}^2 = k_x^2 - k_0^2 \varepsilon_m \tag{2.23}$$

$$k_{z,d}^2 = k_x^2 - k_0^2 \varepsilon_d \tag{2.24}$$

A combination of all these conditions gives the dispersion relation of SPPs with in-plane wave vector $k_{SPP} = k_x$ [2]:

$$k_{SPP} = k_0 \sqrt{\frac{\varepsilon_d \varepsilon_m}{\varepsilon_d + \varepsilon_m}} \tag{2.25}$$

and the normal wavevector component of the SPPs:

$$k_{j,z} = k_0 \frac{|\varepsilon_j|}{\sqrt{\varepsilon_d + \varepsilon_m}} \qquad j = \{d, m\}\,. \tag{2.26}$$

Here k_0 is the free space wavevector in the surrounding medium (air). Under the consideration that ε_m is negative in the visible region it becomes evident that $k_{SPP} > k_0$. Therefore SPP modes can not be excited from free space propagating electromagnetic waves due to the momentum mismatch. In order to couple to SPPs the incident wavevector needs to be shifted to larger wavevectors. This can be achieved by using surrounding dielectric media with higher refractive indices such as prisms (Kretchmann-[5] and Otto-configurations or gratings ([2]) to match the k-vectors. A limiting factor of surface plasmons are their losses. Real metals are very lossy (from electron and phonon scattering) and damping is known to limit the propagation length of SPPs along the interface: $L_{SPP} = 1/(\mathrm{Im}\,[k_{SPP}])$, where $L_{SPP}(Au) \sim 10\mu$m and $L_{SPP}(Ag) \sim 60\mu$m at $\lambda = 633$nm [3].

2.1.2.4 Localized Surface Plasmons

So far, it was discussed that, plasmonic modes at planar metal dielectric interfaces which propagate and cannot be excited by free space waves. In the following these modes will be extended to localized surface plasmons (LSPs, Figure 2.2 b). Similar to SPPs these modes are surface plasmon excitations confined at the interface of metallic nanostructures, such as nanowires and nanoparticles. The nanostructures have sub-

wavelength dimensions and the confinement of light to their surface therefore allows localization of light below the diffraction limit. When excited, the overall displacement of the electron gas compared to the positively charged ion cores gives rise to restoring forces with specific resonances. The properties of LSPs are dominated by the shape and size of the nanostructures and their curvature allows for free space excitation. As depicted in Figure 2.2c different shapes lead to different resonances where high curvatures and edges lead to charge accumulation accompanied with large field enhancements. One of the

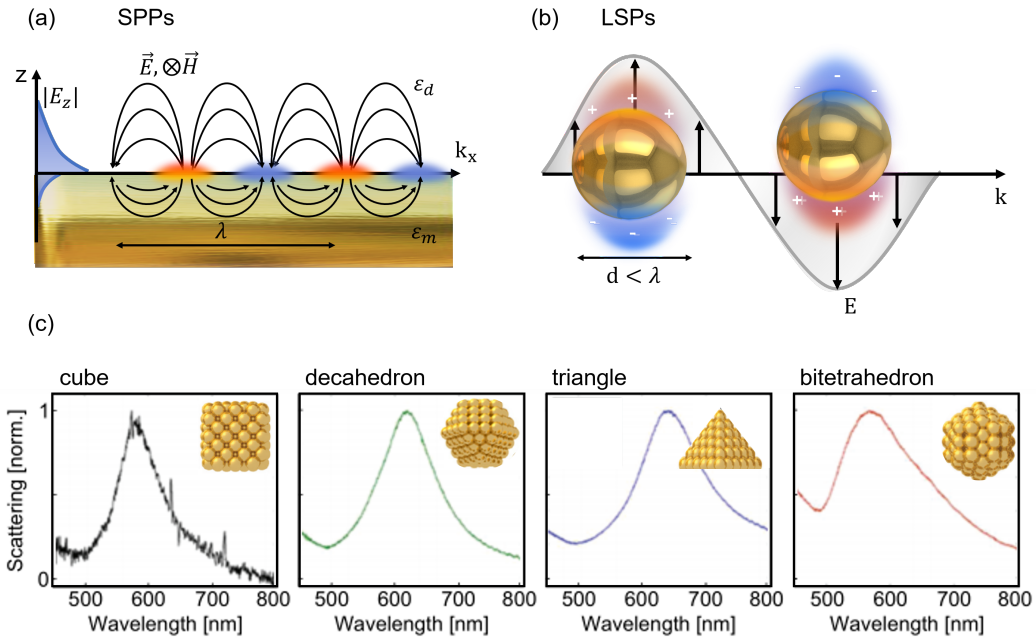

Figure 2.2: **Surface Plasmons and Localized Surface Plasmons** (a) Surface plasmon (SPPs) propagating along a metal-dielectric interface with the electric field $\vec{E}$ oscillating normal and the magnetic field $\vec{H}$ parallel to the interface. Normal to the interface the electric field decays exponentially. (b) Non-propagating Localized Surface Plasmons (LSPs) bound to a nanoparticle surface much smaller than the incident wavelength $d < \lambda$. (c) Different shapes of Au nanostructures lead to different resonances accompanied with large field enhancements (Figure adapted from [6])

simplest nanostructures is the single spherical nanoparticle. For the spherical nanoparticle the resonance condition with the external electrical field can be described within the quasi-static approximation. The quasi-static approximation neglects retardation effects (propagation of light across the nanostructure) and therefore assumes that all points of the nanoparticle respond simultaneously to the external field. This approach is valid for particles much smaller than the incident wavelength $d \leq 100$ nm (Figure 2.2b). In the quasi-static limit the Helmholz equation reduces to the Laplace equation ($\nabla^2 \phi = 0$), which can be written in spherical coordinates:

$$\left[\frac{1}{r^2}\frac{\partial}{\partial r}\left(r^2\frac{\partial}{\partial r}\right) + \frac{1}{r^2 \sin\vartheta}\frac{\partial}{\partial \vartheta}\left(\sin\vartheta\frac{\partial}{\partial \vartheta}\right) + \frac{1}{r^2 \sin^2\vartheta}\frac{\partial^2}{\partial \varphi^2}\right]\phi(r,\vartheta,\varphi) = 0. \quad (2.27)$$

A general solution to the equation for spherical symmetry is of the form[3]:

$$\Phi_{l,m_i}(r,\vartheta,\varphi) = \sum_{l=0}^{l=\infty} \sum_{m_l=-l}^{l} \left[A_l r^l + B_l r^{(l+1)}\right] P_l^m\left[cos(\vartheta)\right] e^{im_l\varphi} \tag{2.28}$$

where l is the degree of spherical harmonic, m_l its order, A_l, B_l constants that are determined by the boundary conditions and $P_l\left[cos(\vartheta)\right]$ the Legendre polynomials.
Applying the boundary conditions of Maxwell equations (continuity of $E_{\parallel}$ and $D_{\perp}$) this leads to two solutions for a small spherical particle of radius a:

$$\Phi = \begin{cases} -\dfrac{3\varepsilon_d}{\varepsilon(\omega)+2\varepsilon_d} r cos(\vartheta) & r \leq a \\ -E_0\, r\, cos(\vartheta) + E_0 \dfrac{\varepsilon(\omega)-\varepsilon_d}{\varepsilon(\omega)+2\varepsilon_d} a^3 \dfrac{cos(\vartheta)}{r^2} & r \geq a \end{cases} \tag{2.29}$$

Important to note here is the independence from the azimuthal angle φ due to the spherical symmetry. With the solutions of the Laplace equation the dipole moment $\vec{p} = \varepsilon\varepsilon_0\alpha\vec{E}$ of the displaced electron gas can be calculated:

$$\vec{p} = 4\pi\varepsilon_0 a^3 \frac{\varepsilon(\omega)-\varepsilon_d}{\varepsilon(\omega)+2\varepsilon_d} \tag{2.30}$$

where α denotes the polarizability. The resonance condition (Fröhlich condition) is met for $\mathrm{Re}\left[\varepsilon(\omega)\right] = -2\varepsilon_d$.

2.1.2.5 Optical Response of Single Nanoparticles

The electric near-field at the surface of the particle and therefore the near-field enhancement is given by[7]:

$$E_{NF} = \frac{3\varepsilon_d}{\varepsilon(\omega)+2\varepsilon_d} E_0 \tag{2.31}$$

With E_0 being the amplitude of the driving field. For example on gold nanoparticles the accumulation of charge at the surface leads to enhancement factors of ~ 55 (for a 40 nm gold sphere[8]). This field enhancement is highly localized and drops off quickly further away from the nanoparticle as $1/r^3$.[8]
In the far field the nanoparticle can be approximated as a point source dipole that absorbs and scatters light. For an emitting dipole the radiated field can be written[3]:

$$\vec{E} = \frac{1}{4\pi\varepsilon_0\varepsilon(\omega)} \left[k^2(\vec{n}\times\vec{p})\times\vec{n}\frac{e^{ikr}}{r} + \left[3\vec{n}(\vec{n}\cdot\vec{p}) - \vec{p}\right]\left(\frac{1}{r^3} - \frac{ik}{r^2}\right)e^{ikr}\right] \tag{2.32}$$

with $\vec{n}$ being the unit vector in the direction to the dipole. From equation (2.36) it is evident that the radiated field is dominated by the last term $(1/r^3)$ for close distances, the so called near-field $r \ll \lambda$, and the first term $(1/r^1)$ for the far-field $r \gg \lambda$. In order to describe the full response of a metal nanoparticle with incident electromagnetic waves it is useful to define the scattering cross section and absorption cross section:

$$\sigma_{scat} = \frac{k^4}{6\pi} |\alpha|^2 = \frac{8\pi}{3} k^4 a^6 \left| \frac{\varepsilon(\omega) - \varepsilon_d}{\varepsilon(\omega) + 2\varepsilon_d} \right|^2 \tag{2.33}$$

$$\sigma_{abs} = k \mathrm{Im}\,[\alpha] = 4\pi k a^3 \mathrm{Im} \left[\frac{\varepsilon(\omega) - \varepsilon_d}{\varepsilon(\omega) + 2\varepsilon_d} \right] \tag{2.34}$$

The sum of the two is called extinction and represents the total effect of a medium on radiation. As the scattering cross-section scales with $\sigma_{scat} \propto a^6$, it dominates over absorption for larger particles. However for very small particles the absorption $\sigma_{abs} \propto a^3$ becomes more important.
The scattering response of single nanoparticles spans a broad spectral range and highly depends on the size, shape, surrounding refractive index and nanoparticle material[9]. This sensitivity to its surrounding medium has been widely exploited in sensing applications[10–12]. Nonetheless, the synthesis of precise nanostructures with a tailored optical response remains challenging. Another approach to tune the optical response of nanostructures involves coupled nanoparticles. If nanoparticles are placed close enough, coupling between them can occur. In this case the optical response is given by combining the single nanoparticle response with a coupling term that is highly dependent on the distance. The use of sub-nanometer spacer materials offers great control over the optical response and near field enhancements.

So far plasmonics were discussed in the quasi static regime. However, it has to be noted that this approach has its limitations as soon as the particle is comparable in size to the incident wavelength. Retardation effects result in phase differences between the incident field and the induced electron oscillations across the particle, strongly influencing the radiated fields. In order to derive an accurate picture Mie theory is required for a more general description. This is discussed elsewhere[3,13] as it would go beyond the scope of this thesis. Nanoparticle sizes explored within this work do not exceed 100 nm.

2.1.2.6 Hybridization- Plasmonic Coupling

Placing two nanoparticles in close proximity to each other with a distance $\mathrm{d_{crit}} \leq 1/\mathrm{k_{spp}}$ introduces plasmonic coupling between the two nanoparticles, leading to additional resonances in the optical response. The coupling can be described within a hybridization picture similar to the formation of molecular orbitals[14] (Figure 2.3).

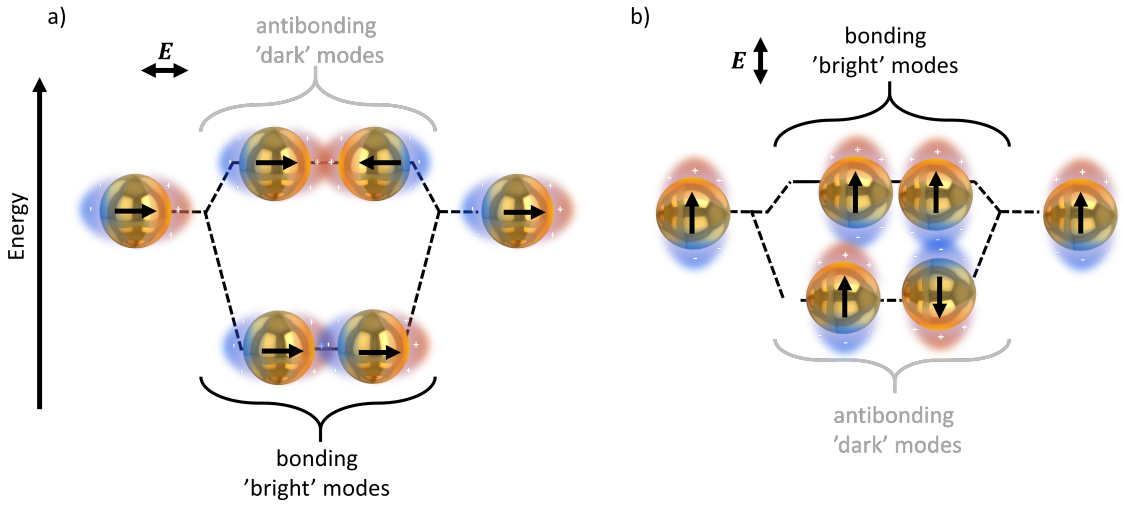

Figure 2.3: (a) Hybridization Model for a nanoparticle dimer. The incident electrical field along a) and perpendicular b) to the dimer connecting axis leads to coupling behaviour of the nanoparticles. The individual induced dipoles are indicated with black arrows. Similar to the molecular orbital theory this leads to "bonding" and "antibonding" modes according to the symmetry. While the bonding modes have a net dipole and therefore are optically "bright" the anitbonding modes remain dark. The image is adapted from [14,15].

In the simplest case of two spherical gold nanoparticles, separated by distance d, the resonantly excited dipole of the individual particle can couple to the dipole of the neighbouring particle. Similar to molecular orbital theory, two states of different energies exist: the bonding state (in phase), which is energetically favourable and the anti-bonding state (out of phase), which has a higher energy compared to the single particle mode (Figure 2.3).The energy difference between the two states is due to the Coulomb-interaction between the single nanoparticle dipoles. In contrast to the uncoupled plasmon modes, the coupled modes show a strong dependence on the inter particle distance, which is observed as shifts in the plasmon resonance [16]. The shift can be approximated using a phenomenological "plasmon ruler" equation [17,18]:

$$\frac{\Delta\lambda}{\lambda} \sim \exp\left(-\frac{(d/D)}{\tau}\right) \tag{2.35}$$

for nanoparticles of diameter D and an inter-particle distance d. The bonding state has a lower energy (red-shifted) and an effective net dipole moment, that allows coupling to light. The anti-bonding mode is blue shifted. It is optically dark since the dipoles of the individual nanoparticles are anti-parallel so that the net dipole cancels out to zero.
From the point source dipole approximation (2.36), it is evident that the interaction energy U of the fundamental mode $l = 1$, scales with d^{-3}:

$$U \propto \frac{p_1 p_2}{d^3} \tag{2.36}$$

Higher order modes ($l=2, l=3, ...$) have an even shorter interaction range ($\propto d^{-5}, d^{-7}, ...$). For very small gaps $d \leq 1$ nm, these have to be take into account, which introduces asymmetry in the hybridization picture. Going even further to $d<0.1$ nm the classical description reaches its limit and doesn't fully hold any more. In this regime local effects become important and a quantum mechanical description is necessary to describe the full picture[19,20].

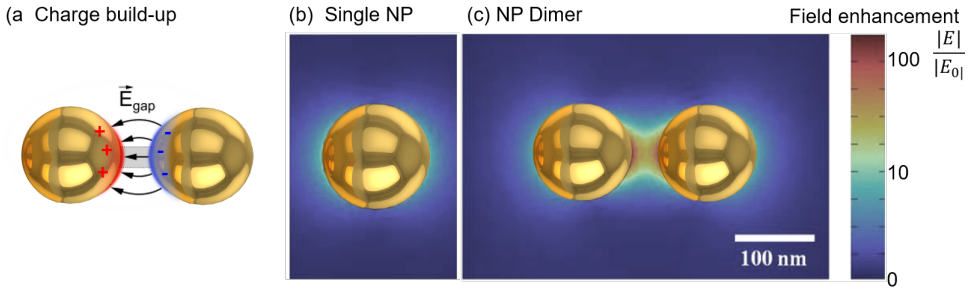

Figure 2.4: **Field Enhancement of coupled nanoparticles**(a) Schematic of charge building up in the "hot-spot". Boundary element simulations (BEM) of field enhancement for a single nanoparticle (b) in comparison to a nanoparticle dimer (c) with high field confinement in the gap region.

Another side effect of coupling between nanoparticles is the increasing localization of the field enhancement with decreasing nanoparticle distance. As they are brought closer together initially the far-field response decreases as the effective dipole is reduced due to the coupling. However, the dimer acts like a capacitor with charge building up at the opposing faces of the nanoparticle when further decreasing the gap size. In the case of a perfectly insulating gap material, with no charge transfer, this charge build up leads to a strong near-field enhancement in the gap between the nanoparticles, the so called "hot-spot". The simulated local field enhancement of a 80 nm Au dimer and a single nanoparticle is shown in Figure 2.4. The large enhancement on very small scales make the coupled system a promising platform for sensing allowing nanometer resolution and single molecule sensitivity[21].

In a different context the plasmonic hot spot can also be regarded as a plasmonic cavity that confines light below the diffraction limit. Optical cavities can either be used to boost or suppress light-matter interactions by confining light in space, usually through multiple reflections. They are therefore essential in many different fields, such as nano-sensing, optical fibers, semiconductor lasers, quantum entanglement, and other quantum optical devices[22]. Their characteristic parameters and how plasmonic cavities fit into this picture will be the content of the next section.

2.1.3 Transition from Weak to Strong Coupling Regime

Introducing different regimes of light-matter interaction, the following section gives an overview of dielectric and plasmonic cavities to enhance light-matter interactions. The two extreme cases of weak and strong light-matter interaction are discussed within the two level picture and a simple classical analogy of a coupled harmonic oscillator is used to describe the transition between the two regimes.
The possibility to tune the energy states of an emitter, such as an atom or a single molecule, by means of light is of great interest in many areas such as chemistry, nano-sensing, nonlinear optics on the nanoscale and many others[23–25]. Nonetheless, the inherent mismatch in the size of the absorption cross-section of atoms or molecules and the wavelength of visible light decreases the probability of light-matter interaction drastically. Furthermore, the coupling strength ($g \propto \mu E(r,\omega)$) is proportional to their dipole strength, making some emitters more suitable than others. For these reasons, optical cavities are used to boost the interaction between single emitters and surrounding optical fields. The probability of an emitter to emit a photon is highly dependent on the local photonic environment and the number of final states available to the transition[26]. The density of the local optical states available (LDOS) depends on the refractive index as well as the wavelength of emission.
Creating a specific resonant environment for certain wavelengths, a cavity can be used to change the LDOS in order to achieve better coupling between the local surrounding electromagnetic field and the emitter.

2.1.3.1 Optical Cavities

The performance of cavities can be characterized by two parameters, the quality factor Q and the mode volume V_m. For an ideal cavity, light would be confined indefinitely with no leakage. In real cavities $Q = \omega_c/\kappa$ is a measure of the time that light is confined in the cavity before it leaks out and V_m is a measure of the spatial confinement of the cavity mode. It defines the volume in which the energy density $W(r,\omega)$ of the optical cavity mode is confined[27]:

$$V_m(\omega) = \frac{\int W(r,\omega) d^3r}{\max\left[W(r,\omega)\right.} \tag{2.37}$$

$$= \frac{\int \varepsilon(r,\omega)\left[E(r)\right]^2 d^3r}{\max\left[\varepsilon(r,\omega)E(r)^2\right]}. \tag{2.38}$$

Here it has to be noted that strictly speaking this is only valid for dielectric cavities where losses can be neglected. An accurate calculation becomes more complicated for metals where the imaginary part has to be accounted for[28].
Both Q and V_m may vary extensively with different geometries and cavity materials. The most significant examples of optical cavities are shown in Figure 2.5 according to their quality factor and mode volume. The first experimental example reaching the strong coupling regime was obtained for a single Rydberg atom in a superconducting microwave cavity. However in the decades after, many examples followed using a variety of cavities reaching quality factors up as high as 10^{10}[29] (dielectric micro-cavities Figure 2.5 (a), top right), and mode volumes as small as 40 nm^3[21]. While planar dielectric micro-cavities are well established with very large Q their mode volumes are rather large ranging from hundreds of μm^3 to tenth of mm^3. Photonic-crystal-slabs ($\sim$ 10 μm^3) and micro-discs ($\sim$ 1 μm^3) are the first examples of reducing the mode volume (Figure 2.5 (a) top right). However, for optical cavities the mode volume is inherently limited to the diffraction limit of the wavelength ($V_m \geq \lambda_0/n$) in a medium with refractive index n. This also limits the maximum achievable coupling strength for single emitters since the mode volume can not easily be pushed below the diffraction limit. State of the art dielectric cavities with Q-factors of $\sim 10^{10}$ reach the strong coupling regime even for large mode volumes due to their minimal losses. Nonetheless, this is also a restricting factor. The very narrow linewidth that is associated with the high Q-factor cavities limits the operating bandwidth and requires the emitter to have equally narrow linewidth to allow optimal coupling and a perfect overlap between the two resonances. Most of these cavities therefore operate at low temperatures with cryogenic conditions. Other challenges that dielectric cavities face are their cost and resource intensive fabrication as well as their lack of adaptability. To achieve precise cavities with large Q factors complicated fabrications steps are involved that render large scale fabrication for applications difficult. Thus, it is desirable to develop truly nanophotonic approaches such as plasmonic cavities to confine light below the diffraction limit, providing an easily fabricated, lower cost alternative. The ultra-confined, sub-diffraction-limited mode volumes of plasmonic systems offer huge coupling strengths g (in the 1-100 meV range) to single quantum emitters enabling strong coupling even at room temperature and ambient conditions.

What started off with simple interfaces between metal and dielectrics to couple Surface Plasmon Polaritons (SPPs) to quantum emitters[26,28,31], (Figure 2.5 (a) middle) rapidly extended to a whole range of plasmonic cavity designs (Figure 2.5 (a) yellow cavities). Different geometries of the nanostructures highly affect the plasmonic modes and their field enhancement, ranging from surface plasmon polaritons (SPPs, Figure 2.5 (a) middle) to localized surface plasmons (LSPs, Figure 2.5 (a) bottom left). Here, the mode volume and field enhancement scales with the size of the nanostructure ($V_m \sim R^3$).

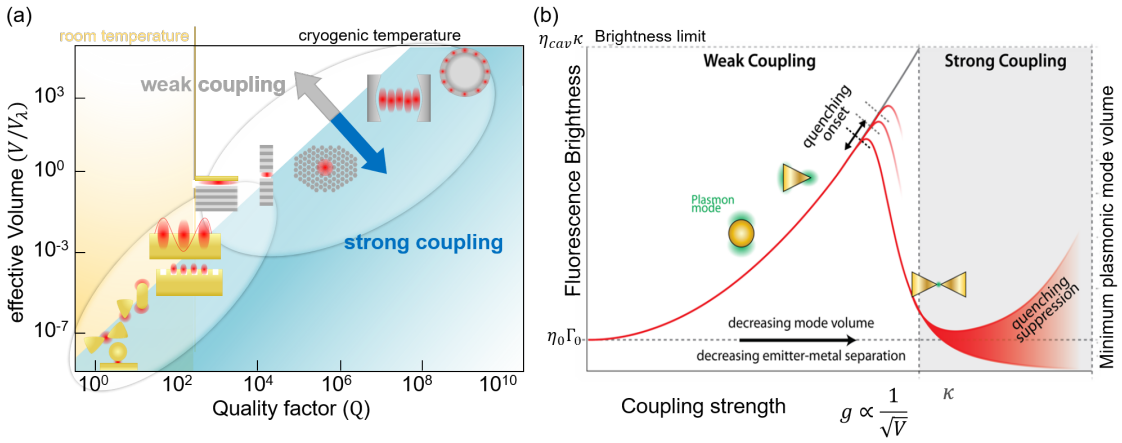

Figure 2.5: **Figure of merit of optical cavities** (a) Optical cavities ranked according to their effective mode volume $V_m{=}V/V_\lambda$ and quality factor Q showing the strong coupling regime in the blue area. Room temperature conditions are marked with the orange area. Schematic of optical cavities, left to right: Nanoparticle on mirror cavity (NPoM), Bow-tie dimers, single nanoparticle and nanorod, plasmonic lattices, flat metal surface, tamm-plasmon cavity, micro-pillars, photonics crystals, micro-cavities, whispering gallery modes. (b) Theoretical maximum brightness enhancement of an emitter coupled to a plasmonic cavity as a function of coupling strength. With η_0 being the emitter quantum efficiency, η_{cav} the radiation efficiency of the cavity, Γ_0 the spontaneous emission rate of the uncoupled molecule, and κ the total cavity decay rate. For large coupling strength and low mode volumes the distance between the quantum emitter and the plasmonic metal decreases below the quenching regime where the photon output is reduced. This quenching onset depends on the exact geometry of the plasmonic system. In the strong coupling regime quenching can become suppressed [30]. Figure is adapted from [21,28].

However, the smallest mode volume was achieved by coupled plasmonic nanostructures (Figure 2.5 bottom left corner). The cavity field is confined to the hotspot created between the adjacent nanoparticles (for more details see section 2.1.2.6) and therefore scales with the gap distance between them. Using molecular linkers, mode volumes as small as 40 nm^3 in the vertical direction have been demonstrated [21], accompanied by a near-field enhancement of the order 10^4 .

However, despite the small mode volumes and therefore coupling strength that outshine dielectric micro-cavities by far, plasmonic cavities are still limited by their large losses and therefore low Q-factor. While the low Q increases their operating bandwidth it affects the total radiative quantum efficiency of the system drastically:

$$\eta = \frac{\Gamma_r}{\Gamma_r + \Gamma_{nr}} \tag{2.39}$$

where Γ_r is the radiative decay rate and Γ_{nr} the non-radiative decay rate. The different loss mechanisms are highly dependent on the exact geometry of the plasmonic system as well as the distance of any emitter placed in proximity of the metal surface (Figure 2.5 b). In an ideal coupled system, the emission of a coupled emitter which is pumped in saturation would increase quadratically from its free space emission efficiency ($\eta_0\Gamma_0$)

only limited by the cavity losses[26]. However, when an emitter is placed close to the metal surface of an isolated NP (~ 10 nm) strong quenching effects occur[32] due to coupling to higher order modes leading to absorption in the metal[30]. Therefore, in most systems the total emission of a coupled emitter is a balance between reduced mode volume and proximity to the metal surface. However, this is highly dependent on the geometry and can be prevented in certain plasmonic coupled structures like the nanoparticle on mirror cavity. It has been shown that in the NPoM system the emission of emitters as close as 1 nm to the metal[21,30] can be enhanced. In this geometry the speed-up of the emission rate prevents the coupling to higher order modes and non-radiative channels leading to quantum efficiencies as high as $\eta \geq 0.5$ for nanoparticle sizes of 60-80 nm[30].

2.1.3.2 Weak Coupling Regime

Typically in the weak coupling regime the energy of the coupled system is lost before a coherent exchange between the emitter and the cavity can be established ($\kappa > g > \gamma_e$, where κ are the losses due to the cavity and γ_e the losses due to the emitter scattering). This leads to a modification of the spontaneous decay rate of the emitter giving rise to phenomena such as the Purcell effect[33] and Föster energy transfer between an acceptor and a donor[26], but leaves the energy states unchanged[31,34,35] (Figure 2.6 a).

The transition of the weak to the strong coupling regime is given by the coupling

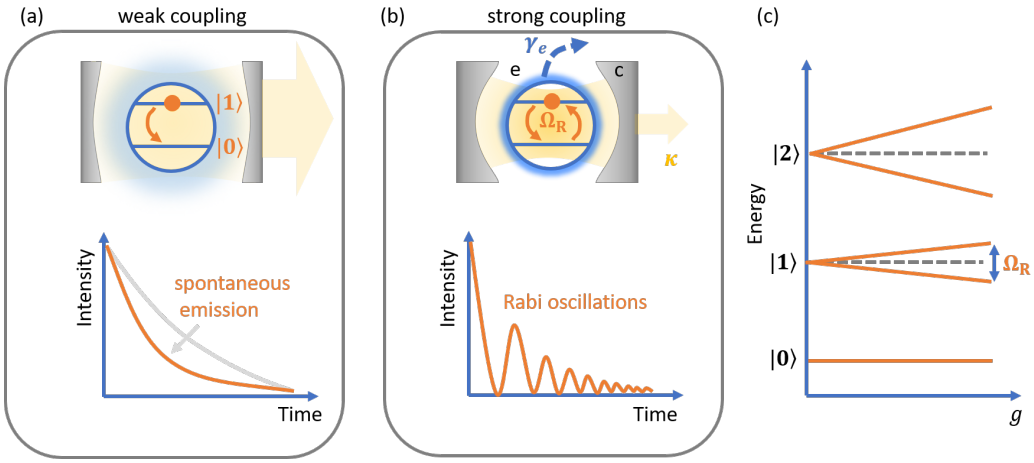

Figure 2.6: **Transition from the weak coupling to the strong coupling regime between an optical cavity and a two level emitter** (a) Weak coupling regime: Modification of the spontaneous decay rate shown at the bottom. (b) Strong coupling regime: coherent Rabi oscillations with rate Ω_R^{-1} between the two states. (c) Energy splitting (Ω_R) as a function of coupling strength g described by the Jaynes-Cummings energy ladder of a strongly coupled emitter-cavity system.The ground state remains unaffected by the coupling. Figure is adapted from[28]

strength g which is quantified by the ratio of Q/V_m[36]. As stated earlier the quality

factor $Q = 1/\kappa$ is the inverse of the cavity loss κ and V_m is the effective mode volume. Here, the mode volume is the parameter that encodes the local density of states (LDOS). For small coupling and low ratios of Q/V_m the emitter energy dissipation into the cavity mode and other losses are non-reversible. Modification of the spontaneous decay rate can be deduced from Fermi's golden rule that expresses the emission rate Γ as a function of the density of electromagnetic modes[37]:

$$\Gamma = \frac{2\pi}{\hbar^2} |M_{12}|^2 \rho(\omega) \tag{2.40}$$

with M_{12} being the transfer matrix element and ρ the density of states. In the case of an emitter in free space the matrix transfer element can be expressed as $M_{12} = \langle |\mu_{12} E| \rangle = 1/3 \mu_{12}^2 E_{vac}^2 = (\mu_{12} \hbar \omega)/(6 \varepsilon_0 V)$ and the free space density of states $\rho_f(\omega) = \frac{\omega^2 V}{\pi^2 c^3}$. This leads to the spontaneous emission rate in free space:

$$\Gamma_f = \frac{\omega_0^3 \mu_{12}^2}{3\pi \varepsilon_0 \hbar c^3} \tag{2.41}$$

When the emitter is than placed into a cavity the density of states is altered with certain wavelengths ω_c resonantly enhanced:

$$\rho_c(\omega) = \frac{\kappa}{2\pi V_m} \frac{1}{(\kappa/2)^2 + (\omega_c - \omega)^2} \tag{2.42}$$

The modified emission rate of an emitter in a cavity can therefore be written as:

$$\Gamma_c = \frac{3Q\lambda^3}{4\pi^2 V_m} \frac{\kappa^2}{4(\omega - \omega_c)^2 + \kappa^2} \frac{|\mu_{12} E|^2}{|\mu_{12}|^2} \Gamma_f \tag{2.43}$$

In the case of resonance $\omega = \omega_c$ this simplifies to:

$$\Gamma_c = \frac{3\lambda^3}{4\pi^2} \left(\frac{Q}{V_m} \right) \Gamma_f \tag{2.44}$$

However to describe the coupling of the emitter to a cavity in the weak coupling regime the Purcell factor is usually preferred.The Purcell factor describes the enhanced emitter decay rate when placed in a cavity compared to its free space spontaneous decay rate Γ_0:

$$F_P = \frac{\Gamma_c}{\Gamma_f} = \frac{3}{4\pi^2} \left(\frac{\lambda_0}{n} \right)^3 \frac{Q}{V_m} \tag{2.45}$$

Here λ_0 is the transition wavelength of the emitter and n is the refractive index within the unit volume.

This emission enhancement is exploited in a variety of applications, such as bio-imaging [32], photochemistry, single-photon sources and quantum information [23,25,33,38,39],where emitters with very low emission yields are involved. However, more profound effects emerge when the emitter "'strongly couples"' to the optical fields for high ratios of Q/V_m . Placing an emitter in a resonant optical cavity establishes a mutual exchange of the energy of the emitter and the surroundings that allows for the energy to cycle back and forth coherently.

2.1.3.3 Strong-Coupling Regime

In order to reach the strong coupling regime the coupling constant g needs to exceed the losses due to the emitter scattering γ and the cavity κ. For strong enough interaction, both the emission rate and the energy levels of the emitter can be altered. The coupling leads to strong entanglement of the emitter and the optical field forming two new hybrid states that are neither solely light nor matter. This splitting of the states is called Rabi-splitting with the Rabi frequency $\Omega_R = 2g$. Tuning the coupling strength the energy levels of the coupled system are shifted. The mechanism can be fully described using the quantum mechanical Jaynes-Cummings model [28,31] with a Hamiltonian for a two level system:

$$H = \hbar\omega a^\dagger a + \frac{1}{2}\hbar\omega_0\sigma_z + hg(a\sigma_+ + a^\dagger\sigma_-), \tag{2.46}$$

where ω is the frequency of the cavity field and ω_0 the frequency of the transition of the 2 level emitter $\omega_0 = (E_e - E_i)/\hbar$. Here $a^\dagger, a$ are the field creation and annihilation operators and $g = \mu\frac{\hbar\omega}{2\varepsilon_0 V_m}$ the coupling strength. A simplified picture that captures many of the key features of strong coupling is the classical two harmonic oscillator model [31]. The coupling dynamics are described by two oscillators (Figure 2.7) with resonances ω_c and ω_e. The displacement of the two oscillators evolves according to the following coupled equations of motions:

$$\frac{d^2x_c}{dt^2} + \gamma_c\frac{dx_c}{dt} + \omega_c^2 x_c + g^2(x_c - x_e) = 0 \tag{2.47}$$

$$\frac{d^2x_e}{dt^2} + \gamma_e\frac{dx_e}{dt} + \omega_e^2 x_e + g^2(x_e - x_c) = 0 \tag{2.48}$$

with γ being the damping of the oscillators and g the coupling strength of the two oscillators e (emitter) and c (cavity). The differential equations can be solved assuming

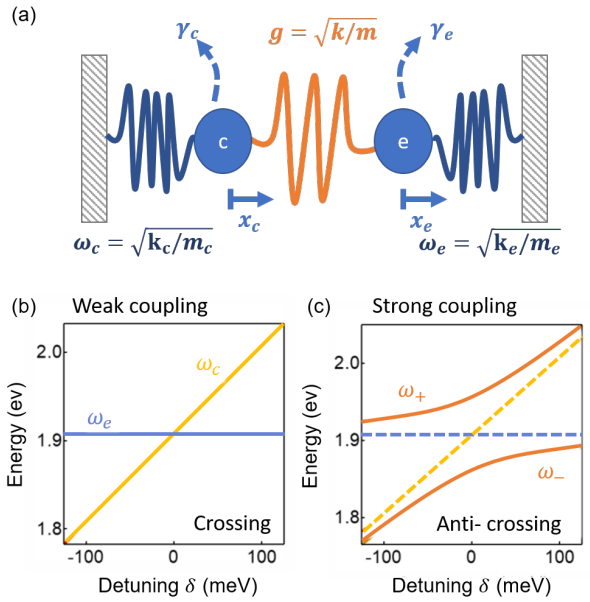

Figure 2.7: **Harmonic Oscillator model for strongly coupled systems** (a) Schematic of a harmonic oscillator with eigenfrequencies ω, dissipation γ and the coupling strength g of the two oscillators e (emitter) and c (cavity. (b) Crossing for weak coupling: Eigenfrequencies of two weakly coupled oscillators as function of detuning $\delta = \omega_c - \omega_e$ (c) Anti-crossing for strongly coupled oscillators, with a frequency splitting proportional to the coupling strength.

harmonic time evolution for positions:

$$x_e(t) = A\sin(\omega_+ t + C) + B\sin(\omega_- t + D) \tag{2.49}$$

$$x_c(t) = -A\sin(\omega_+ t + C) + B\sin(\omega_- t + D) \tag{2.50}$$

The constants are determined by the initial conditions. There exist 2 non-trivial solutions to the equation of motion with frequencies of the eigenstates:

$$\Omega_\pm = \frac{1}{2}(\Omega_e + \Omega_c) \pm \frac{1}{2}\sqrt{\delta^2 + 4g^2} \tag{2.51}$$

with $\delta = \omega_c - \omega_e$ being the detuning and $\Omega_{c,e} = \omega_{c,e} - i\gamma_{c,e}/2$ the complex frequency with the resonance frequency $\omega_{c,e}$ and linewidth $\gamma_{c,e}$. The resonance position of the new hybrid states of the systems can therefore be written as:

$$\omega_\pm = \frac{1}{2}(\omega_e + \omega_c) \pm \mathrm{Re}\sqrt{4g^2 + \delta^2 - (\gamma_e - \gamma_c)^2/4 - i\delta(\gamma_e - \gamma_c)} \tag{2.52}$$

The simple oscillator model captures the transition between the two regimes for different ratios of the coupling strength g and the losses in the system $\gamma_{c,e}$:

- the weak coupling regime ($g \ll \gamma_{c,e}$):

In the extreme case of weakly coupled oscillators, they act as independent oscillators with their frequencies remaining unmodified (Figure 2.6 a) and an exponential decay of their displacement. Even in resonance $\omega_c = \omega_e$ the energy is not efficiently transferred which is reflected in the crossing of the two lines (Figure 2.7 a).

- the strong coupling regime ($\gamma_{c,e} \ll g \ll \min[\omega_{e,c}]$):
  Energy cycles efficiently many times between the two oscillators and leads to the formation of new eigenmodes ω_+ and ω_-. With decreasing detuning of the two resonances an anti-crossing is observed (Figure 2.7 b) with Ω_R (Rabi-splitting) referring to the energy splitting at zero detuning $\delta = 0$.

While experimentally extreme cases of single molecule strong-coupling are already evident[21] key problems remain to maximize the full potential of plasmonic cavities. It is important to note here that with decreasing mode volume the precise and deterministic nano-positioning as well as orientation of the emitter in the nanosized plasmonic cavity becomes more crucial[26,40]. In the case of molecular emitters the reproducible placement of the emitters in the cavity still is challenging due to the use of self-assembly chemistry. The use of quantum dots (QDs) and 2D materials allows a more reliable route to control the orientation and therefore coupling to the emitter.

2.2 2D Materials

A core part of this thesis is dedicated to cavity plasmonics with sub-nanometer spacer materials. One of the main challenges here is to find adequate spacer materials that allow for a precise assembly as well as control over the spacer thickness to achieve reliable yet tuneable cavity systems. Molecular spacer layers that can be fabricated using self assembly are known to provide reliable gaps of just 0.4 nm thickness. Stacking these layers, gap distances of 0.4 up to 2.4 nm have been demonstrated[41]. Nonetheless, making these layers is not straight-forward. The coverage as well as the thickness is very sensitive to the fabrication process. Island growth makes it difficult to achieve a guaranteed homogeneous thickness and degradation over time is a challenge yet to overcome. A newly emerging alternative exploits 2D materials. 2D materials, often referred to as single layer materials, are crystalline materials consisting of stackable single layers of unit cells. They offer unique optical, electronical and mechanical properties and therefore are ideal candidates as versatile spacer materials.
During the past decade 2D materials gained a lot of attention due to their remarkable properties such as high carrier mobilities, superconductivity, mechanical flexibility, good

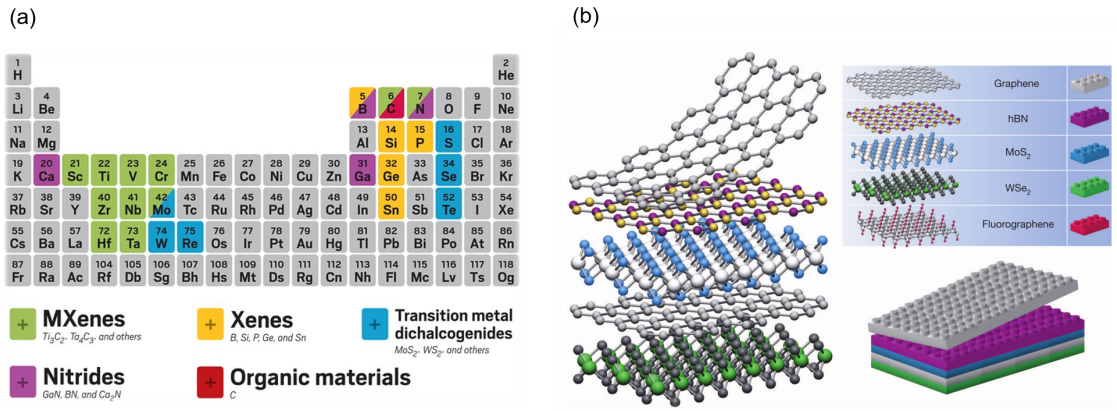

Figure 2.8: **Current library of 2D Materials** (a)"Periodic table" of known layered 2D materials, organized based on the element involved. Focus of this thesis are the transition metal dichalcogenides (TMDs or TMDCs, in blue), which are of the stochiometry type MX_2, with M being a transition metal atom from the group VI (M= Mo, W, etc.) and X a chalcogen atom (X=S, Se, or Te). (b) Nano-Lego: Schematic illustrating stackability of a variety of 2D layers which act as building blocks to combine different material properties. Overview of 2D Materials taken from[42] and[43].

thermal conductivity, as well as high optical and UV absorption.

The wealth of available materials is impressive. First traces of 2D materials in literature date back more than 60 years[44]. While there were studies of layered materials it was only in 2004 that the discovery and characterization of a monolayer of graphene caused some commotion and was awarded the Nobel prize in 2010. What started off with single element layers of graphene now extends to a big family of atomically thin van-der-Waals materials such as phosphorene, borophene, germanene and silicene and mixed element compositions such as hexagonal boron nitride (h-BN) and transition metal dichalcogenides (TMDs) as well as 2D oxides[45] (Figure 2.8 a). The family of 2D materials offer properties that range from somewhat distinct to graphene to yet complementary and similar. This allows for generalising of the experimental and theoretical framework for 2D materials.

Van-der-Waals materials distinguish themselves from other solid materials through their stackability (Figure2.8 b). Strong covalent bonds provide in-plane stability of 2D crystals, however the individual layers are held together by relatively weak van-der-Waals-like forces[43]. The ability to stack isolated atomic layers of different materials into carefully designed hetero- and homo-structures, choosing the sequence layer by layer, completely tailors their properties. With steadily improving fabrication techniques the different 2D layer materials function as "nano Lego Building blocks" giving rise to a zoo of interesting physical phenomena, such as valley polarization, superconductors, room-temperature excitonic superfluidity[43,46,47]. While there exist many different 2D materials that can be incorporated into plasmonic cavities, in this thesis the main focus is on TMD materials due to reasons that will become more evident in the next section.

2.2.1 Transition Metal Dichalcogenides (TMDs)

TMDs are atomically thin semiconductors of the stoichiometry type MX_2, with M being a transition metal atom from the group VI (M= Mo, W, etc.) and X a chalcogen atom (X=S, Se, or Te). One layer of M atoms is sandwiched between two hexagonal planes of X atoms (Figure 2.9 a). The overall symmetry of TMDs is hexagonal (2H),

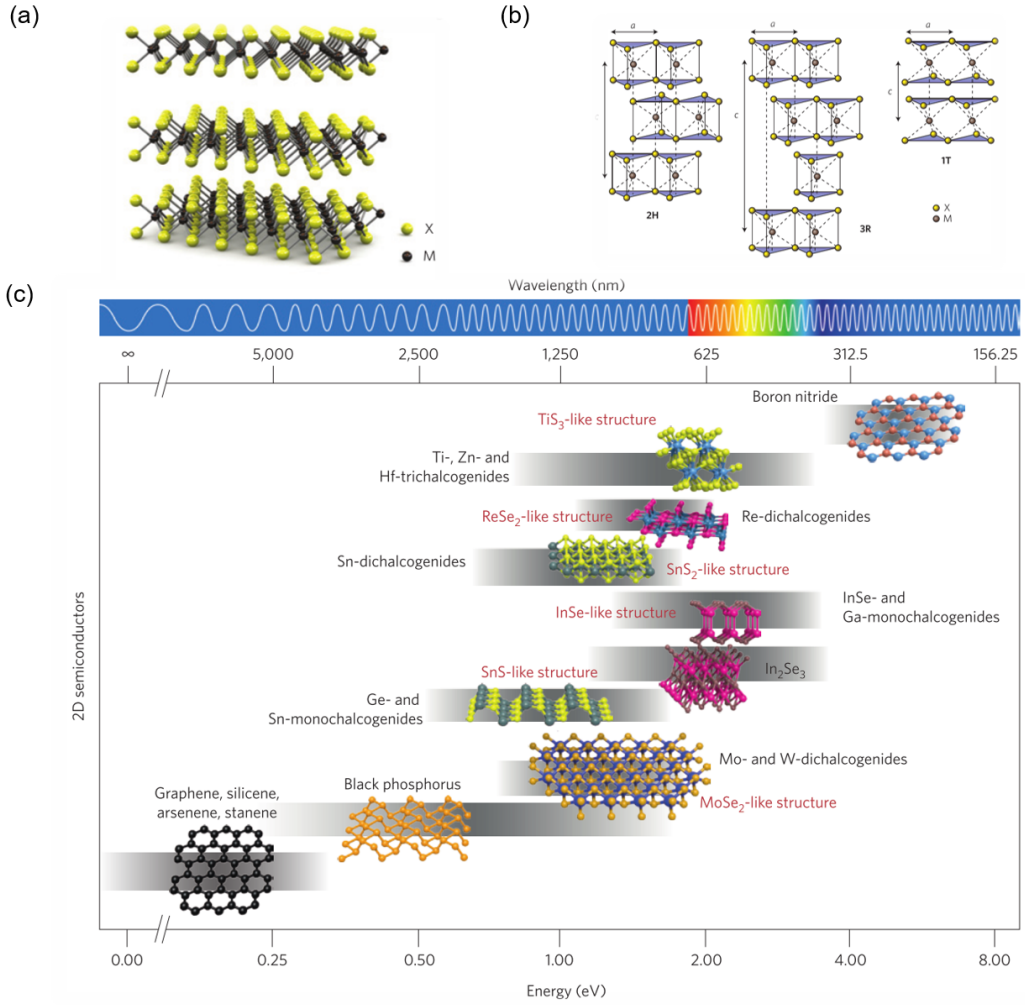

Figure 2.9: **Transition metal dichalgoenides** (a) A schematic illustration of the stoichiometry of TMDs: MX_2, with M being a transition metal atom (black) from the group VI (M= Mo, W, etc.) and X a chalcogen atom in yellow (X=S, Se, or Te).Taken from [48,49] (b) Existing types of structural symmetries: hexagonal (2H) with 2 layers per unit cell, rhombohedral (3R) with 3 layers per repeated unit and tetragonal (1T) 1 layer per unit. (c) Comparison of band gap energies for different semiconducting 2D Materials with the crystal structures displayed respectively. Band gap engineering realized through strain, number of layers or dielectric surrounding is indicated with grey bands. Figure is taken from [47].

rhombohedral (3R)or tetragonal (1T) with a layer separation of around 6-7 Å and lattice constants a ranging from 3.1 to 3.7 Å [49] as shown in Figure 2.9(a). The separating metal atoms have octahedral or triagonal prismatic coordinates[49]. These materials have an

intrinsic bandgap within the visible part of the spectrum. WSe_2 and MoS_2 have bandgaps of 1.75 eV and 2 eV respectively[50]. This may vary with strain[46], number of layers[51] or dielectric surrounding[50] and is known as band gap engineering[47]. Its unique and versatile properties allow for a variety of applications in fields including catalysis, energy storage, sensing, nano electronic devices, all-optical switches and superconductors[46,48,50]. However, most of these properties rely on very high quality layers. Different approaches are used to achieve high quality small flakes or large flakes with uniform properties. Some of the widely used methods are summarized in the next section. Giving an overview of all the methods in this context would be beyond the scope of this thesis but can be found elsewhere:[45,52].

2.2.1.1 Synthesis of TMDs

There exist many different methods to fabricate TMDs with varying dimensions, shape and quality, but only a few that allow for mass fabrication are scalable. Each of the following method presented has its advantages and drawbacks ranging from high quality flakes that are expensive but rather small, to large area flakes with lower quality (Figure 2.10).

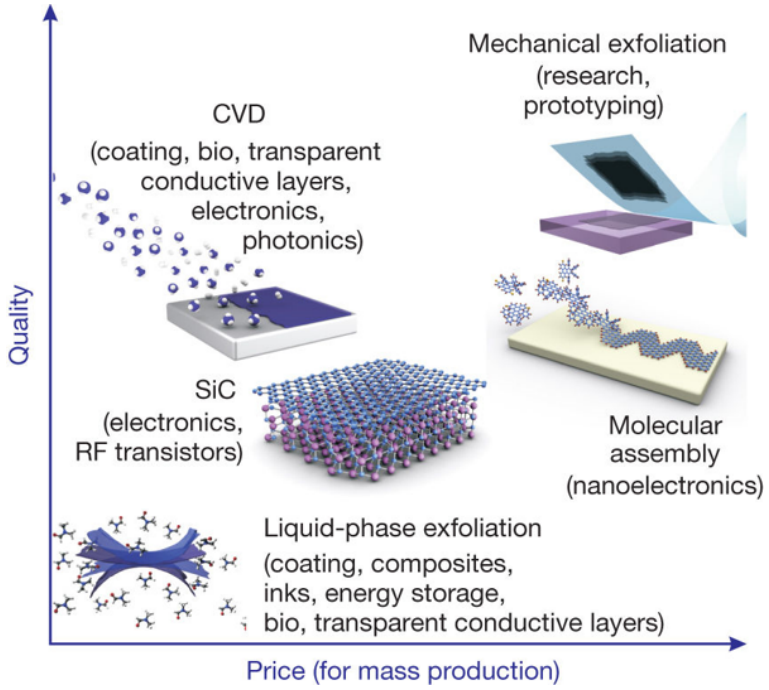

Figure 2.10: Different fabrication methods to mass produce graphene. Similar strategies are employed to fabricate 2D materials. The wide range of mass-production methods allow a wide choice in terms of size, quality and price for particular applications. Image taken from[53]

- top-down exfoliation:
  Mechanical exfoliation from bulk crystals: Using bulk crystals, atomically thin flakes of TMDs can be stripped off individually using adhesive stamps or tape. While this allows the generation of very high quality flakes with very low contamination, scalability and reliable control of the thickness remain a challenge. Mechanically exfoliating the flakes and carefully placing them on a substrate produces flakes of random sizes and thickness. Furthermore, only specific substrates with certain adhesive properties can be used to directly stick the exfoliate flakes onto the substrate. Substrates such as gold and silver, which are used within this thesis require transfer methods to deposit the flakes that further complicate the process.
  To generate larger flakes chemical exfoliation shows a higher yield. Here, the intercalatation of TMDs with ionic species such as lithium separates the individual layers. However, the resulting exfoliated flakes differ substantially in their electronical and optical properties from the bulk material.
  Liquid phase exfoliation: While mechanically exfoliated flakes produce the highest quality monolayer samples, liquid phase exfoliation methods result in lower quality flakes but have a high yield and can therefore be used where larger quantities are needed. Typically the flakes are exfoliated in a solvant by sonication[48]. In this case the solvant or surfactant has surface energies comparable to the cohesion energy of the material in order to overcome the cohesion energy between the stacked layers.

- bottom-up synthesis:
  Chemical vapour deposition: Another method to obtain large wafer scale flakes is chemical vapour deposition (CVD). Using a metal substrate as catalyst the individual atoms are epitaxially grown. The outcome and thickness of the atomic layers highly depends on the exact pressure, temperature and concentration as well as composition of precursors and therefore need careful adjustment. Major disadvantages of this technique are the smaller domain sizes, the higher impurity concentration and the greater defect density of the flakes, that act as scattering centres in the optical response.
  Atomic layer deposition: Atomic layer deposition (ALD) is a thin-film deposition method based on surface chemical reactions. Precise thin-film thickness control and high conformity are achieved by surface self-saturated reactions. One cycle consists of 4 steps: (a) precursor exposure, removing the unreacted precursor with inert gas, exposure and removing of a counter reactant and byproducts[54].

Incorporating 2D material flakes into the nanoparticle on mirror system requires high quality flakes with very view defects. Furthermore, the flakes need to be transferred to

gold and silver substrates in order to allow for the formation of the plasmonic cavity. For these reasons mainly exfoliated flakes of WSe_2 and MoS_2 have been used within this thesis, where the exact sample preparation is described in section 3.3.3.

2.2.1.2 Electronic Structure and Optical Properties

In the following section the most important optical and electronic properties of TMDs are briefly discussed with major focus on WSe_2 and MoS_2 since these are used within this thesis.

Bandstructure and Valleytronics

Generally MoX_2 and WX_2 compositions are semiconductors and NbX_2 and TaX_2 are metallic. The typical optical response of a 2D semiconductor is show in Figure 2.11 a. Due to the Coloumb-interaction between the electrons and the holes, new bound states below the band gap emerge. These states are called excitons (labelled as $n = 1, 2..$) and their energies can be modelled similarly to the hydrogen atom. An attractive feature of TMDs are their large exciton binding energies. These are defined as the differences between the bandgap E_{gap} and the exciton resonances energies. Binding energies exceeding $\geq$ 300 meV make TMDs stable room temperature candidates paving the way for realistic excitonic devices. Furthermore, the reduced dimensionality of the excitons in a 2D layer results in a reduction of the dielectric screening of the Coulomb interaction leading to higher binding energies[56]. Stacking another TMD monolayer on top of 2D semiconductors can therefore change the dielectric screening on atomic length scales, tuning the band gap energy and well as the exciton binding energies (Figure 2.11 b).
The emerging 2D semiconductor not only allows the study of room temperature excitons, but also interesting phenomena such as the generation and dynamics of charged excitons (trions, bi-excitons)[57,58] or valley-polarized photoluminescence emission[47,50,59] The latter stems from the large spin-orbit interaction in these compounds, due to the heavy transition metals where the spin-degeneracy of the valence bands is lifted. This leads to a splitting of the valence band that strongly affects their optical spectra opening up a new field of "'valleytronics"' (Figure 2.11 c). The two resulting transitions between the maxima of the split valence bands and the minimum of the conduction band at the K and K' point of the Brillioun zone are called A and B excitons (Figure 2.11 c,d). The spin up state at the K valley is degenerate with the spin-down state at the K' valley. The large splitting results from the lack of inversion symmetry, the high mass of the elements in the MX_2 structures and the confinement of the electron movement in-plane. The large spin-orbit splitting allows for spin-polarized carrier populations which form the foundation of the valley- and spin-dependent optical and electronic properties. Using circular polarized light the carrier populations in distinct valleys can be controlled and

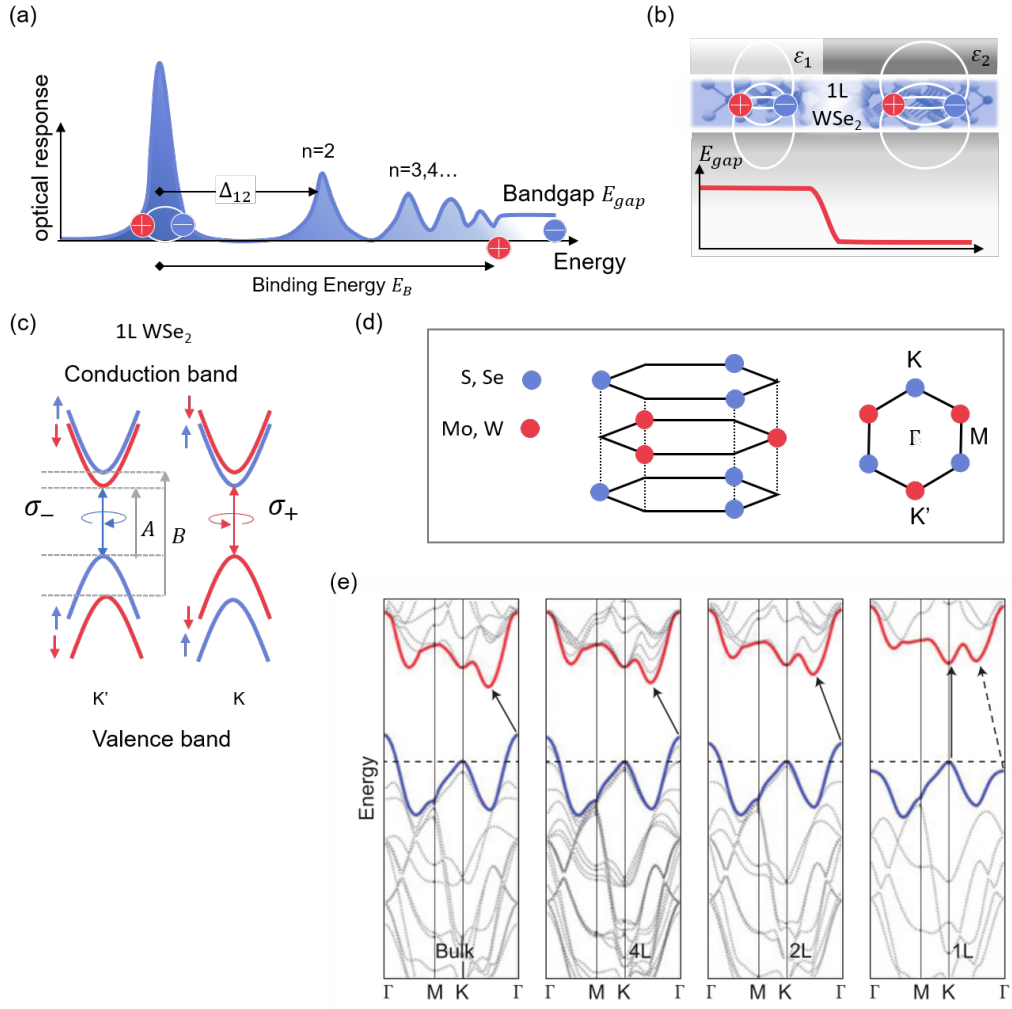

Figure 2.11: **Bandstructure of WSe_2 and MoS_2**S (a) Schematic of a typical optical response of a 2D semiconductor and (b) band gap engineering. By partially covering the 2D layer with an ultra-thin dielectric layer the environmental dielectric screening is modulated on atomic length scales, effecting the band gap energy and well as the exciton binding energies. (c) Trigonal prismatic structure of monolayer TMDs with the high-symmetry point of the Brioullin zone. (d) Electronic bandstructure for WSe_2 at the K and K' points, which are spin-split by the spin-orbit interactions. The spin (up and down arrows) and valley (K and K') degrees of freedom are locked together and lead to valley-dependent optical selection rule ($\sigma_+\sigma_-$). (e) Example calculation of MoS_2 bandstructure: Energy dispersion (energy versus wavevector k) in bulk, quadrilayer (4L), bilayer (2L) and monolayer (1L) MoS_2 from left to right. The horizontal dashed line represents the energy of the valence band maximum at the K point. The red and blue lines represent the conduction and valence band edges, respectively. The lowest energy transition is indicated by the solid arrows. In the case of the monolayer the indirect transition of the Γ-K point (dashed arrow in 1L plot) is overpowered by the direct (vertical) K-K transition. Figure is taken from [55],(d) Bandgap engineering of 2D Materials, taken from [56]

manipulated[49] (Figure 2.11 c). Furthermore, the different bonding mechanisms in and out of plane of the atomically thin layers make these materials also highly tuneable with number of layers. It has been shown experimentally as well as theoretically that due to the quantum confinement in the direction perpendicular to the layer plane, a tran-

sition from direct band gap to indirect gap can be observed as the number of layers is increased from monolayer to multilayer[47]. An example of this transition is depicted in the calculated band diagram of MoS_2 (Figure 2.11 e). The arrows indicate the excitonic transitions A and the direct and indirect bandgaps at E_g and E'_g.

While the direct band gap is located at the K-point, which is located at the edge of the Brillouin zone (Figure 2.11 d), this gradually changes with increasing number of layers where the indirect transition becomes more dominant. The conduction band minimum at the Γ- point shifts towards lower energies with increasing number of layers competing with the direct transition. The change in the band structure originates from the change in hybridization between p_z orbitals of the S (Se) atoms and the d-orbitals of the W (Mo) atoms[49]. Experimental studies have demonstrated that already with two layers the indirect transition can dominate over the direct transition[51]. Density functional theory (DFT) simulations show that the states at the conduction band K-point are caused by the localized d-orbitals of the W (Mo) atoms. Compared to the states near the Γ-point these states remain relatively unaffected with number of layers. Changing the number of layers therefore leads to a transformation at the Γ-point from an indirect to an increasing direct transition while the direct transition at the K-point remains unchanged. Furthermore, besides changing the number of layers it has been experimentally shown that factors such as temperature[51] and pressure[60], mechanical strain[61], doping[62] as well as external electrical fields and dielectric screening[56] can be used to induce changes in the band structure and therefore alter the electronic properties and optical response.

While there exist a wide range of TMDs which have different properties ranging from insulating to semiconducting all the way to metallic properties and the individual TMDs are tuneable with the number of layers an even more versatile approach of stacking different TMDs has emerged during the past decade. These heterostructures form the basis of "nanoscale lego"[43,45]. The basic principle is simple: take a monolayer, put it on top of another monolayer or few-layer crystal, keep adding layers in a chosen sequence until the desired functionality is achieved. The resulting stack represents an artificial material assembled where the atomic layers are used as Lego- building blocks with atomic precision. In contrast to conventional, epitaxially grown heterostructures, there is not only a discontinuity of the band structure, leading to energy barriers, but also of the density of states (DOS) which results in an additional resistance at the junctions[63]. Furthermore, an additional degree of freedom, the twist angle between layers, requires careful alignment, as it drastically alters the optical and electronic properties[64].

2.3 Conclusion

In this chapter the groundwork to explore light-matter interactions at the nanoscale was laid. The optical response of metals was derived using Maxwell equations and the Drude-model. In particular plasmonic metals that confine light below the diffraction limit were explored and the behaviour of light at these length scales was discussed. The framework is then extended to describe plasmonic coupling, introducing the concept of plasmonic cavities. Important consequences of strongly confined light which is accompanied by high local field enhancement were reviewed and specifically light-matter interactions in the strong coupling regime was discussed in detail. A classical description of two harmonic oscillators is introduced to define key parameters of the strong coupling regime.
In a second section 2D materials are introduced and their unique optical and electronic properties as well as the most common fabrication methods are summarized.

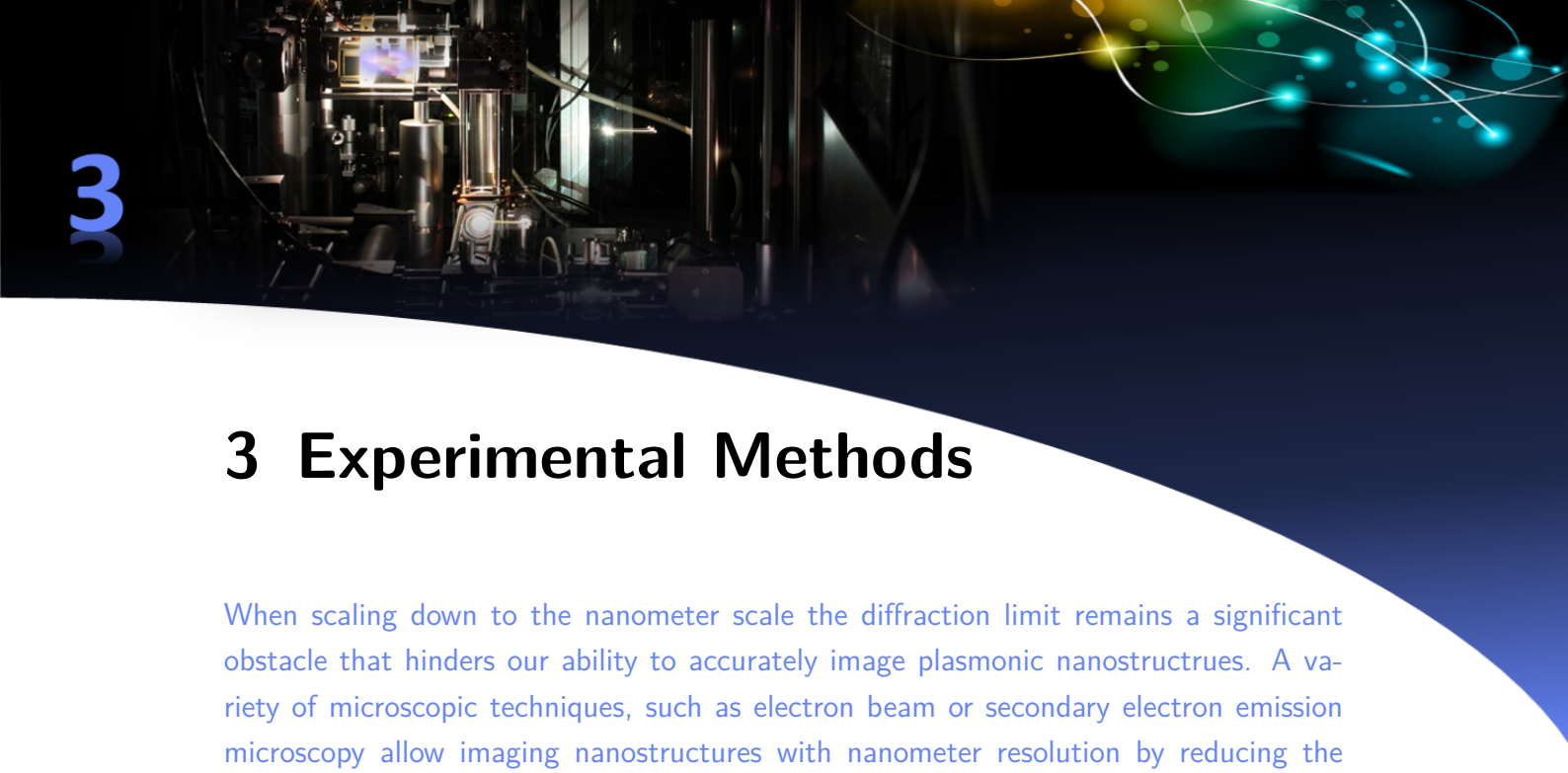

3 Experimental Methods

When scaling down to the nanometer scale the diffraction limit remains a significant obstacle that hinders our ability to accurately image plasmonic nanostructrues. A variety of microscopic techniques, such as electron beam or secondary electron emission microscopy allow imaging nanostructures with nanometer resolution by reducing the probing wavelength thus reducing the diffraction limit. Nonetheless, these techniques are costly and invasive, therefore making systematic and reproducible studies difficult. Dark-field microscopy provides a non-invasive and versatile alternative and is the main technique used within this thesis. It enable the imaging of nanostructures with dimension < 5 nm without damaging the structure[12].

This experimental methods chapter contains three parts. The first part summarizes different dark-field microscopy techniques and gives an overview of the custom-built dark-field setup that was developed during this thesis. Furthermore other essential experimental techniques are briefly discussed. The second part describes the numerical methods that were used to simulate nanostructures in order to gain a better understanding of the light-matter interaction at the nanoscale. Finally the third part focusses on fabrication techniques and sample preparation.

3.1 Dark-Field Spectroscopy

One of the major problems encountered when using a conventional bright-field microscope is the poor spatial resolution. Here, volumes much larger than the individual nanostructure are probed. This leads to a massive background caused by the reflected incident light from the gold surface of the nanoparticle on mirror (NPoM) constructs. The reflected background is several orders of magnitude higher than the signal from the nanostructures. One possible way to reduce the background is blocking the directly reflected light by a beam block. This is realized by shaping the incident light in an annular ring. The shaped light is then focused onto the sample via an objective (Figure 3.2 a). At the sample the light is either absorbed, via non radiative pathways, reflected or scattered from the nanoscale objects. The reflected light is blocked by an iris after the objective, enabling the background free detection of the scattered light. Particles on

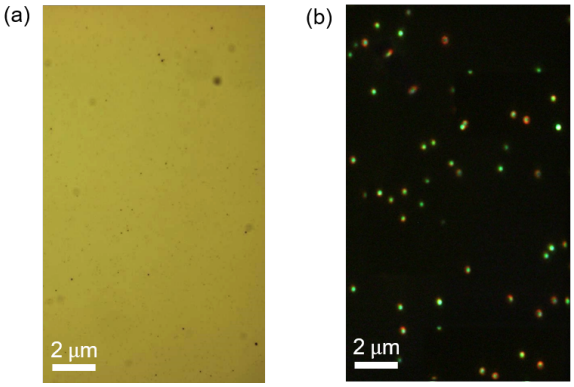

Figure 3.1: **Imaging on the nanoscale**. (a) Typical bright-field and (b) dark-field image of a nanoparticle on mirror (NPoM) Sample with 80 nm nanoparticles on a gold substrate and 0.9 nm spacer layer. White scale bar indicates 2 μm.

the substrate thus appear as bright diffraction-limited spots on a dark background (Figure 3.1 b)[65] in contrast to bright-field images where the particles appear as dark spots on a bright background (Figure 3.1 a).The dark-field microscopy that was performed during this work was carried out on two different dark-field microscopes. A dark-field setup which was developed during this thesis (Figure 3.2 a) and a modified commercial Olympus BX51 upright microscope (Figure 3.5). While the commercial microscope was mainly used for particle tracking which allows the measurement of many hundreds of nanoparticles constructs per night, the home made dark-field microscope was used for more elaborate and specific measurements, where modification of the setup itself was necessary. Furthermore, seemingly subtle differences in the illumination path of the two setups lead to substantial differences in their characterization performance. This will be elaborated in detail in the following sections.

3.1.1 Custom Built Dark-field Setup

A simplified version of the beam path of the custom built microscope is shown in Figure 3.2 a). To allow for background-free detection of the scattered light, a typical dark-field configuration consists of two complementary beam blocking elements. A beam block and iris diaphragm or two bowtie beam blocks rotated 90 degrees (inset in Figure 3.2 a), dashed boxes) allow the excitation and detection of complementary angles. The shaped incident light (blue beam path) is guided to the sample using a beamsplitter and focused to a diffraction limited spot by a high NA objective. Using a high NA objective allows for optimal coupling to the NPoM constructs, which have their maximum emission angle around 65 degrees in respect to the surface normal. For lower NA objectives the NPoM is not efficiently excited as the incident light has no field components oscillating parallel to the plasmonic dipole orientation (This is not the case for nanoparticle dimers as here the plasmonic dipole lies within the sample plane). The detection beam path (yellow) consist of a fiber coupled spectrometer and a CCD camera. The scattering response of nanostructures as a function of wavelength is recorded with the spectrometer and the CCD camera is used to image the area of interest.

Operating Modes

The setup can be operated in two different modes, one to minimize chromatic aberration and one to maximize versatility. In the two modes the beam blocking elements can either be placed as close as possible to the back focal plane of the objective or a 4f-imaging configuration can be used to re-image the beam block onto the back focal plane. Through exchanging lenses at the correct planes the setup can be switched between operating modes. The first mode uses fewer lenses and minimizes chromatic aberrations. It is also mechanically more stable due to compactness of the dark-field unit. However, the 4f-configuration has proven to be more versatile in its operation as well as easier to align. Here the beam is re-imaged onto the back of the objective using the 4f-configuration as indicated in Figure 3.3. This allows the incorporation of spatial filters in the correct planes for a better alignment of the beam. It also facilitates the access to the beam block that is projected onto the back focal plane, which is typically inaccessible under the objective holder and very complicated to replace. Therefore, in this configuration different dark-field techniques (annular or bow-tie shown in the inset in Figure 3.3 a) can be easily exchanged without having to realign the beam path. Being able to switch to bowtie-configuration using the same objective allows the excitation and collection angles to be extended and overlapped. In the case of the NPoM, where the optimal in-and out-coupling is expected to be around $\theta \sim$65 degree[66] this becomes crucial as the angles are limited by the NA of the objective and further reduced using

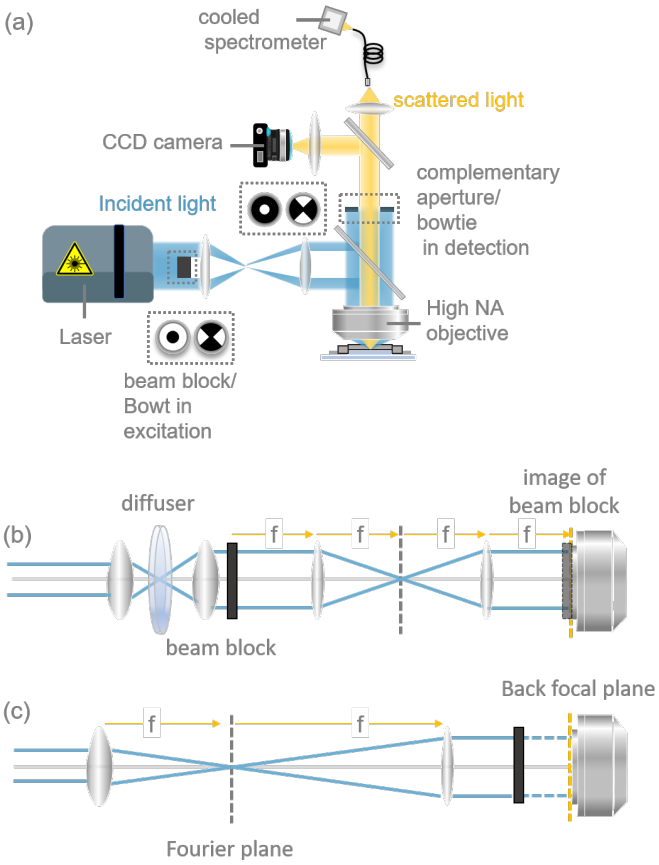

Figure 3.2: **Dark-field configurations and Operating Modes.** (a) Simplified Illustration of the built dark-field microscope beam path. (b) Beam block is re-imaged onto the back-focal plane of the objective using two lenses. Using the 4-f configuration allows for access of the image at the back-focal plane as well as easy alignment of the beam path. (c) Beam block is as close as possible to the back focal plane of the objective, making the system mechanically very stable. The beam is expanded to fill the back aperture and focus the beam to a diffraction limited spot.

an annular beam block[67]. Having the full angular information available allows the angle dependent emission characteristics to be mapped out without employing complicated hyperspectral imaging techniques. Furthermore, an additional diffuser in the excitation beam path is used to minimize artifacts in the dark-field images due to speckles and beam inhomogeneities as well as to increase the field of view.

Supercontinuum Laser as Light Source

A 4W pulsed supercontinuum Fianium SC400-4 Laser is used as a light source. The supercontinuum is generated through temporal and spectral broadening of a source pulse in a non-linear single mode photonic crystal fiber. The pump laser is a Nd:YAG laser ($\sim$ 5 picoseconds, $\lambda = 1064$ nm, repetition rate 40 MHz).This results in a broadband, near-Gaussian, collimated output beam that is several hundred picoseconds long. Operating

it at full power it can reach an average spectral power density of $\sim 2\,\mathrm{mW/nm}$.
Its high light levels allow for integration times as short as 10 ms over a wavelength range of 450 to 1200 nm. Referencing of this source spectrum is taken from reflecting of gold substrate, choosing a position far away from any nanostructures.
While the spectral range of the Fianium reaches the NIR (400-2100 nm) the bandwidth is limited by the optical components used to guide the Fianium in the illumination and detection beam paths, limiting it to around 450-1000 nm. Most lenses and beam splitters operate in the wavelength range of $\sim$ 400-800 nm, quickly dropping off beyond that. To extend that range the lenses can be optionally changed to IR lenses.

The beam path of the custom built dark-field setup is shown in Figure 3.3. The setup is shown in the 4-f configuration mode where a beam block is re-imaged at the back focal plane of the objective. The laser beam is expanded to fill the one inch optics using 2 lenses and the annular beam (blue) is produced by a ring shaped light stop. It is re-imaged to the back focal plane of the objective using lens $L1$ and $L2$ ($f_{1,2}$=150 mm). The incident polarization can optionally be set and rotated by a half-waveplate. A beamsplitter (BS) is used to direct the light to the objective where it is guided through the periphery of the bright-field objective and focused down onto the sample. The scattered light (yellow) is collected in the inside angular cone and re-imaged (4-f configuration) onto a fiber-coupled spectrometer allowing confocal detection. The reflected incident light is blocked by an aperture after the beamsplitter. As mentioned before the annular beam block and aperture can be exchanged for bowtie beam blocks. In the confocal configuration the scattered light is focused onto a 50 μm multimode fiber guiding the light to a peltier-cooled Ocean Optics spectrometer.
Using a fiber before the spectrometer increases the spatial resolution. The fiber acts as a pinhole in the detection, filtering out light that does not originate from the focal spot. Hence, for low density samples the contribution of individual nanostructures can be measured. The increased spatial resolution reveals modifications in the optical response caused by local changes in structural parameters as well as refractive index variations that would otherwise be averaged out[68]. While 90% of the scattered light is focused onto the spectrometer with a 100 mm focal lens a 90:10 beamsplitter after the beam block is used to split 10 % of the scattered light from the sample and image it on to a CCD camera. This allows to position individual NPoM constructs into the centre of the confocal detection.

Field of View

The laser is focused down to a diffraction limited spot, allowing individual single nanoparticle constructs to be addressed for samples of sufficiently low density. Nonetheless, this goes hand in hand with a very limited field of view, which is necessary for particle track-

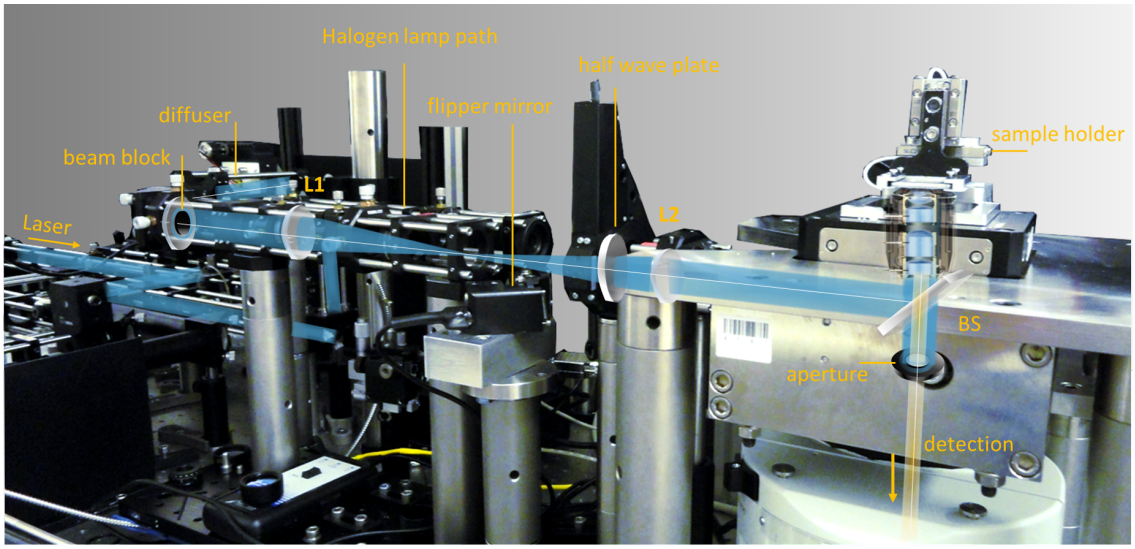

Figure 3.3: **Custom built Dark-field Setup** Photograph of Experimental setup. Part of the excitation beam path and detection beam path are overlayed on top of the image in blue and yellow respectively. The setup is shown in the 4-f configuration mode where a beam block is re-imaged at the back focal plane of the objective. The annular shaped beam (blue) is produced by a ring shaped light stop and re-imaged using lens L1 and L2. The incident polarization is is rotated by a half-waveplate and a beamsplitter (BS) is used to direct the light to the objective where it is guided through the periphery of the dark-field objective and focused down onto the sample. The scattered light (yellow) is collected in the inside angular cone and re-imaged onto a fiber-coupled spectrometer allowing confocal detection. The incident light is blocked by an aperture after the beamsplitter.

ing. If desired, a wider field of view can be achieved by exchanging the beam expander with a rotating ground glass diffuser in the excitation beam path (Figure 3.3. Using short focal length lenses the beam is focused on to the frosted glass diffuser, which is rotated by a stepper motor. The large spatial coherence length of lasers produces speckles, degrading image and spectra quality. The scattering from a moving diffuser adds a random phases to different parts of the beam, destroying its spatial coherence and homogenizing the beam spectrally as well as increasing the spot size on the sample[69]. While this also decreases the power density of the beam it can be accommodated for by increasing the laser output power. For an even larger field of view the additional xenon lamp can be used for dark-field imaging. Using a flippable mirror in the k-space plane the beam path can be switched between coherent laser excitation and incoherent illumination with an ultra-bright xenon lamp. By the means of this flipper mirror one can be switched in and out running fully automatized between measurements. While the xenon lamp produces good quality dark-field images, low light levels and atomic lines in its spectrum render it unsuitable for fast acquisition of dark-field spectra.
Three different bright-field objectives can be used to allow for different excitation and detection angles.

- A short working distance, 63x magnification, water immersion, 1.2 NA Leica objective allows for high angle excitation (θ_E=55-64 degrees) and detection (θ_D = 0-55 degrees) with large bandwidth (λ=500-1000 nm). This is used for imaging nanostructures immersed in a liquid medium as well as polarization dependent measurements.

- A long working distance, 50x magnification air-immersion, 0.8 NA Olympus objective with angles ranging from θ= 0-53 degree and a spectral bandwith (λ=500-850 nm).This is used for samples that can not be placed on top of a cover slip and require a longer working distance.

- A 100x magnification Oil immersion, 1.4 NA Nikon Objective with incident angles ranging from θ_E=67-79 (0-79 bowtie configuration) and detection angles θ_D=0-67 degrees (0-79 bowtie configuration). This is used for ultra high angle excitation and detection and to image through gold coated cover slips with nanostructures on the top side.

After passing through the objective, the reflected incident light is blocked using either a motorized aperture close to the objective or a complementary beam blocking element in the image plane. In case of a diaphragm the diameter of the aperture needs to be adjusted according to the size of the beam block used. The background-free scattered light is then detected at the complementary angles. The scattered light is normalized by subtracting the background and dividing by a reference spectrum. Subtracting the background accounts for background scattering and electronic noise while the reference is used to take out the spectral shape of the light source as well as to account for the spectral detection efficiency. The background is taken with a fully closed aperture using the same integration as the actual measurement. The reference spectrum is taken with the aperture fully open.

3.1.1.1 Polarization-Dependent Dark-Field Scattering

Introducing a polarizer into the excitation beam path allows the polarization response of individual nanostructures to be measured. To ensure that the incident light is linearly polarized the polarization is set by a grid polarizer (GP) with a spectral range of 300-1000 nm. It is then rotated by ϕ at the back focal plane of the objective by an ultra-broadband zero-order half-wave plate (HWP, Figure 3.4) to retain polarization

purity at the sample. Using an incoherent light source leads to polarization components in the s- and p- plane (Figure 3.4 a). When focused down on to the sample the polarization components add up. This leads to polarization component parallel to the substrate as well as along the z axis due to the high angle excitation. The z-fraction of the polarization scales with the NA of the objective; lower NA objectives have small polarization components oscillating along the z axis while large NA objectives lead to large z polarization and therefore efficiently couple to the plasmonic dipole of the NPoM system.

However, using a supercontinuum laser, which possesses a coherence length of approximately 3 mm leads to light in the focal spot that is dominantly s polarized with the field components oscillating parallel to the substrate. This is due to out-of-phase superposition (Figure 3.4 a). When carefully aligned, the mixed p-polarized components coming from two opposite sides of the incident annular cone cancel out due to the out-of-phase superposition of these beams (Figure 3.4 b), orange). The remaining constructively-superimposing components are s-polarized in the azimuthal plane (Figure 3.4 b), with a direction set by the incident polarization direction (Figure 3.4, white). Combining the two light sources therefore allows the full 3-D polarization response of single nanostructures to be collected.

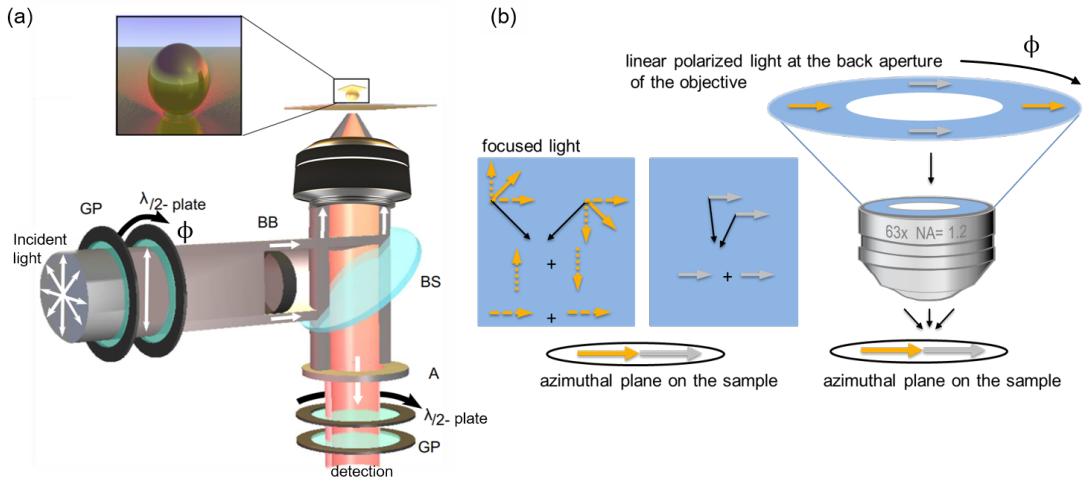

Figure 3.4: **Polarization dependent dark-field microscopy** (a) Polarization-dependent dark-field microscope. The polarization of the supercontinuum laser in set with a wire-grid polarizer (GP) and a $\lambda/2$ plate to rotate the linear polarization in the excitation beam. Using a beam splitter (BS), the light is focused onto the sample through a high NA (1.2) water-immersion Leica objective (63x magnification). A beam block (BB) in the incident beam path and an aperture (A) in the detection allow for background-free detection of the scattering. (b) Realization of polarization in the azimuthal plane: p-polarized components cancel out due to the out-of-phase superposition of the beams from opposite azimuthal directions on the cone (orange), while s-polarized components add (grey).

3.1.1.2 Photoemission and Laser-Induced Tuning

To carry out simultaneous photoluminescence (PL) and dark-field measurements an additional beamsplitter port in either the excitation or detection beam path can be used to couple in a monochromatic continuous wave (CW) laser into the microscope. The 403 nm laser diode is coupled in via free space and collimated with multiple lenses to guarantee the even illumination of the back focal plane of the objective. If the laser is coupled in via the detection beam path it illuminates the sample at normal incidence, however, if the excitation path is used the beam is focused down at high angles, because the beam must pass through the complementary k-space masks in each path. A 500 nm long-pass filter before the spectrometer is used to block out the laser light and allows for the simultaneous detection of PL emission and dark-field-scattering. For high laser powers light induced restructuring of the nanoparticles is observed.

3.1.2 Olympus BX51

The optical path of a commercial BX51 is shown in Figure 3.5. The illumination path and the detection path are overlaid in blue on top of the microscope image. An ultra bright halogen lamp in combination with a dark-field objective is used to illuminate the sample. A homogeneous illumination is realized by the reflective Koehler configuration, where the sample and light source are in two conjugated planes. This illumination technique prevents the projection of the light source image on to the sample plane[70] ensuring that the image of the individual filaments of the halogen lamp is defocused over the sample. The result is an extremely homogeneous and even illumination over the entire imaging area. As indicated there are two irises: one in the aperture stop (AS) which together with the back focal stop (BFS) are reciprocal to the sample plane and one in the focal stop (FS), which is conjugate to the sample plane. At the AS the image of the light source is reproduced using a lens. Closing the iris in the AS plane blocks the outer light, which allows the incident angles of the incoming light to be reduced. On the other hand, the FS iris can be used to centre the illuminated area on the sample at the camera. It is placed after a second lens so it is conjugate to the sample plane and therefore in focus at the same time as the sample. With a third lens the light is then projected onto the back focal plane, fully filling the back aperture of the dark-field objective. Before the light reaches the objective an annular mirror (3.5 b) is used to cut out the middle of the beam to ensure the annular shaped high angle illumination. For a 100x 0.9 NA Olympus objective incident angles of θ=58-64 degrees are realised. The schematic of a dark-field objective is shown in Figure (3.5 c). The incident light in form of a ring produced by the annular shape mirror is projected onto the back focal plane

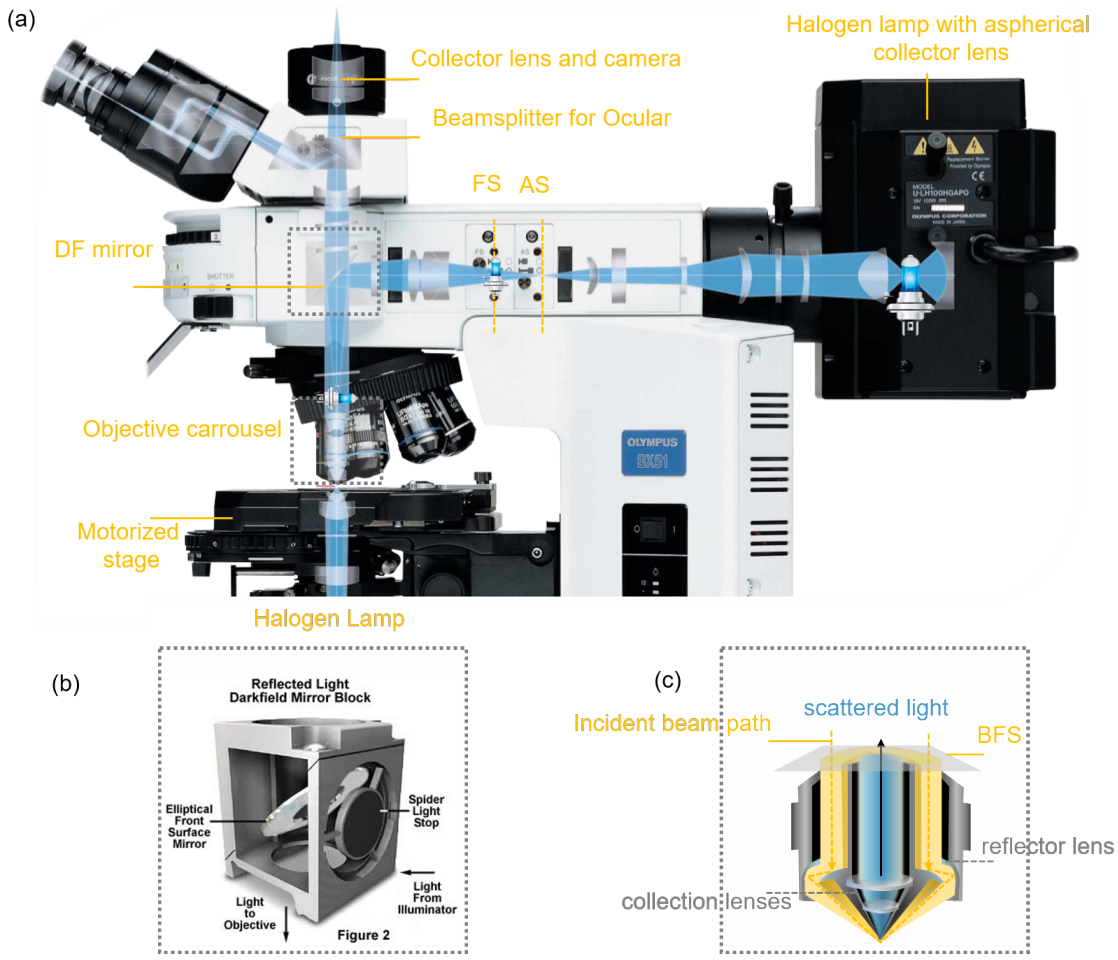

(a) DFSetupA

Figure 3.5: **BX51** (a) Schematic of the commercial BX51 setup with overlayed beam path in blue. Detection path way is not shown. (AS) and (FS) label Aperture and Focal stop respectively. (b), (c) zoomed in images of the inside of a dark-field mirror and dark-field objective used in the BX51 to allow for background-free detection of dark-field scattering. The doughnut shaped beam (yellow) is produced by an Elliptical Front Surface Mirror in combination with a Spider Light Stop and guided through the periphery of the dark-field objective where it is focussed down onto the sample with a reflector lens. The scattered light (blue) is collected in the inside cone. Images (a) and (b) reproduced and modified from [71]

of the objective. Different objectives are mounted on a carousel, which allows for easy exchange of objectives without misaligning on the sample. In the objective the light is guided along the periphery and a reflector lens is used to focus the light onto the sample in a large spot under high angles.The scattered light is collected through the inside cone of the objective with a collection lens.

Since the scattered light is collected with the same objective the detection angles are limited to smaller angles below the illumination cone θ=0-58 degrees, corresponding to 0.85 NA=$n\sin(\theta)$. After being reflected from a beamsplitter the returning scattered light from the sample is focussed onto a 50 μm multimode fiber guiding the light to a

peltier-cooled spectrometer in confocal configuration.
Optionally two additional beamsplitter ports in the illumination path serve as an extra input for external light sources or an easily accessible output from the illumination beam path without having to modify the imaging path. In combination with a shutter (Uniblitz) in front of the halogen lamp this allows alternating photoemission and dark field scattering studies to be carried out on the same nanostructure (see section 6)
The use of a halogen lamp in the excitation has many advantages such as the large and even illumination area, which is ideal to carry out large-scale automated scans of many different structures on one sample, but it also has its limitations. The large area illumination results in very low light levels, requiring integration times of seconds. It also does not allow the excitation of individual nanostructures. Furthermore the spectral range of the halogen lamp is limited to the visible range (500-830 nm). Monitoring fast changes in dark field scattering across the visible and the near IR simultaneously demands a system with higher light levels for fast acquisition and a broader spectral range. This was realised by using a super continuum Fianium laser as a light source, which forms the heart of the custom built dark-field setup described in the previous section.

3.2 Simulations

In addition to experiments, numerical simulations offer a rich tool set that can provide important insights into the optical response of plasmonic nanostructures and their coupling. In particular, simulations allow us to explore coupling and scattering mechanisms in a level of detail that remains inaccessible experimentally. The most commonly used numerical methods are the **Boundary Element Method** (BEM), **Finite-Difference Time-Domain** (FDTD) and **Finite Element Method** (FEM) and a brief overview is given in the following:

- BEM:
  The BEM method is an integral equation method that is generally based on solving Greens functions. These Greens functions are solved by transforming them into a system of linear equations. In contrast to the two other methods only the current and charge distributions at the boundary surface are calculated. For objects with a small volume to surface ratio this method is very efficient in computational resources.

- FDTD:
  In FDTD the time dependent Maxwell equations (differential form) are discretised using central-difference approximations. The resulting equations are solved in a

cycle for the E-field component vectors and the magnetic field component vectors for each discretised volume at a given time. Since it is a time-domain method the advantage is that the full spectral response of an object with a broadband incident pulse (gaussian pulse) can be calculated with a single simulation.

- FEM:
  FEM is also referred to as "Finite element analysis" (FEA). As in the other methods the problem is subdivided into smaller elements. Similar to FDTD this is a volume meshing method and therefore more computationally expensive. Using the parameter variation method the partial differential equations are approximated and solved.

The majority of simulations carried out in the work presented here were done using the BEM method and FDTD simulations, which will be described in more detail in the following paragraphs (section 3.2.1, 3.2.2).

3.2.1 Finite Difference Time Domain Simulations

Most of the simulations were carried out with Rohit Chikkaraddy and part of the following section has been published in[72]. Full-wave finite difference time domain (FDTD) simulations with Lumerical were used to calculate the scattering response and field enhancement of plasmonic cavities formed between faceted 60-100 nm nanoparticles and gold substrates as well as dimers. Gap sizes were varied from 1-10 nm to match the experimental conditions described in section 7.4. For a more accurate representation, the wavelength-dependent refractive index of the gap was extracted from the experimental reflectivity spectrum of the spacer layer (eg. WSe_2 flake), and the parameters incorporated into full-wave calculations to model the NPoM cavity accordingly. The incident plane wave (total-field scattering-field) was set to an illumination angle of Θ_i=55 deg or 0 deg as an approximation for s- and p-polarization respectively. This allows the character of the different plasmonic modes to be tested. To reproduce the experimental condition the collection angles were limited to a cone of Θ_c=0 to 55 deg. (based on the NA of the objective). An inbuilt sweep function was used to scan the incident wavelength from 500 to 900 nm. Different facet sizes were simulated to tune the plasmonic cavity modes across the exciton resonance.
To estimate the mode volume of the cavity resonance, the Purcell factor was calculated,

$$F_P = 3/(4\pi^2)(\lambda_0/n)^3 Q/V. \tag{3.1}$$

As described in section 2.1.3.2 the Purcell factor describes the enhanced spontaneous decay rate of a classical dipole in the NPoM cavity. It is simulated by placing dipoles in specific orientations at the locations where the fields are most strongly enhanced. In the case of the NPoM this is either in the centre of the facet or at the edge near the top nanoparticle (Figure 7.4 e), Figure 7.9). From the simulated Purcell factor and a Q-factor which was inferred from the resonant lineshape of each mode, with $Q = \omega/(\Delta\omega)$, the mode volume was calculated. To simulate strong coupling, the gap of the NPoM cavity is modelled as a self-consistent dispersive medium with excitonic dielectric permittivity described by the Lorentz model as

$$\varepsilon_{tot}(\omega) = \varepsilon_\infty + \sum (f_j \omega_j^2)/(\omega_j^2 - \omega^2 - i\gamma_j \omega)_j, \tag{3.2}$$

where ε_∞= 5 is the non-resonant background, and for each exciton (A,B,C) f_j is the reduced oscillator strength, where $\omega_{A,B}$ = 1.63, 2.0 eV are the A,B exciton energies with linewidth parameters $\gamma_{A,B}$ = 70, 100 meV. The f_j are tuned to match the experimentally observed reflectivity and strong coupling spectra.

To account for the anisotropy of the permittivity, f_j's are adjusted accordingly to give a 50% reduced background refractive index for fields normal to the layer planes as seen in the experimental data.

3.2.2 Boundary Element Method

The implementation of the BEM method was done in Matlab, where the code was developed around the MNPBEM toolbox.The toolbox itself has been designed to provide flexible simulation of the response of plasmonic structures. In principle it works for arbitrary dielectric bodies with homogeneous dielectric properties, separated by abrupt interfaces, and has been proven to work on plasmonic nanoparticles[73]. The algorithm was firstly proposed by Hohenester[73–75], then extended to the layered media case in[76] and adapted with a more efficient multilayer Green's function evaluation, as described in[77]. The toolbox was further improved by Dr. Xuezhi Zheng. He solved the surface integrals of different geometrical structures analytically, which allowed the implementation of Waterman structures[66,78] and other complicated shapes. A centre piece of the BEM method is the calculation of Greens functions suited to the problem. This can usually only be done for linear homogeneous media and therefore places considerable restrictions on the variation of problems that can be solved. In this section, the algorithm underlying

the BEM simulations carried out in this work will be briefly reviewed.
In a multilayer environment, the main equation to be solved is[76]:

$$\begin{pmatrix} A_{11} & A_{12} \\ A_{21} & A_{22} \end{pmatrix} \begin{pmatrix} x_1 \\ x_2 \end{pmatrix} = \begin{pmatrix} B_1 \\ B_2 \end{pmatrix} \tag{3.3}$$

In equation (3.3) A_{11}, A_{12} and A_{21}, A_{22} constitute the matrix A (system matrix) that characterizes the electromagnetic properties of the system under consideration (the nanoparticle on mirror, NPoM). B on the right hand side can either be a single column vector consisting of B_1 and B_2 or in the case of multiple incident fields is multicolumn and represents the excitation of the system. The response of the system is then given by x_1 and x_2 which are unknown. It contains the equivalent charge distribution σ and the current distribution h on the boundary of a nanoparticle shown in Figure 3.6.

BEM simulations were used to calculate the scattering response and surface charge distribution of plasmonic cavities formed by faceted 80 nm nanoparticles and gold substrates. The gap distance was fixed to 0.9 nm to reproduce the spacer thickness used in experiments. Polarization dependent simulations of different facet sizes and with ellipsoidal nanoparticles were carried out to study the effect of asymmetry and cavity angle (chapter 5). Incident angles were adjusted to experimental conditions given by the NA of the objectives. Furthermore extensive simulations varying surrounding refractive index, gap size and nanoparticle size were done to obtain a complete picture of the NPoM geometry (the results are shown in section 4.3).

In order to ensure converging solutions in all cases the grids were chosen sufficiently small. The NPoM geometry is simulated using a four layered system: the Au substrate layer, the CB gap layer, the scatterer (Au ellipsoid) and the surrounding medium (air). The variation of the incident polarization is achieved by rotating the incident angle in p-and s-configurations.

3.3 Sample Preparation

The majority of samples used throughout this work were Nanoparticle on Mirror structures (NPoM). The construct is fabricated using bottom-up self assembly and the process can be divided into 3 steps. The substrate fabrication, the spacer layer deposition and the drop-casting of the nanoparticles solution with desired shapes and sizes. These steps will be described in detail in the following sections.

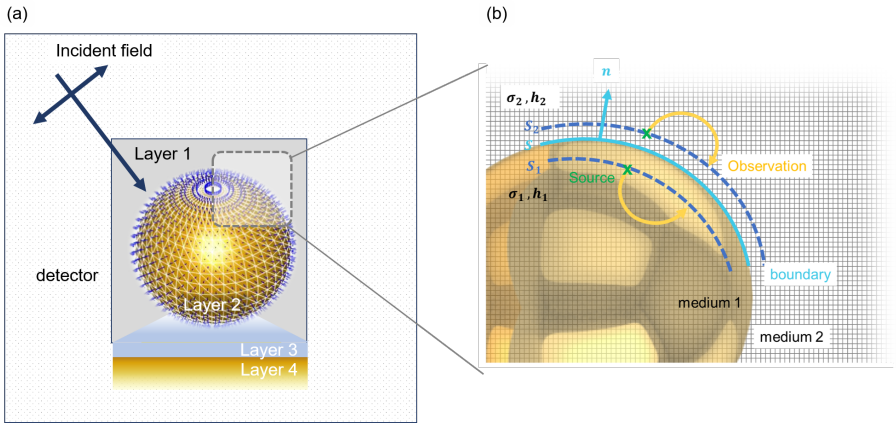

Figure 3.6: **Boundary Element Formalism**(a) Schematic of simulation setup with NPoM system, Illumination source and detector (not scaled) (b) Illustrations of physical quantities involved in the Boundary Element Formalism[75]. The physical boundary of a nanoparticle (S) is marked by the light-blue color with its normal as the blue arrow pointing from medium 1 to medium 2. Boundaries (S1 and S2) just inside and outside the physical boundary are delineated by a dashed dark blue curves. The source and observation points on the inner surface and the outer surfaces are denoted by the dark green crosses ad orange arrows respectively.

3.3.1 Template Stripping of Gold Substrates

In order to guarantee a reproducible optical signature of many NPoM constructs the nanoparticles need to be placed on a atomically flat "mirror" substrate. Using "Template stripping", contamination before depositing the spacer layer can be avoided and the surface roughness is reduced to a minimum. This is achieved by directly depositing the gold layer on a silicon wafer without any adhesive layer.

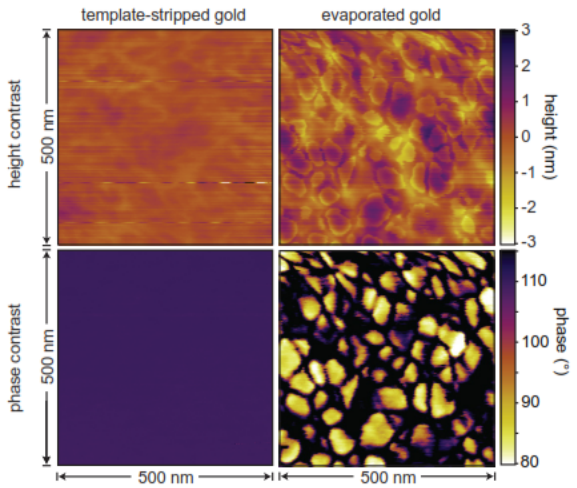

Figure 3.7: **Template stripped gold vs. evaporated gold samples**. AFM images of a 500 nm x 500 nm area of a template stripped gold sample and an evaporated gold sample. Image take from[79]

Evaporation

The process is described in Figure 3.8. Firstly the silicon wafers are cleaned with Decon90 and deionised water. To leave no residue on the wafer, it is rinsed with ethanol, isopropanol and deionised water and then dried with nitrogen. Any residue on the silicon is found to lead to roughness of the gold surface and in the extreme case prevents the gold layer from stripping off the wafer.

The clean wafer is placed in the Kurt J. Lesker Company PVD 200 electron-beam Evaporator and evacuated to a pressure of $10-7$ atms. The crucible of the gold is heated with an e-beam of 10kVs acceleration voltage to create a metal vapour phase. The material is evaporated onto the wafer after opening the shutter. In order to ensure a homogeneous deposition the sample is rotated during the entire process. For the optimal result the deposition speed can be adjusted by changing the e-beam current. A deposition speed of 0.1 $\dot{A}/s$ was found to achieve the smoothest surface.

Template Stripping

After evaporation, the wafer is placed on a hot plate at 60 degrees. A 2 component epoxy glue is mixed by combining the two components 1:1 of Epo-Tek 377. Subsequently, 1 cm^2 squares of flat silicon are epoxy-glued onto the gold surface using approximately $3\mu l$ of epoxy per square. After curing the epoxy at 150 degrees for 2 hours the wafer is slowly cooled down in steps of 10 degrees per hour to avoid thermal stress. Once the wafer has cooled down to room temperature the silicon squares can be striped from the wafer. To reduce the damage of the gold surface at the edges, the outside of the silicon squares are scratched to loosen the squares. The surface used to prepare the sample

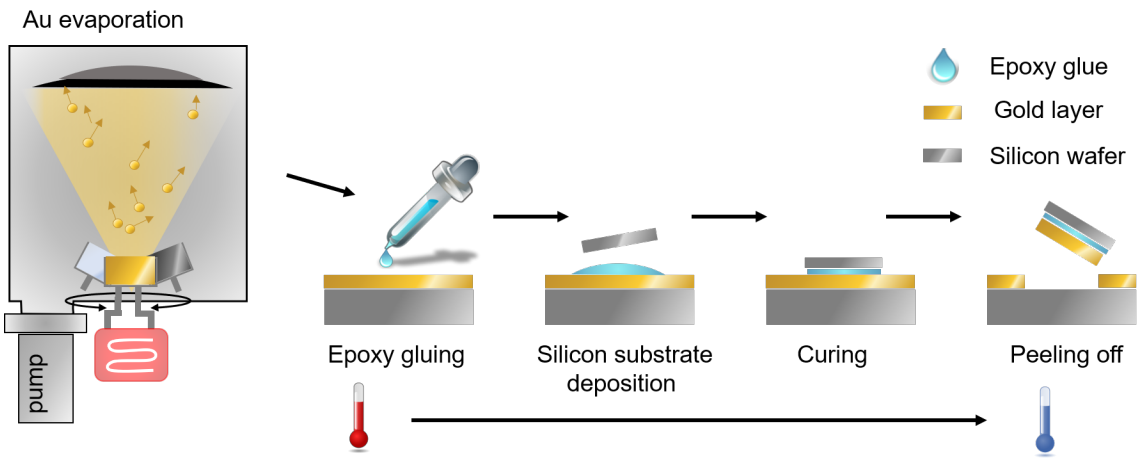

Figure 3.8: **Process of template stripping** 100 nm layer of gold is directly evaporated on a silicon wafer with a titanium adhesion layer in between. By using epoxy and small pieces of silicon wafers it is than "stripped off" the original silicon wafer yielding an atomically flat and clean gold surface.

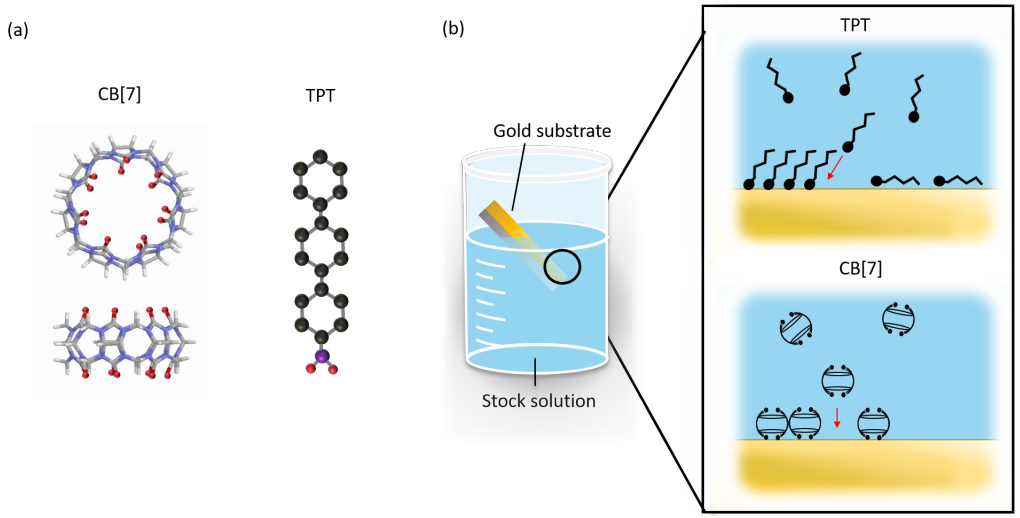

Figure 3.9: **Self-assembled Monolayers** (a) molecular linker molecules used as spacers. (left) macrocyclic molecule cucurbit[*n*]uril (CB[7]) for a 0.9 nm gap, (right) 1,1',4',1''-terphenyl-4-thiol (TPT) for 1.4 nm gaps. (b) Illustration of the formation of self-assembled monolayers with the two different molecular linkers in solution.

is the surface that was in contact with the silicon wafer before. Since it was protected from the atmosphere during the process it is very clean and flat. That way the squares can be stored for several month without contamination before being peeled of.

3.3.2 Self-assembly of Soft Spacer Layers

Self assembled monolayers (SAMs) are dense layers of organic molecules that spontaneously form to an ordered monolayer[80,81]. The molecules used for the SAM are required to have an end group with a high binding affinity to the desired substrate so a uniform monolayer is formed. In the case of gold, thiol terminated groups are a popular choice. Different molecules can be used to achieve a variety of gap distances.

Within this work two types of soft spacers were used: the thiol based molecule 1,1',4',1''-terphenyl-4-thiol (TPT) with a thickness of approximately 1.4 nm[82] and the macrocyclic molecule cucurbit[*n*]uril (CB[7]) for a 0.9 nm gap distances. CB[*n*] molecules are pumpkin shaped molecules with a hydrophobic cavity. It has carbonyl-portals on each end (Figure 3.9) that absorbs to gold surfaces[83,84] Since it is a very rigid molecule it allows for a precise and reproducible gap in plasmonic coupled systems. Furthermore it's pumpkin shape allows incorporation of different molecules in a host-guest configuration[21]. TPT on the other hand is known to have a high degree of uniform packing density as well as good SERS signals. In both cases a 1 mM solution is prepared. Anhydrous ethanol is

chosen as a solvent for TPT and distilled water for CB[7].
The gold substrate is freshly stripped off the wafer and purged with nitrogen to remove any gold flakes. The purged Au substrate is left in stock solution for 10 min (CB[7]) and 24h (TPT) to deposit a monolayer. Afterwards the samples are thoroughly flushed with distilled water or ethanol to remove excess molecules and dried with nitrogen.

3.3.3 2D Materials

Monolayer and few-layer TMD flakes are mechanically exfoliated from bulk crystals onto a silicon substrate coated with a polymer bilayer (100 nm Polymethylglutarimide (PMGI) and 1 μm polymethyl methacrylate (PMMA)). The top PMMA layer is lifted off the substrate by dissolving the sacrificial PMGI layer and transferred onto a gold substrate, fabricated according to section 3.3.1 . The PMMA membrane is dissolved in acetone, and the sample is rinsed in isopropanol and dried with a nitrogen flow.
Additionally, for control measurements 10 nm SiO_2 were deposited onto 100 nm gold substrates by vapour deposition. As with the fabrication of the gold substrate this is done in the Kurt J. Lesker Company PVD 200 electron-beam Evaporator under vacuum and low pressures of $10-7$ atms. After the gold evaporations described above the crucible is switched to the desired material (SiO_2) and heated with an e-beam of 10kVs acceleration voltage. The material is evaporated on top of the gold layer after opening the shutter.

3.3.4 Nanoparticle Assembly

The last step in the sample fabrication is the drop casting of nanoparticles. Depending on the spacer layer the deposition of nanoparticles can last from 10 seconds to 10 hours, reflecting the affinity of the top surface of the spacer layer to the gold nanoparticles. While most of the soft spacer layers have a strong affinity to gold, the hard spacer layers don't interact with the gold except for van-der-Waals-forces, which are very short range. The scattering of nanoparticles decreases with diameter ($\approx D^6$)[68]. Therefore, mostly 60, 80 and 100 nm sized nanoparticles were used for the NPoM constructs tuning the plasmon wavelength to the desired spectral range.

Soft Spacers A drop of BBI gold nanoparticle solution is drop-casted on the sample, and left for 10 seconds (sparse sample, 3.10) or 30 seconds (dense sample). The excess nanoparticle solution along with residue of salt and stabilising agents is thoroughly washed away with distilled water and dried with nitrogen.

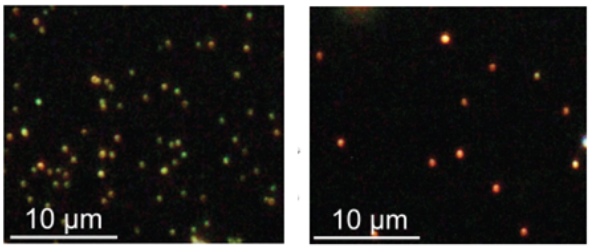

Figure 3.10: **Dark-field images of NPoM samples**(a) high density sample after 30 seconds deposition time. (b) low density sample after 10 seconds deposition time

Hard Spacers The samples were submerged into a small vial of nanoparticle solution and left there for 6 - 10 hours. If the density of nanoparticles on the sample was still too low salt was added to the nanoparticle solution to destabilize the citrate covered nanoparticles in the solution. This destabilization also leads to an increase of nanoparticle aggregates on the sample and therefore was only used for samples with very poor gold interaction.

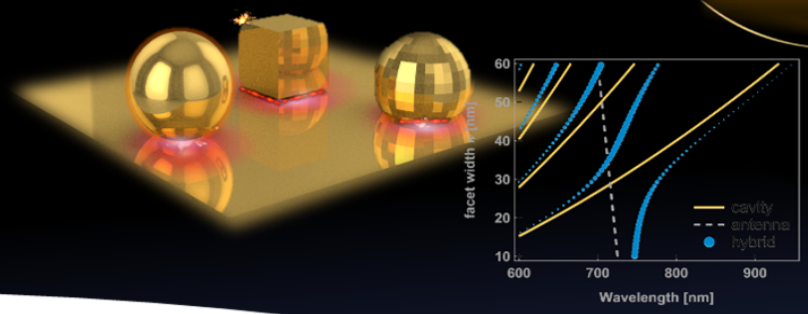

4 Nanoparticle on Mirror

The Nanoparticle on Mirror geometry builds our foundation of cavity plasmonics. This plasmonic nano-cavity enhances light-matter interactions drastically, allowing monitoring down to the single molecule level[21]. Its optical response is highly influenced by the cavity morphology with a sensitivity high enough to track atomistic changes in real time[78,82]. Using plasmonic cavity modes to couple to single emitters and track chemical reactions in real time requires a full understanding of the far-field scattering response and the local field enhancement due to the spatial charge distribution across the nano gap.

In this chapter the cavity that is formed by the nanoparticle on mirror geometry (NPoM) will be addressed in detail. When depicted, the NPoM constructs are mostly shown as perfectly spherical. However as SEM images show, nanoparticles are highly faceted and not always symmetric. The consequence is a complex convolution of dimer like response with the cavity modes, modifying the optical response of the coupled nanoparticle system. To disentangle the different parameters influencing the response of the NPoM system the following relations will be explored:

- The effect of varying nanoparticle size, gap distance and surrounding refractive index on the plasmonic modes of the NPoM construct.
- The impact of the nano-cavity morphology and edge rounding on the far-field scattering response.
- Influence of the symmetry: How gap modes couple to radiative antenna modes.

Combining experimental data with simulations, the different modes (bright and dark) are distinguished and their mixing behaviour, which gives rise to a rich spectrum of plasmonic coupled modes is analysed.

Parts of this work [1] have been published in reference[66].

[1] Experimental work was undertaken in collaboration with R. Chikkaraddy and simulations were carried out together with X. Zheng and R. Chikkaraddy.

4.1 Plasmonic Coupled Systems

The "sweet spots" of plasmonic coupling

As described in section 2.1.2.6 when a nanostructure is placed in close proximity to another nanostructure plasmonic coupling occurs which can be considered within the hybridization model. The coupling not only leads to additional resonances that highly depend on the gap distance as well as the refractive index, but also creates a huge field enhancement (10^4), so called "hot-spots" between the two coupled nanostructures.

This gap-size dependent field enhancement is readily exploited in the literature for

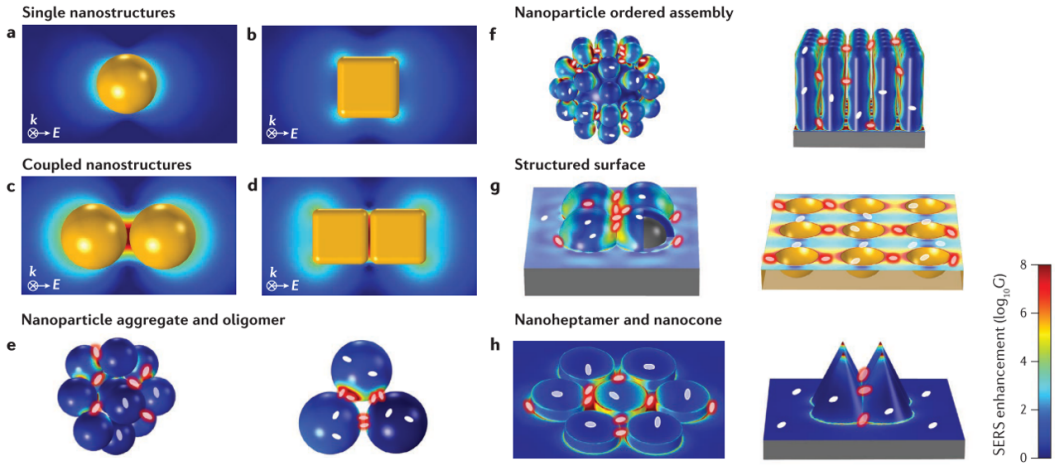

Figure 4.1: Finite-element simulations of hotspots in different plasmonic geometries with an average SERS enhancement $\langle G_{NP} \rangle$ over the entire nanoparticle surface and a maximum SERS enhancement factor G_{NP}^{max} . Exemplary molecules in the hotspot are depicted as red circles and outside the hotpot as white circles. Single nanoparticles show moderate field enhancement: (a) sphere, $\langle G_{NP}(545\ nm) \rangle$=160, G_{NP}^{max}(545 nm)=2500 and (b) cube $\langle G_{NP}(585\ nm) \rangle$=1400, G_{NP}^{max}(585 nm)=2700. Significant increase in enhancement is seen for plasmonic coupled systems (c) nanosphere dimer $\langle G_{NP}(645\ nm) \rangle$=1.47*$10^6$, G_{NP}^{max}=(645 nm)=4.11*10^9 (d) nanocube dimer $\langle G_{NP}(725\ nm) \rangle$=2.41*$10^5$, G_{NP}^{max}=(725 nm)=1.24*10^8.Complex nanostructures formed by (e) nanoparticle aggregates, (f) ordered assembly structures, (e) patterned surfaces and (h) cones dimers and heptamers. Figures and enhancement values taken from: [85]

.

sensing applications such as surface enhanced Raman scattering (SERS), tip enhanced Raman scattering (TERS), plasmon mediated chemistry with very few molecules (such as single molecule redox reactions and catalysis reactions) or for plasmon enhanced strong coupling, going all the way to the single molecule level [10,40,86–88] While there are many different approaches which use plasmonic coupled systems to enhance light matter interactions, the reliable fabrication of such systems bears some challenges and there is still a race on to find the optimal "hot-spot" geometry [85]. Simulations of some representative plasmonic coupled systems with hot-spots and field enhancements are shown in Figure 4.1. Using single nanostructures (Figure 4.1a,b), such as individual spherical nanopar-

ticles, nanorods or cubes, only moderate enhancements at the surface/ edges of the single nanostructure can be reached. This can be further boosted using nanoparticles with sharp edges such as nanostars[89] and nanoflowers[90] by the means of the "'lightning rod effect'. However, these sharp edges round off over time due to degradation or damage with high excitation powers. Significantly greater enhancement is seen for coupled nanoparticles like dimers (bowtie antennas,tip-dimers), trimers[91], nanoclusters[92] (aggregates or ordered chains of nanoparticles[93]) or even structured surfaces and cone-like structures[11] .
The small volumes enclosed between nanoparticles show the largest field enhancement, thus rendering coupled structures the ideal arrangement for high sensitivity sensing[85,94] with nanometric resolution. To guarantee for optimal enhancement and reproducible "hot-spots" the reliable fabrication of theses structures is crucial and will be discussed in the next section.

4.1.1 Fabrication of Plasmonic Coupled Systems

The modes of plasmonic coupled nanostrucutres strongly depend on the inter-particle distance and hotspot geometry, making reproducibility and consistency in the fabrication as well as scalability essential.
Approaches in fabrication can be broadly broken down into one of two categories: bottom-up and top-down (Figure 4.2). While top-down approaches are good for producing structures with long-range dimensions and for making macroscopic connections, bottom-up approaches are best suited for easy assembly and establishing short-range order at nanoscale dimensions (Figure 4.2 c,d,e).

Top-Down

Top-down techniques have been applied for a long time in the semiconductor industry for patterning. Nanostructures are coated either directly using different types of lithography (e-beam lithography) and milling (focused ion beam), or indirectly by producing a template that can be used as a stamp. As the sample is directly patterned a rich variety of complex geometries and shapes can be realised (Figure 4.2 b). Nonetheless, this level of complexity comes at a price. Most of these kinds of fabrication techniques are very expensive, and therefore not transferable to large scale production methods for plasmonics structures. Furthermore, the resolution in the pattern is still limited by the diffraction limit of the ion beam ($\gg$5 nm) and material issues. Therefore, spatial resolution in top-down fabricated structures remains limited to several nanometers[101].

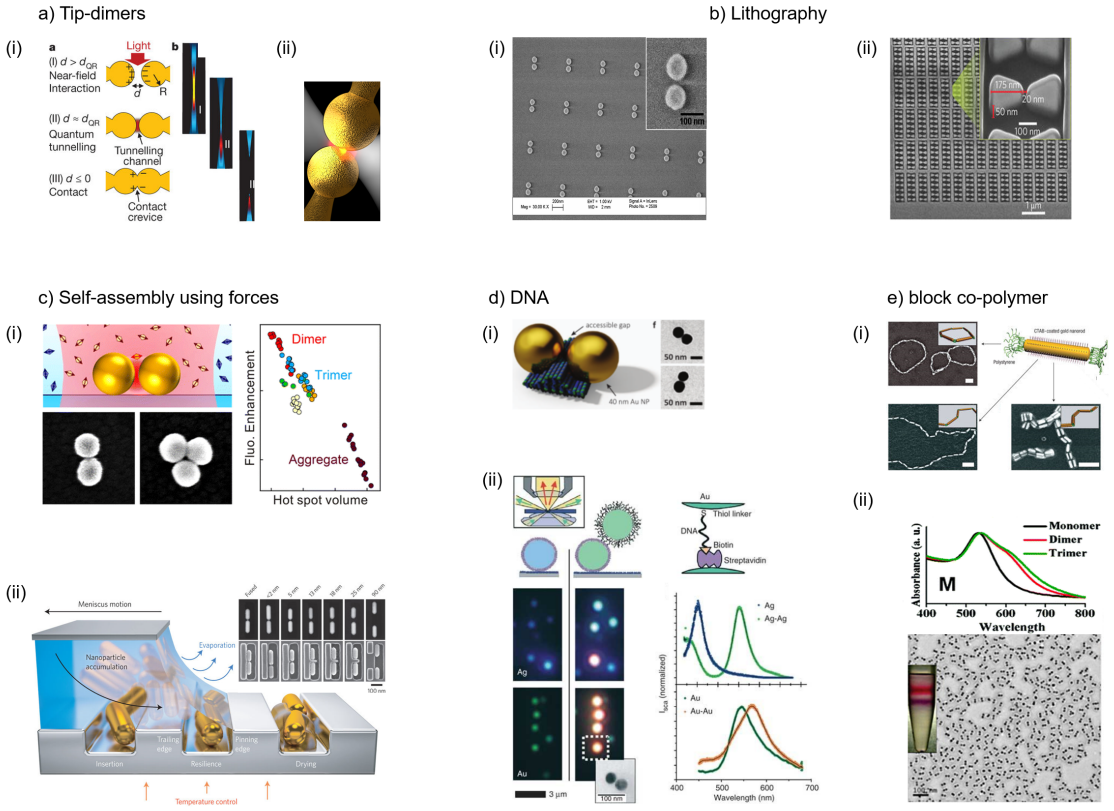

Figure 4.2: Nanoparticle fabrication and assembly processes. (a) Tip dimer formation using to AFM tips reaching sub-nm gap spacings. (b) Complex patterned nanostructures with top-down methods that allow large scale fabrication. (c) Self-assembled nanostructures via aggregation using van-der-Waals forces (i) and de-wetting processes (ii). (d) Controlled self-assembly using molecular linker molecules such as (i) DNA, (ii) thiol linkers or (e) block co-polymers allowing a vary the spacer thickness and to add additional functionalities to the system. Figures taken from [95–100] respectively.

Bottom-up

In contrast bottom-up self-assembly allows for spatial control of less than a nanometer by using molecular linkers to form nanostructures. This direct method of assembly can easily be scaled up to produce large numbers of structures in an affordable way. The individual structures, such as nanoparticles, nanorods or nanoprisms are coated with charged surfactants in solution to stabilize them. Overcoming this repulsion force, for example using salt, brings the particles close together and makes them aggregate due to van-der-Waals forces. This method allows for production of large disordered clusters. While this is a great method to produce large plasmonic coupled structures the reproducibility remains low due to their random aggregation with a large variation in their clustering and packing density as well as their individual spacing.

A more controllable method is the use of molecular spacers. They provide a fixed gap distance between the nanostructures as well as allowing the addition of different func-

tionalities to the structures. Several studies exist on the assembly of nanostructures using DNA in the arrangement of dimers,[102,103] chains,[104,105] or even more complex structures. While DNA assembly previously was limited by the strands length of ∼5 nm to rather large gap distances in recent work the lateral positioning of nanoparticles on DNA rafts with nanometer precision has been shown[40]. A possible alternative to DNA strands is offered by block co-polymers, which have been reported to enable larger scale 2D structures of metallic nanoparticles[106,107]. Scaling down further, another molecular spacer is Cucubit[*n*]uril (CB[*n*]) , which has a relatively rigid structure and stable height of 0.9 nm and therefore allows for a precise control over the gap distance between two adjoining nanostructures[83,84,93,108,109] (also see section).
With increasing complexity of the system more coupled modes start to arise, rendering dimers and simple coupled structures the preferred testing platform. Nonetheless, the fabrication of controlled structures such as dimers and trimers with exact inter-particle distances in high yields is a challenge.

Nanoparticle on Film Structure

A simpler and easily fabricated plasmonic coupled system is the nanoparticle on film system, also called "nanoparticle on mirror" (NPoM, Figure 4.3). The nanoparticles are simply drop-cast onto a gold substrate with a monolayer of a molecular spacer or a 2D material sandwiched in between. Using different spacer layers, either soft or hard, prevents conductive contact and produces consistent gaps with different thickness while allowing any additional functionalisation of the nanostructure due to the electronic properties of the spacer material. The detailed assembly of the NPoM constructs used within this work is described in section 4.1.1. The easy fabrication method allows production of NPoM constructs on a large scale in a time efficient manner. The density of NPoM constructs over a particular area can be controlled by adjusting the deposition time, where densities up to $\sim 10^6$ NPoM per cm^2 can be realized. Here the limiting factor is reducing crosstalk between the individual constructs. The spacing between constructs has to be large enough to guarantee the dark-field scattering collection is from a single structure. In the case of confocal detection the detection area is in the range of $\approx 10\,\mu$m^2 requiring NPoMs to be at least spaced apart further than this.

4.2 NPoM Geometry and its Optical Response

When the nanoparticle is placed on a gold substrate image charges induced in an underlying metal film allow plasmonic coupling between the nanoparticle and its mirror image

(inset in Figure 4.3 b). This creates a system that acts like the coupled plasmonic dimer with an enclosed nano-cavity (inset in Figure 4.3 b). The precision and reproducibility of the NPoM make it the preferential way to fabricate plasmonic dimer systems with equivalent field confinement reaching enhancement factors of 10^4 in the gap (Figure 4.3 a,b).

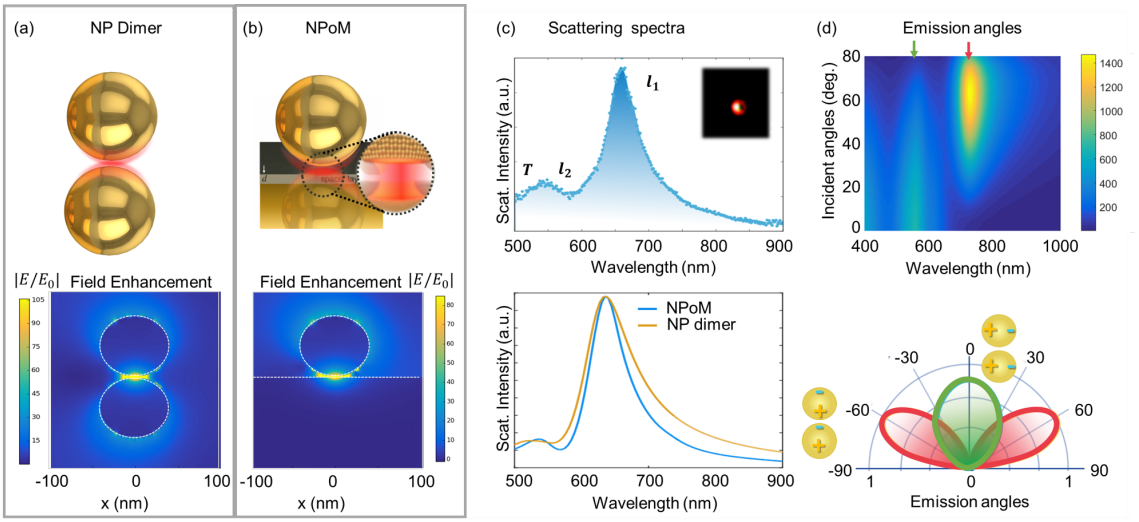

Figure 4.3: **Nanoparticle on Mirror (NPoM)**. The NPoM construct (b) is inherently similar to the plasmonic coupled dimer (a) with equivalent field enhancement in the "hot-spot" reaching factors of $\sim 10^4$ in the gap. (c) Top: experimental scattering response of a 80 nm Au NPoM with a 0.9 nm CB[7] spacer layer, measured using dark-field microscopy. The different modes with the simplified charge distribution are shown in the inset and labeled accordingly: T: Transverse mode, l_2: Quadrupolar mode, l_1: coupled mode. Bottom: comparison of scattering response of a dimer vs. the NPoM construct. Each system is simulated with 80 nm Au nanoparticles and a 1 nm gap.(d) Simulated emission profile of the NPoM system. While the transverse mode is emitted near normal incident the coupled modes are expected to show maximum emission for high angles ($\sim$ 60 deg.).

Perfectly Spherical NPoMs

In a simplified picture the nanoparticle can be considered as perfectly spherical. However, this does not take into account the seed mediated growth of nanoparticles which lead to a variety of different shapes and faceting, which will be discussed in the next section. The scattering spectra of a typical near-spherical 80 nm NPoM with a 0.9 nm spacer layer of CB[7] in the gap (Figure 4.3 c), top) is obtained by dark-field microscopy. Analogous to the plasmonic dimer, the NPoM system has a strong dipolar response, with an equivalent near-field enhancement (Figure 4.3 a,b) and scattering response (Simulations: Figure 4.3 c), bottom). In the simplest case it consists of 3 modes: Transverse mode, Dipolar mode (l_1) and Quadrupolar mode (l_2). Their scattering intensity as a function of emission angle is shown in Figure 4.3 (d). The transverse mode (T) around 530 nm corresponds to the single nanoparticle response and is dominant for polarization perpendicular to the connecting dimer axis (Figure 4.3 d), green). The modes around 600 nm (l_2: quadrupolar

mode) and 730 nm (l_1: dipolar mode) are first and second order coupled antenna modes $l_1, l_2, ...$ (explained in detail later). Due to their dipolar and quadrupolar character they can both couple to the far-field, but it is the dipolar l_1 mode that dominates the scattering spectra. They are most efficiently excited with polarization parallel to the dimer axis or in case of the NPoM system at angles $\Theta \sim 60$ degrees (Figure 4.3 d). This is confirmed by typical dark-field images shown in the inset, where the coupled mode appears as red doughnut shaped rings around green dots corresponding to the transverse mode emitting at near normal incidence. Thus, the high angle emission and excitation of these modes requires high NA objectives to achieve sufficient coupling. As the transverse mode only couples weakly to the induced mirror charge its resonance position is mostly fixed by the nanoparticle size and the surrounding refractive index as shown in Figure 4.4 (a,b). In

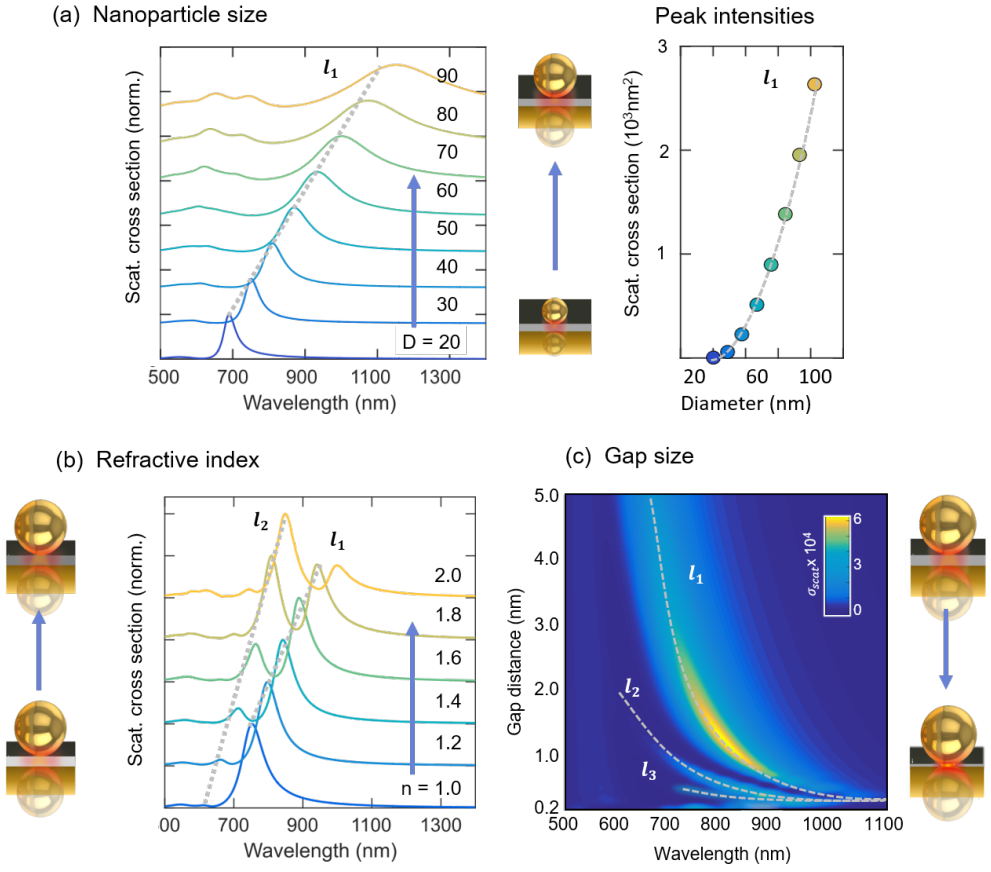

Figure 4.4: **Exploring the tuning parameters of NPoM system using boundary element method simulations (BEM)**. The scattering response of spherical NPoM system at 65 deg. incident angle is simulated. Scattering spectra of the NPoM construct with varying (a) nanoparticle size, refractive index of the spacer layer n and (c) gap distance d as indicated in the schematics on the side. The scattering response as function of n and d was simulated for a spherical 80 nm nanoparticle with a gap distance of 0.9 nm and a refractive index of 1.4 respectively. Extracted peak intensities of the l_1 mode as a function of nanoparticle diameter are shown at the right hand side.

both cases the resonance position of the coupled mode shifts linearly as a function of

refractive index and nanoparticle size, where a refractive index variation of 0.1 already leads to a spectral shift of 25 nm. The surrounding refractive index is left constant but it should be noted that it also has an influence on the mode positions being of importance when using water or oil immersion objectives that require high refractive index matching solutions. A decrease in scattering intensity of the l_1 mode and an increase for the l_2 modes with higher refractive indices is seen in Figure 4.4 (b). The opposite trend is observed for increasing nanoparticle size. Here, the intensity increases as a function of nanoparticle size (Figure 4.4 a, right hand side) accompanied by a broadening of the l_1 mode. Similar trends are seen for the quadrupolar and dipolar mode. However, their mode position is most dramatically affected by changes in the gap distance (Figure 4.4 c). While the resonance position of the transverse mode remains nearly constant as a function of gap size, the quadrupolar and dipolar modes show clear spectral shifts[82,110] (Figure 4.4 c), where three regimes can be identified. For a nanoparticle with a very thick spacer layer the nanoparticle acts independently as no coupling to the underlaying mirror occurs. For a spacer thickness much smaller than the nanoparticle size the coupling becomes significant and higher-order antenna modes l_2, l_3.. are effectively excited. The coupled modes initially red-shift as a function of decreasing separation and the far-field response is weakened as the effective dipole of the dimer-like structure is reduced[111]. As the spacer thickness is further decreased, there is a strong build up of charges at the opposing faces in the gap accompanied by a near-field enhancement. The third regime is the "nearly-touching" regime, for gap distances $d \leq 1$ nm. Here, local effects, such as dynamic screening and charge spill out[19,112] start to play an important role and dramatic changes in the scattering response occur in form of additional modes disappearing rapidly into the infra red region[111]. With decreasing distance the dominant dipolar modes become narrower and decrease in intensity as the higher order modes take up some of the overall light scattering strength. At the same time each of the higher order modes first increases in strength as d decreases, and then eventually decreases for even smaller d, while shifting to the red. This occurs sequentially for each successive shorter wavelength mode. The narrowing of the modes in the infra red region is likely caused by the lower absorption of the gold at longer wavelengths. These results demonstrate the exquisite sensitivity of the optical response of the NPoM system to the nanoparticle size, its surrounding refractive index and gap distance. Here, the smaller the gap the larger the field enhancement in the gap region and the higher the sensitivity. However, for very narrow gaps ($d \leq 1$ nm) the morphology of the cavity itself starts to impact the optical response. Therefore, to describe the full picture the faceted nature of nanoparticles has to be accounted for, which will be discussed in detail in the next section.

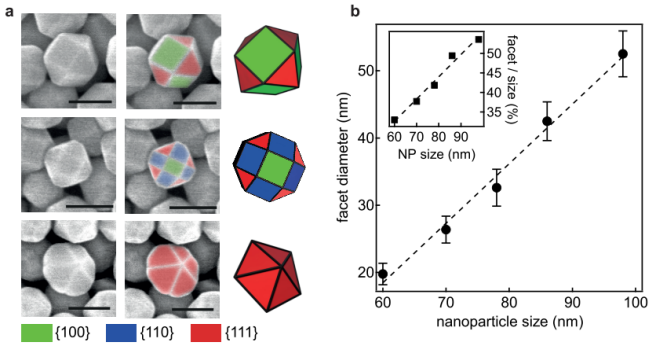

Figure 4.5: **Faceted nanoparticles**(a) SEM images of commercially bought spherical BBI nanoparticles showing a large variety of faceting with corresponding 70 nm scale bars. The different crystal faces are color coded respectively and the deducted Waterman structures are shown to the left from top to the bottom: cuboctahedron, rhombicuboctahedron and pentagonal bipyramid. (b) Correlation of nanoparticle size with facet ratio. Figures taken from [82]

4.3 Nanoparticle Size and Faceting

While most schematics of the nanoparticle on mirror geometry show perfectly spherical nanoparticles on top of a flat mirror, in reality gold nanoparticles are highly faceted and asymmetric (Figure 4.5 a). This is due to their crystalline nature, where the different crystal faces grow at a variety of speeds due to their differing surface energy [113]. For a single crystal seed, free of 2D defects, the dominant growth shapes are variations of octahedra; for twinned seeds already more complex shapes such as pentagonal bipyramids or icosahedra are grown. This has been exploited in literature to grow diverse structures such as triangles, pentagonal bipyramids, octahedra or truncated octahedrons [114]. Even for nominally spherical nanoparticles commercially bought from BBI, SEM images (Figure 4.5) reveal the large variety of shapes and sizes of the nanoparticles within a single batch. Despite the relatively mono-disperse size distribution with less than 5 % variation, the variation in the facet size and shape is large. The trend between nanoparticle size and facet size goes linearly as seen in Figure 4.5. Despite the linear trend, looking at the gradient it is evident that bigger nanoparticles show a higher ratio of facet size to nanoparticle volume. For individual nanoparticles the optical response is hardly affected by the facet size variations. However, this is not the case for coupled nanoparticles.

Gap Modes

Faceting of the nanoparticles changes the gap morphology drastically, affecting the near field and therefore inherently the far field. Additionally to the coupled antenna modes another set of modes, so called "gap modes" arise due to the formation of a cavity between the facet and the underlying mirror with specific boundary conditions (Figure 4.3). The influence of these modes on the scattering response of the NPoM system is

highest for very narrow spaced nanoparticles and can be understood within the metal-insulator-metal (MIM) waveguide picture[115].

As the name suggests, gap modes show strong field enhancement, highly localized in the gap region which quickly drops off away from this area. In contrast to the antenna modes they are non-radiative. The resonance condition of the gap modes is given by the lateral boundary conditions of the facet width. In a simplified model for spherical nanoparticles, these modes can be described as drum-like standing waves, and calculated analytically using Bessel-functions to give[116]:

$$\lambda_i(w,d) = \lambda_p \sqrt{(w\varepsilon_d/(d\xi_i) + \varepsilon_\infty)}, \tag{4.1}$$

where λ_p is the plasmon wavelength of Au ($\propto$148 nm), ε_∞ is the background permittivity, ε_d is the permittivity of the gap spacer, w is the facet width, d the gap size, and $\xi_i = \xi_i + \phi$ is the i-th antinode of the $J_0(\xi)$ cylindrical Bessel function, with $\phi = \pi$ the phase-shift caused by the reflection of the cavity modes at the edge of the cavity. Just like standing waves the number of nodal points increases with increasing order of the mode. These transverse modes depend on the lateral facet width w and show different symmetries depicted in Figure 4.6 (a). Two types of mode symmetries can be identified from the charge distribution in the gap: even-order and odd-order modes. The even-order modes are centro-symmetric and and have a maximum field distribution in the middle of the facet. The odd-order modes have a nodal-point in the centre with a higher field distributions on the edge of the facet. The indices in $(s_{01}, s_{11}, ..)$ therefore mark the number of nodal points in the x and y direction and indicate the symmetry of the charge distribution in the gap.

Hybridization of Gap and Antenna Modes

While these gap modes are tightly confined in the plasmonic cavity and are therefore optically dark, they can couple to antenna modes $(l_1, l_2, ..)$ which have a vertical dipole (Figure 4.6 a), top) and a charge distribution across the entire nanoparticle[115–118]. The resulting hybridized modes ($j_1, j_2, ...$, turquoise dotted line Figure 4.6 b) form at the crossing points of the gap modes (orange) and the antenna mode (grey dashed line) for different facet width w. The radiative strength of the new hybridized modes j_i as a function of wavelength and facet width w is extracted by carrying out an eigenmode analysis and depicted as dot size in Figure 4.6 (b). Hybrid modes show highest radiative efficiency when in close proximity to the antenna modes. When close to the l_i modes the antenna mode fraction is highest, whereas moving further away their character becomes more cavity-like. Furthermore, the radiative efficiency and the in- and out-coupling of these modes depends on the overlap of the mode pattern of both modes (l, s)[66,115]. While clear anti-crossings are seen for even-order modes, which have the highest intensity

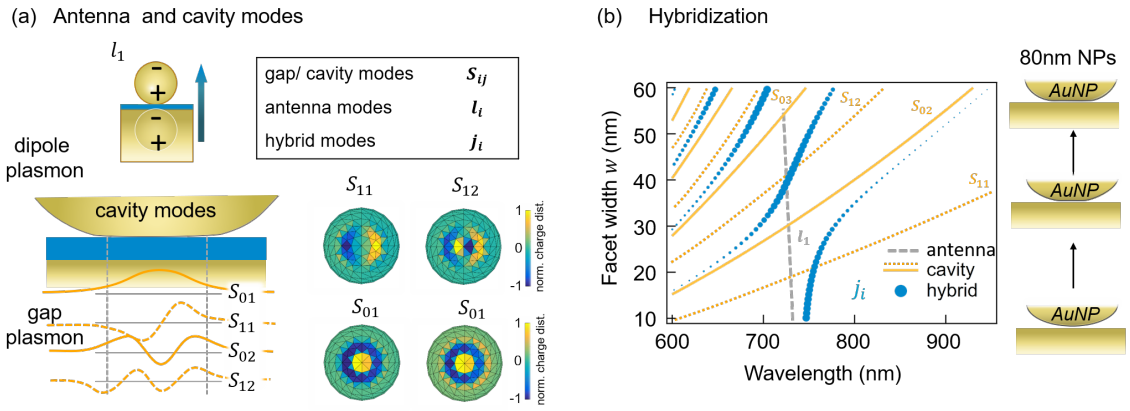

Figure 4.6: **Hybridization model of gap s_{ij} and antenna modes l_i** (a) The nomenclature of the different plasmonic modes is summarized in the top table. Schematic of the dipolar character of longitudinal antenna mode l_1 (top), which are bright and couple efficiently to the far field (blue arrow shows dipole orientation). In contrast, gap modes (bottom) are tightly confined in the cavity with field distributions showing even and odd order symmetries. The corresponding charge distribution of the different cavity modes s_{ij} is shown at the right hand side. (b) Hybridization of cavity and antenna modes with increasing facet size w. Analytical model is calculated for a 80 nm nanoparticle with a 0.9 nm gap size. Strong mixing of the l_1-modes (gray dashed line) with the even s_{0i} modes (solid orange line) is seen for larger facet sizes. Where no mixing occurs for odd order modes s_{jj} (dashed orange lines) indicated by a crossing rather an anti-crossing of the hybridized modes (turquoise dots, j_i). Hybridization model is adapted from [116].

in the centre of the facet, odd order modes with nodal points at the centre of the facet remain unaffected, merely crossing the antenna modes. Thus, even-order modes i are found to be bright, while odd-order modes $i+1$ remain dark. While the analytical model creates a good intuition of the plasmonic cavity, boundary element simulations (BEM) are needed to describe the full picture and predict the exact mode positions of the NPoM construct. The influence of the nanoparticle faceting on the optical response becomes more evident when simulating the different sets of modes with increasing facet width w. For simplicity this is simulated by cropping off the bottom of a spherical 100 nm nanoparticle, where the facet width is varied from 5 nm to 60 nm (Figure 4.7). To mimic experimental data a spacer thickness of 0.9 nm is chosen with a refractive index of 1.4. Here, the spacer layer is set to be large enough so that classical electrodynamics provides an accurate description of the optical response. The scattering map (Figure 4.7 a) shows a complicated picture containing many modes, all highly dependent on the facet width. By gradually increasing the width of the facet, a set of transverse cavity modes is progressively excited and hybridizes with the antenna modes (orange dotted lines indicate the different set of modes). The individual scattering spectra for increasing facet width (w =5 to 80 nm in steps of 5 nm, as illustrated in the b) are shown in (Figure 4.7 c). For clarity the subsequent spectra are shifted vertically and normalized. Comparisons between BEM simulations and the analytical model (Figure 4.7 a) blue dashed lines)

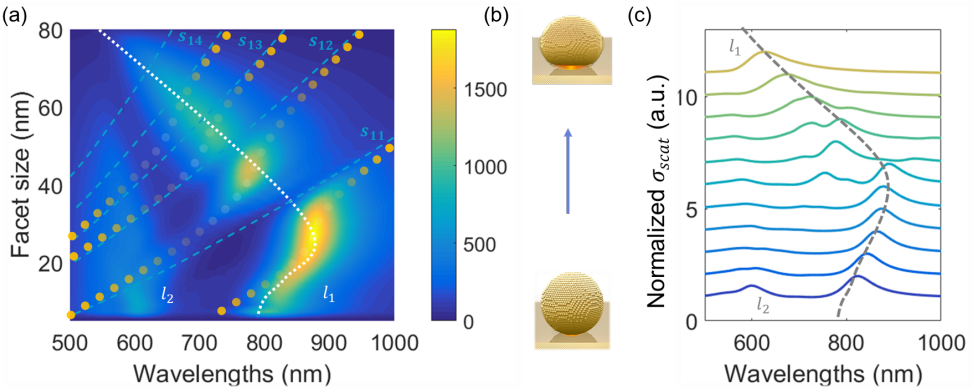

Figure 4.7: **BEM simulations of faceted NPoM** (a) Simulated scattering spectra for a faceted spherical gold NP with diameter D = 100 nm, separated from a 1 μm thick gold film by a dielectric spacer layer (thickness d = 0.9 nm and n=1.4) as indicated by the schematic in (b). Changing the facet width w is simulated by cropping the bottom of the nanoparticle while keeping the volume of the nanoparticle constant. This leads to an increasing circular facet diameter w from bottom (w = 0 nm) to top (w= 50 nm). A white dashed line is overlayed indicating the resonance position of the l_1 antenna mode and blue dashed lines indicate the gap modes s_{ij}. Yellow circles mark all excited modes to guide the eye. (c) Extracted consecutive scattering spectra with increasing circular facet diameter w=5 to 80 in steps of 5, with the two antenna modes l_1, l_2 indicated in grey. For clarity curves are shifted vertically and normalized to 1.

show that the main trends are well reproduced by using the simplified analytical model. The dispersive character of the antenna mode l_1 is extracted from the simulated BEM data and not included in the simplified analytical model (Figure 4.6 b). In the spectral region where the antenna and gap modes overlap, the BEM simulations confirm the anti-crossing behavior for even-order modes and the crossing behavior without interactions for odd-order modes. This is also reflected in the intensity profiles. The scattering intensity and therefore the coupling to the far-field increases in the area where the gap modes overlap with the antenna modes whereas the intensity drops off in regions far away from the antenna mode. Here the out coupling behavior and therefore irradiation angles of the hybridized modes are dominated by the antenna modes. Furthermore, it can be seen that an increase in facet size initially leads to an overall red-shift of the modes for facets from w ~0-15 nm. At larger facets the red shifts saturate and the modes eventually start to blue-shift for very large facets, due to the height reduction caused by cropping the nanoparticle. The spectral position of the mixed modes therefore is determined by the ratio of the facet width to the nanoparticle size and the symmetry, where only the even-order gap modes contribute to the far-field scattering. The symmetry in turn is influenced by the nanoparticle shape as well as the faceting itself, which will be discussed in the next section.

Edge Rounding and Contact Angle

For both the analytical model and BEM simulations described so far, the faceted nanopar-

ticle has been assumed as a perfectly spherical nanoparticle with the bottom cropped off. This is not fully representative of these plasmonic cavities as the facet angle formed between the nanoparticle edge and the cavity has been reported to highly influence the field enhancement and scattering response of the cavity (Figure 4.8 a)[115,119]. Tserkezis et al.[115] calculates the mode-mixing by a hybridization model which describes the interaction of the two modes as Coulomb coupling between the charge distributions in the gap. Their simulations indicate that lower angles between the sidewall and the facet bottom face are favored for larger mixing and efficient coupling to the far-field. This is in agreement with simulations carried out with R.Chikkaraddy. Gradually transforming a nanocube into a nanoparticle via an increase in edge rounding gives a linear blue shift of the cavity modes s_{11}, s_{02} (Figure 4.8 b). Furthermore, for large gaps the s_{11} mode of the cube reaches Purcell factors up to 7x 10^3, while for smaller gaps $d < 4$ nm the NPoM construct shows a larger ratio of field enhancement to mode volume making it more suitable for coupling to emitters[66]. This clearly shows that further simulations are needed, including edge rounding effects and facet angles to accurately describe the full optical response of plasmonic cavities.

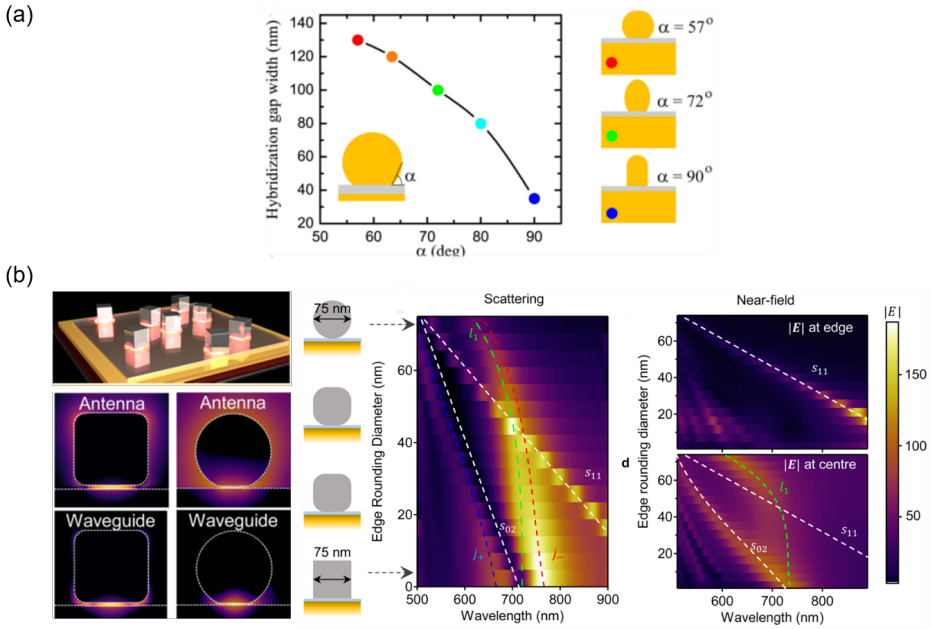

Figure 4.8: **Influence of edge rounding** (a) Interaction between l_1 and s_i modes, expressed in terms of the width of the produced hybridization gap, as a function of the angle α between the nanoparticle sidewall and the facet bottom face (see inset). Colored dots for the different angles map directly to the corresponding right-hand schematics. (b) Simulations of gradual transformation from cube to faceted sphere showing the change of plasmonic modes and corresponging field enhancement. Figures taken from[66] and[115] respectively.

4.4 Conclusion

The nano-cavity formed in a plasmonic coupled system acts as versatile sensing platform with many applications. These range from enhanced sensing and spectroscopy for chemical identification and detection, bio-sensing, near-field optics and scanning microscopy using metallic probe tips, to signal propagation with metal-based waveguides[10,40,86,87,101]. All of these applications depend exquisitely on the the exact morphology and reproducibility of the hot-spot. Therefore, reliable fabrication and an underlying understanding of the optical response of the system are essential to design the cavity and tailor the hot-spot. In this chapter different fabrication strategies were reviewed and the optical response of the NPoM was discussed. In the simplest case nanoparticles are considered perfectly spherical and the optical response is composed of coupled and single nanoparticle modes. Taking faceting effects into account additional "gap modes" arise. These modes are highly confined in the cavity below the nanoparticle and mix with the antenna modes to form a new set of hybridized modes. Carrying out boundary element simulations (BEM) simulations, the parameter space was mapped out and the crucial influences dominating the coupling behaviour were identified. An analytical model was introduced to create an intuitive picture and representing the key parameters. For larger gaps ($>$1 nm) the field enhancement in the gap is found to drop off quickly and the mode positions are set by the nanoparticle size and the refractive index. For smaller gaps ($<$1 nm) the optical response is dominated by the gap modes. Due to the high field confinement of these gap modes they are highly dependent on the facet morphology forming a cavity with ultra small mode volumes ($\geq$ 1 nm^3)[120] and field enhancement up to 10^4.

5 Polarization

Coupled plasmonic structures are of great interest in the sensing community due to their enhanced optical fields in the cavity hot spot. The high tunability and the extreme light localization make them attractive candidates for applications in Surface enhanced Raman Scattering (SERS), Coherent Anti-stokes Raman Scattering (CARS), active optoelectronics, nanochemistry and nanoscale sensing. As discussed in the previous chapter the field enhancement stems from a set of modes that are highly dependent on the morphology and structure of the nanoparticle on mirror construct. In the extreme case of very small gaps ($d \leq 1$ nm), faceting dominates the optical response. Therefore characterizing and controlling the nanoparticle facet is essential. However, the cavity morphology of the NPoM construct remains hidden underneath the nanoparticle, inaccessible for conventional characterization techniques such as Scanning Electron Microscopy (SEM) or Transmission Electron Microscopy (TEM).

In this chapter non-invasive polarization-dependent dark-field spectroscopy is used to map out the influence of nanoparticle faceting and asymmetries with nanometer resolution, thus accessing the concealed plasmonic cavity. Employing incident light polarized in the azimuthal plane (xy plane parallel to the substrate) excites tightly-confined dark cavity modes that are highly sensitive to the exact morphology of the cavity. Together with boundary element method (BEM) simulations, the origin of these modes is revealed, exposing the precise geometry and orientation of the facet, which otherwise is hidden underneath the nanoparticle. Comparison to an analytical cavity model creates an intuitive picture, advancing the understanding of how atomistic changes in the gap morphology affect the optical response of plasmonic coupled systems with sub-nm separation. [1]

[1] Simulations were carried out together with X. Zheng. Parts of this chapter have been previously published in reference [78].

5.1 Polarization Signatures of Narrow Gap Systems

By studying plasmonic narrow gap systems with dark-field microscopy, plasmonic modes arising in coupled nanoparticle systems can be directly monitored. These systems include nanoparticle on surface systems[117,121] or Ag and Au nanoparticle assembly of dimers and trimers[101] and even more complex structures[10,122].

The wide interest in plasmon coupled structures is well reflected in the plethora of work that has been carried out studying the influencing parameters of plasmonic coupled systems (Figure 5.1). While the initial work was focussed on the influence of nanoparti-

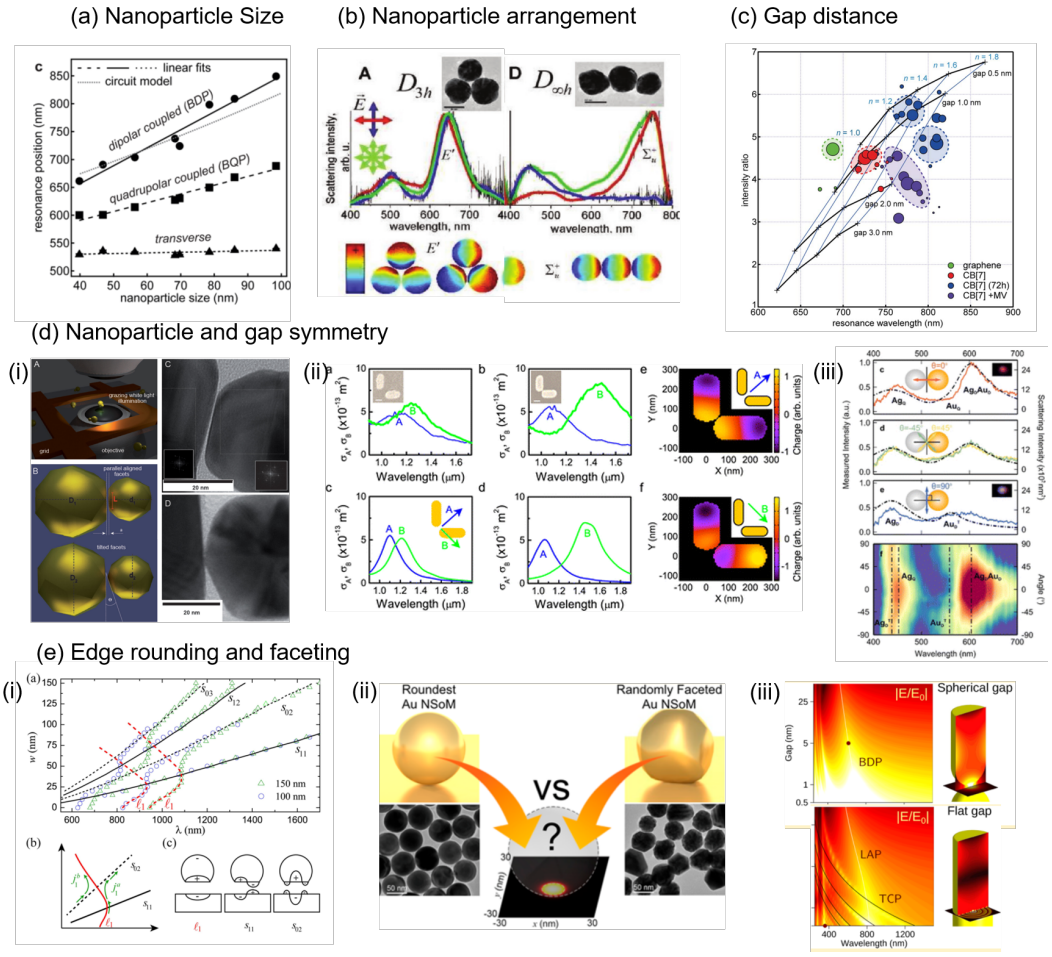

Figure 5.1: **Plasmonic narrow gap system**. Dark-field scattering reveals large influence of (a) nanoparticle size, (b) nanoparticle alignment and (c) gap separation on the optical response of plasmonic narrow gap systems. (d) Polarization dependent dark-field scattering reveals further information about the symmetry of the arrangement as well as the gap itself. (e) Edge rounding and faceting is shown to have large effects on plasmonic mode hybridization and field enhancement in the gap. Figures taken from[82,110,115,119,123–125]

cle size[82,117,126,127], substrates[128], spacer materials and gap size[110,129,130] (Figure 5.1 a,b,c), it became evident shortly after that the nanoparticle shapes[131] and especially nanoparticle faceting largely impact the optical response (Figure 5.1 e). Further refining

advances followed analyzing the effect of edge rounding, particularly facing the enclosed gap (Figure 5.1 e),[66,115,116,119,132–135] and symmetry as well as the topology of larger clusters[91,121,122,136–142] (Figure 5.1 d). These experimental findings were accompanied with corresponding extensive theory work[15,115,125,143].

Despite wide interest in this field and significant theoretical progress, mapping the exact morphology of plasmonic cavities remains a challenge - the NPoM cavity is inaccessible beneath the nanoparticle on top of it. Moreover, commonly used imaging methods such as SEM and TEM that rely on accelerated electrons to image structures, damage these constructs and change their optical signatures, thus making the analysis complicated and unreproducible[123]. Polarization-dependent broadband dark-field spectroscopy instead is a low cost, non-invasive characterization technique that allows the influence of nanoparticle faceting and asymmetries to be mapped out with nanometer resolution. The following work was carried out on the custom built polarization dark-field microscope described in section 3.1.1. High-angle (Θ =55-65 deg.) annular excitation produces scattered light from individual NPoMs and is collected in a cone from Θ= 0-55 degrees. The background-free dark-field scattering is extracted by blocking the incident light with an aperture and spectrally analysed in confocal detection. The incident light is linearly polarized and set by a broadband grid polarizer. Using an ultra-broadband half-wave plate in the excitation beam path (Figure 5.33.3) the linear polarization is then rotated by ϕ perpendicular to the beam propagation axis. The linearly polarized light maintains its polarization even after the high-NA objective[144], resulting in s and p-polarized light (orange, blue inset, Figure 5.3 a). When carefully aligned, the mixed p-polarized components coming from two opposite sides of the incident annular cone cancel out due to the out-of-phase superposition of these beams (Figure 5.3 a), blue). The remaining constructively-superposing components are s-polarized light in the azimuthal plane (x-y plane, for more details see below).

While in former studies unpolarized or p-polarized light was used[92,118,126,129] to study the influence of the nanoparticle size and gap spacing[82,110], the following chapter demonstrates how s-polarized dark-field scattering can be used to directly access the cavity modes in the NPoM geometry. In combination with BEM simulations, s-polarized dark-field spectroscopy can be used to identify the characteristic modes of plasmonic structures, where a splitting in the polarization directly relates to the asymmetry of the system. This is exploited to distinguish and map out the orientation and asymmetry of different plasmonic constructs.

Identifying Different Nanostructures by their Polarization Signature

The typical experimental scattering response of different plasmonic structures as a function of polarization is shown in Figure 5.2, starting from simple (on the left) to more

complicated (to the right). Schematics of the compared structures are shown in the inset: (a) a single nanoparticle on glass, (b) a nanoparticle dimer on glass, (c) a spherical nanoparticle and (d) a non-spherical nanoparticle on Au with CB[7] as a molecular spacer layer.

The first row shows the individual normalized scattering spectra with colours represent-

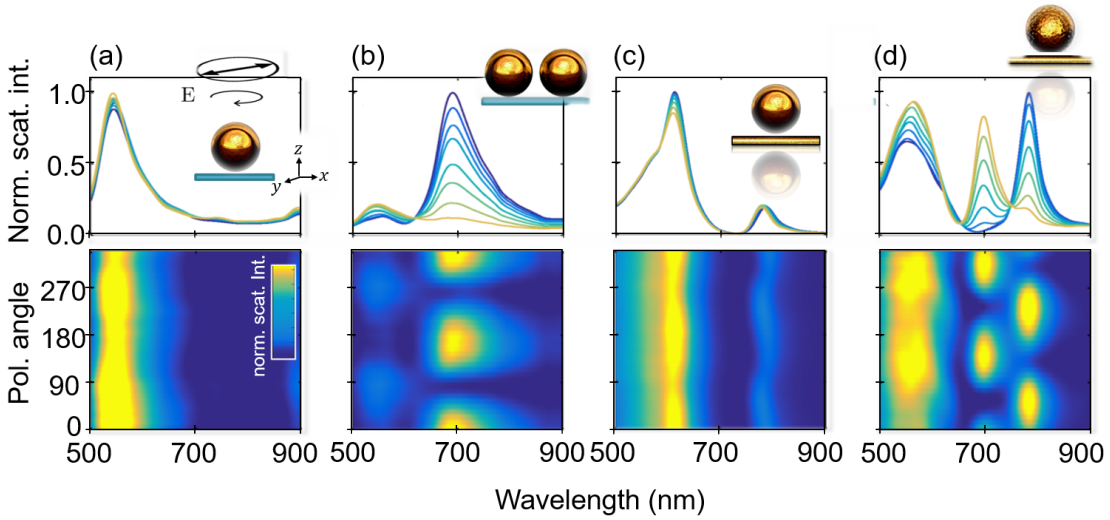

Figure 5.2: **Experimental dark-field scattering from plasmonic structures as a function of linear incident polarization** The first row shows the individual scattering spectra of structures shown in the inset sketches, while second the row shows the corresponding polarization maps. No polarization signatures are seen for the symmetrical structures in the x-y plane: (a) 80 nm Au NP on glass, (c) spherical 80 nm Au NP on Au substrate with 0.9 nm CB spacer. By contrast, very different polarization effects are found for asymmetric plasmonic constructs: (b) 80 nm Au NP dimer coated with chitin on glass substrate, and (d) faceted 80 nm Au NP on Au substrate with a 0.9 nm CB spacer layer.

ing the different polarization angles realised by rotating the linear polarizer. To visualize the variation in peak intensities, the second row shows a polarization map, with the colormap corresponding to the scattering intensity of the same structures shown in the first row.

Starting at the left with a single spherical NP on glass, only a single mode around 545 nm appears. This transverse mode has no polarization dependence in the case of a spherical nanoparticle. In contrast, a NP dimer that has the dimer axis in the azimuthal plane (x-y-plane) shows a strong polarization dependence for both modes[91,121,141]. The transverse mode at 545 nm dominates the spectrum for polarization angles perpendicular to the dimer axis, showing the same spectra as for the single nanoparticle on glass (Figure 5.2 a). The coupled mode (695 nm) reaches its maximum for polarization angles when the E-field vector oscillates parallel to the connecting axis. Rotating the incident polarization within the sample plane thus maps out the orientation of the dimer, identifying the two main axes of the plasmonic structure.

Placing a single nanoparticle on top of a flat gold mirror results in the typical NPoM

structure (Figure 5.2 c). Apart from the transverse mode there is evidence of two additional modes at 600 nm (quadrupolar mode) and 780 nm $s_{x,y}$ (first order cavity mode). Here, the effective dimer axis is rotated by 90 degrees so that it extends in the direction perpendicular to the sample plane (z) in contrast to the nanoparticle dimer which is oriented parallel to the sample plane (x,y). Therefore, in the s-polarized configuration the excitation efficiency of the coupled mode is very low. Instead, the mode at higher wavelength corresponds to a gap mode, which will become more evident for non-spherical particles. For a perfectly spherical nanoparticle the optical response is the same for all polarization angles due to the symmetry in the azimuthal plane. For imperfectly spherical nanoparticles (Figure 5.2 d) the cavity modes $s_{x,y}$ (700 nm and 790 nm) split according to the two fundamental axes of the cavity, revealing the orientation and asymmetry of the facet hidden underneath the nanoparticle. This signature is only seen for s-polarized dark-field scattering and will be discussed in detail in the next section.

5.2 Polarization Signature of the NPoM System

More insight into the polarization dependent behavior is gained by anlyzing in detail the different modes. In Figure 5.3 a) the two possible polarization configurations are shown. Conventional high NA dark-field spectroscopy on NPoMs with unpolarized white light contains $p-$ and $s-$ components. When focussed on to the sample the s-polarized

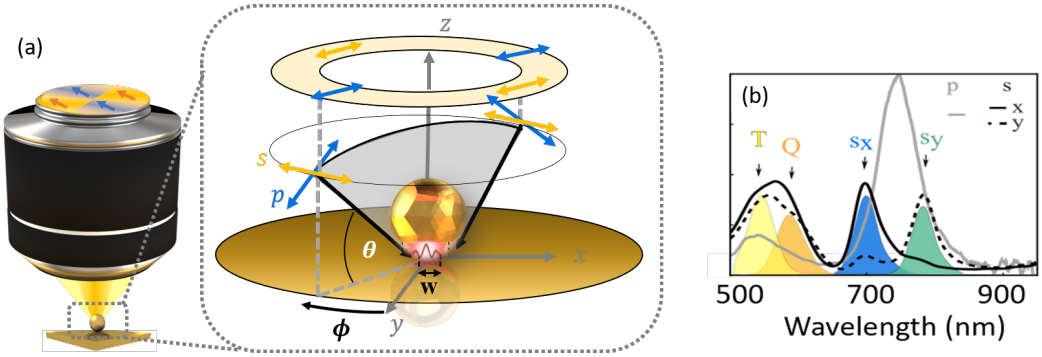

Figure 5.3: **Polarization-dependent dark-field scattering of a 80 nm faceted Au nanoparticle atop a 0.9 nm molecular spacer layer of CB[7] on a Au mirror (NPoM)**. (a) Schematic of experimental setup with incident light within a cone at high angles. Red line in inset depicts gap plasmon mode amplitude. Right side shows how coherent light when linear polarized transforms into the two different polarizations in the focal plane. (b) Experimental scattering spectra of p-polarized (gray) compared to s-polarized (black) incident light. Orthogonal polarization axes (x,y) within the azimuthal plane (solid, dashed) show different modes. T: transverse, Q: quadrupolar, $s_{x,y}$: dark cavity modes.

light remains its E-field components oscillating in the x,y plane (Figure 5.3 a), orange).

However, depending on the NA of the objective the E-field of the p-polarized light oscillates along z parallel to the NPoM axis (Figure 5.3 a), blue) and probes the vertical antenna mode (grey line in Figure 5.3 b). This mode couples more efficiently to the far field, resulting in larger scattering intensities that dominate the optical response for unpolarized incident light.
Using a linear polarized laser in the excitation, the polarization is set by rotating a half-wave plate (5.3 a, ϕ). In the case of an annular excitation cone (yellow ring in Figure 5.3 a), the polarization components of each side of the cone interfere in the focal plane. The p-polarized components coming from two opposite sides of the incident annular cone cancel out due to the out-of-phase superposition of these beams (For more details see section 3.1.1.1). The remaining constructively-superimposing components are s-polarized in the x,y plane (Figure 5.3 a). The direction of the oscillating E-field is set by the direction of the incident polarization (ϕ). Rotating the half-wave plate therefore allows to rotate the polarization within the plane of the NPoM cavity. The scattering response of s-polarized incident light as a function of wavelength is shown in Figure 5.3 b). There are three different modes besides the single nanoparticle transverse (T) mode at 550 nm. The T mode remains constant for all polarization angles as expected and therefore contains no information about the cavity morphology. The mode around 607 nm can be identified as a quadrupolar mode (Q), which was discussed in section 4.2. Most significant are the two longer wavelength modes labelled $s_{x,y}$ at 787 nm and 827 nm, which show a clear polarization dependence. A distinctively different scattering response is found for the two perpendicular polarization axis along x and y (Figure 5.3 b), black solid and dashed line respectively). In contrast, the p-modes show negligible polarization dependence (Figure 5.3 b) due to their z-oriented dipole, which gives a centro-symmetric charge distribution within the gap that is independent of the facet asymmetry. As the p-modes radiate more efficiently to the far-field and spectrally coincide with the s-modes this polarization signature is usually hidden underneath the coupled modes. The radiative character of the modes is also reflected in a larger FWHM of the coupled modes compared to the cavity modes (s-modes).

5.2.1 Comparison of BEM Simulations and Experimental Data

The full measured and simulated optical response as a function of polarization angle using s and p-polarized incident light is shown in Figure 5.4. The s-polarization response is phase-shifted by 90 degrees between the two s-modes and follows a sinusoidal intensity pattern. This polarization signature depends on the deviation from a perfectly spherical nanoparticle (SEM image right side Figure 5.4 a, top facet marked with white dashed

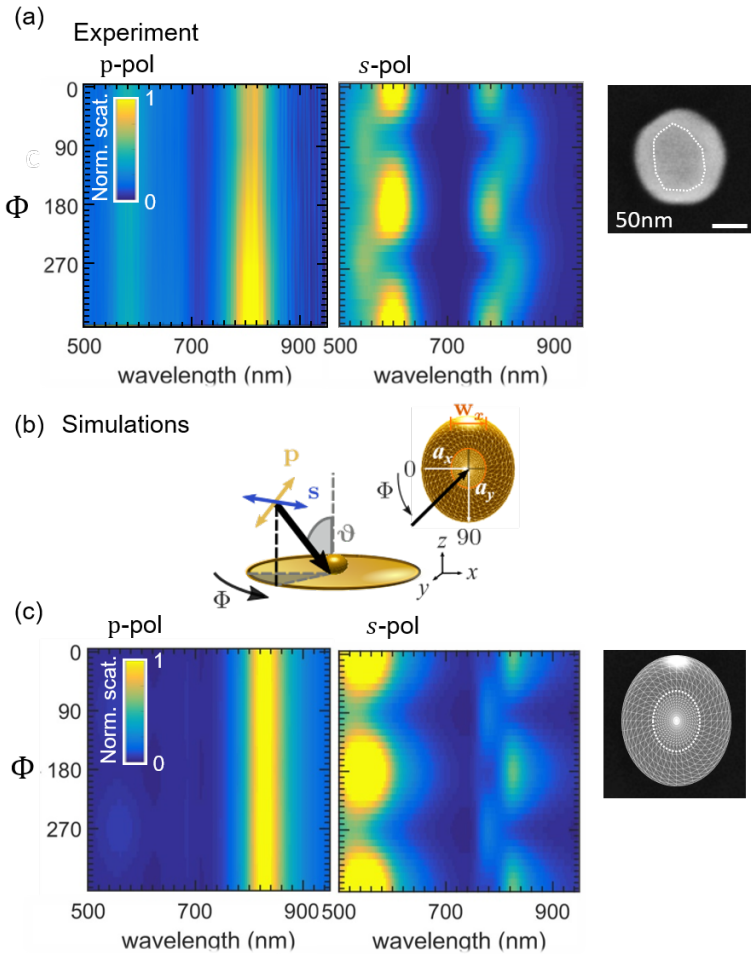

Figure 5.4: **Polarization-dependent dark-field scattering of a 80 nm faceted Au nanoparticle atop a 0.9 nm molecular spacer layer of CB[7] on a Au mirror (NPoM)**. (a) Experimental dark-field scattering spectra as a function of linear polarization angle (s,p-pol input), right side: SEM image, white dashed lines mark top facet.(b) Simulated structure: NPoM elongated along one axis into an ellipsoid, with semi-major axes of a_x=30 nm, $a_y = a_z$ =40 nm, and a facet width of w_y=25 nm, white dashed lines mark bottom facet.(c) Simulated dark-field scattering from NPoM shown in (b) for p-,s-polarized light.

lines) and varies between different nanoparticle shapes. This suggests that incident light polarized within the azimuthal plane (x,y-plane) along the nanocavity is capable of exciting gap modes. While normally dark, these become radiative due to symmetry breaking. More insight about the polarization dependent "splitting" is gained through comparing the experimental data with BEM simulations.

Using Boundary Element Method simulations described in section 3.2.2 the influence of faceting is analysed. The structure simulated is shown in Figure 5.4 b) and consists of a faceted nanoparticle on top of a Au substrate with a fixed gap of 0.9 nm and ε_{Au} from[4]. The faceted nanoparticle is realized by cropping of the bottom half of the nanoparticle disregarding the top facet. Exciting the NPoM from an in-plane direction Φ at an incident angle θ=55 degrees for p-/ s- polarizations, the experimental conditions were

reproduced. While the incident angle θ was kept fixed at the angle given by the NA of the objective, the polarization angle was changed. Rotation of the input polarization (from 0-360 degrees) for the s-coupled annular excitation in the experiment is realized by changing the incident direction in the simulations (Figure 5.4 b). Here, retardation effects due to the excitation from only one side are negligible. To match the experimental data in Figure 5.4 a), different nanoparticle structures were simulated tuning the resonance positions of the modes by adjusting the nanoparticle and facet size. Best agreement was found for a faceted sphere which is slightly elongated along one axis into an ellipsoid, with semi-major axes of a_x=30 nm, $a_y = a_z$ =40 nm, and a facet width of w_y=25 nm. Simulations using this geometry with p- and s-polarized light are shown in Figure 5.4 c). The spectral map for s-polarization consists of four modes matching the experimental mode positions well: 545 nm (T), 580 nm (Q), 780 nm and 830 nm (s_x, s_y). The characteristic quadrature polarization dependence of s_x and s_y modes as well as the 90 degrees phase shift is reproduced by the simulations. In contrast, the simulations for p-polarization confirm the polarization independence of the antenna mode seen in the experiment using unpolarized light in the excitation.

To gain a better understanding of the mode origins, the symmetry-breaking (Figure 5.5) is explored. This is realized by changing the axis ratio of the simulated ellipsoid and the ratio of facet size to nanoparticle volume. The simulated spectral response to s-polarized incident light as a function of incident directions is shown in Figure 5.5 a). The two higher wavelength peaks show an intensity maximum at $\Phi = 0, 90$, respectively. These two peak positions for the two perpendicular incident directions ($\Phi = 0, 90$) as well as polarizations (s,p) are extracted from the spectra as the incident angle is rotated around the nanoparticle (Figure 5.4 b). Focusing on the modes dominated by p-polarization one can see that distortion of the geometry has little effect on the z-polarized hybridized antenna-cavity modes (longitudinal p-modes; grey points Figure 5.5 b), except a small effect on the resonance position as a result of changing nanoparticle size[126]. Even for highly asymmetric nanoparticles the p-modes are degenerate and show no splitting for two incident directions ($\Phi = 0, 90$). By contrast, exciting with s-polarization for Φ=0 degrees (along x,◆) and 90 degrees (along y, ◆) shows how the modes directly track the facet width in the incident direction.

Fixing the height of the nanoparticle to 80 nm, but elongating the truncated sphere along the y-direction shows that the s_y mode depends most on the facet size w_y (Figure 5.5 b, dark blue line). The mode position is directly correlated with the cavity width in that polarization direction. Therefore when the facet becomes circular,the modes $s_{x,y}$ are degenerate (dashed horizontal line), while the s-mode splitting becomes more pronounced for larger asymmetries (with small effects on the Q mode at 580 nm also

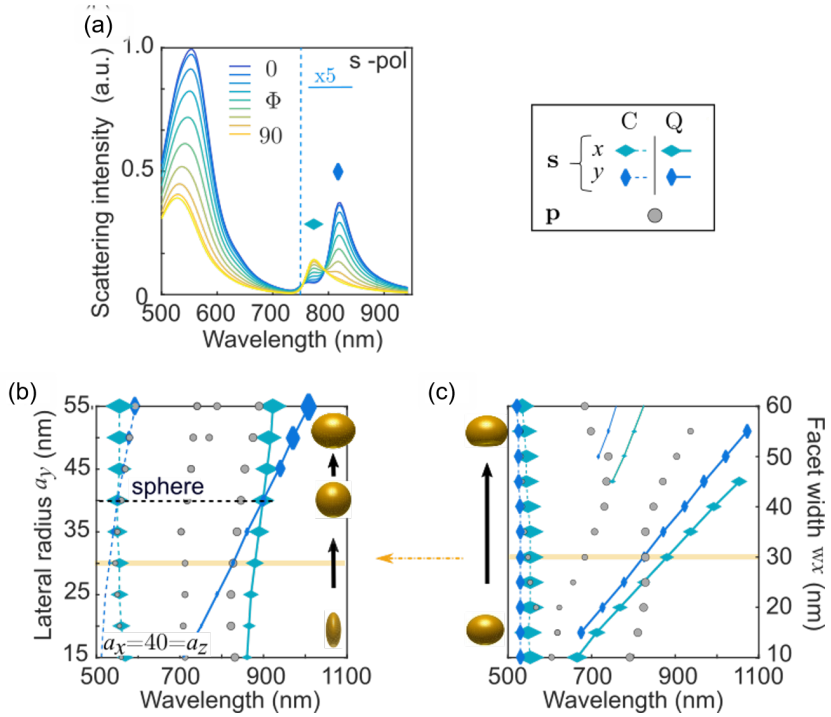

Figure 5.5: **Simulations of a NPoM construct with ellipsoid semi axes $a_{x,y}$, and facet widths $w_{x,y}$.** (a) Simulated scattering spectra for s-polarized incidence vs azimuthal angle ϕ (x5 for λ>750 nm). (b, c) Extracted peak positions (along x: blue, vertical diamond and y: turquoise horizontal diamond) of cavity and antenna modes for (b) changing aspect ratios a_x/a_y of a cropped ellipsoid on mirror with a 25 nm facet width, and (c) changing facet size of a 60 x 80 x 80 nm cropped ellipsoid on mirror. Orange line indicates facet width in (b). Size of marker points in (b,c) shows the amplitudes of each mode at extracted peak positions.

seen).

Increasing the faceting of the nanoparticle while keeping the facet asymmetry fixed (Figure 5.5 c) shows that the relative splitting is preserved (light/dark blue lines) but facet-dependent spectral splitting is seen as the facet diameter increases. Changing the incident linear polarization for s-coupled light thus clearly accesses cavity modes along different facet directions, where higher wavelength correspond to a longer cavity width w. For very large facets (w_x >45 nm) higher order modes appear. These modes are similarly spectrally split. In the other limit for very small facets the cavity modes become less pronounced while without the facet, these cavity modes are suppressed. From Figure 5.5 c) it is evident that the p-modes are polarization independent even for larger facets. The mode position only tunes with facet size, but show now polarization splitting. Although p-modes depend on nanoparticle size,[126] gap size,[110] and average facet width,[133] they are not sensitive to the exact geometry of the facet and its asymmetry.

Charge Distribution

Looking at the charge distribution of the different modes, the polarization dependence on the incident direction becomes more evident (Figure 5.6 c). The dipolar p-mode and

the quadrupolar Q-mode show a surface charge distribution around the entire particle. While the dipolar mode is completely centrosymmetric the Q-mode shows a nodal plane around the surface (bottom panels). By contrast, the $s_{x,y}$ modes are strongly confined to the nanocavity gap (top panels). The modes show almost no charge distribution around the top of the particle, emphasizing their different origin and character. As anticipated,

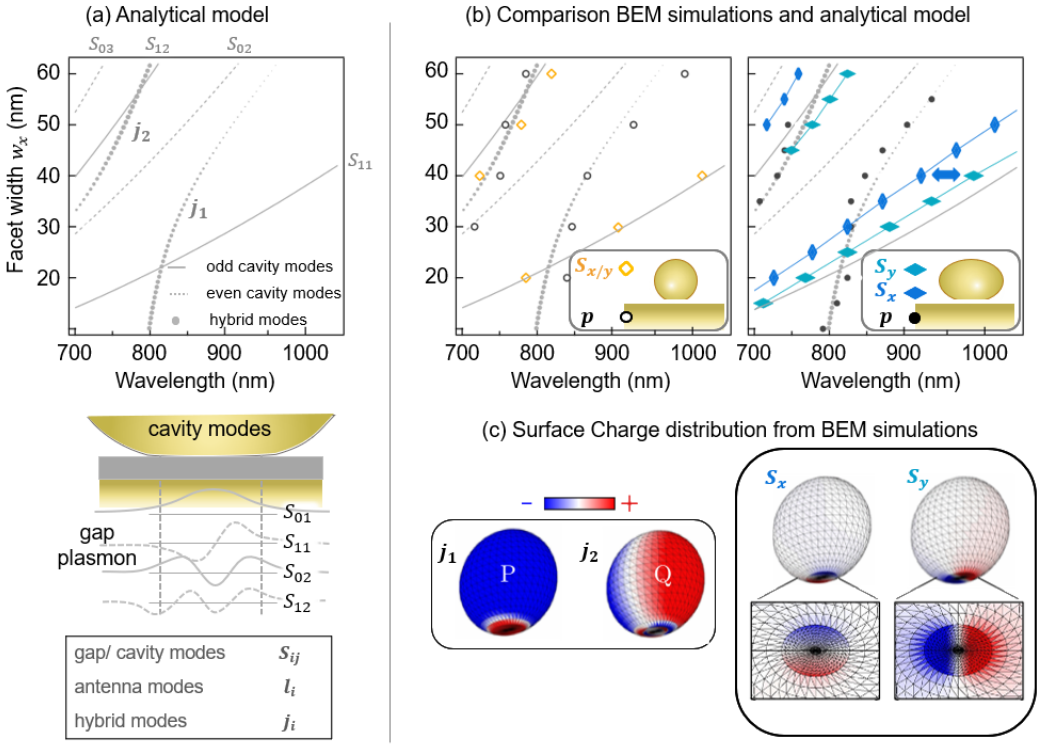

Figure 5.6: **Comparison BEM and analytical MIM model** (a) Analytical cavity model. Top: cavity modes (gray lines solid = odd, dashed = even) and hybridized modes (grey dots) as a function of facet width. Bottom: schematic field distribution of even and odd order cavity modes s_{ij}. (b) Comparison of analytical model (grey) and full BEM simulations (orange points = sphere and blue markers = ellipsoid. (c) Simulated surface charge distribution for slightly elongated ellipsoidal Au NPoM (a_x=30 nm, a_y=a_z=40 nm) on Au substrate with 0.9 nm gap. Right panels show the two gap confined cavity modes $s_{x,y}$ while left panels display radiative dipolar j_1- and quadrupolar j_2-modes.

$s_{x,y}$ directly relate the polarization splitting to the orientation of the facet modes. They show charge separation along the two perpendicular axes of the facet for the different incident direction.

Analytical MIM Model

The previously discussed analytical model for the MIM waveguide modes given by equation 4.1 is shown in 5.6 a). Cavity modes are depicted in grey lines (odd order s-modes = solid, even order s-modes = dashed), while grey dots mark the hybrid modes. A direct comparison of the BEM simulations (same parameters as before) with the MIM waveguide modes (5.6 b) shows that the s-modes coincide with cavity modes. In Figure 5.6 b) on the right hand side the dark odd modes (solid) and bright even modes (dashed) are

shown (grey lines) super-imposed on the p-modes (○) and s-modes (◇) of the exact simulations for spherical nanoparticles. For the sake of completeness the modes of the ellipsoidal nanoparticles (● and ◆,◆) are shown on the left hand side. The sphere has degenerate s-modes which match equation 4.1 extremely well for the s-modes with order $i = 1$. The even order modes (s_i=0) hybridize with the p-modes, forming mixed modes that show anti-crossing as a function increasing facet size in the unpolarized scattering response (As discussed in section 4.3). The odd order modes don't mix and therefore remain dark for unpolarized dark-field scattering. However comparison with the analytical model suggests that s-polarized light used here is capable of exciting these usually-dark odd symmetry cavity modes. If the facet is non-circular, the spectral s-mode positions depend on the effective nanocavity length in the direction of the optical field (the s_x mode has a shorter cavity and thus higher energy compared to the s_y mode, Figure 5.6 b). The polarization-dependent mode splitting is only ever two-fold symmetric and maximized for rectangular or elliptic facets. The much stronger out-coupling of p-modes arises from the even-cavity mode coupling to the antenna modes, which results in hybrid modes that anticross (dashed open circles, Figure 5.6 b) as discussed previously.[115,116] In contrast, the s-modes cannot couple to the antenna mode due to their symmetry, and are only weakly emitted.

Orientation and Eccentricity of Bottom Facet

This analysis makes it possible to explore the behaviour of many different NPoMs with different facet morphologies and shapes. In Figure 5.7 the polarization dependent dark-field scattering spectra of a few representative nanoparticles are shown. The particle shape and orientation is shown in the inset obtained via SEMs on exactly the same nanoparticles. Here it has to be noted that imaging techniques such as SEM and TEM use accelerated high energy electrons to the sample surfaces and are therefore highly invasive. Several studies report nanostructure damage occurring during SEM imaging[145,146] accompanied by changes in their optical properties. In order to maintain the optical properties the SEM images are taken after the optical characterization. Using a diamond cutter the sample was marked with several scratches to identify the area of interest. Images of different magnifications were taken of the are of interest to later match the corresponding nanoparticles and their orientation to the SEM images. The raw polarization-dependent spectra (Figure 5.7 a) show considerable variation in response, which is in agreement with the variety of faceted nanoparticle images obtained from electron microscopy (Figure 5.7 a, insets). The peak maxima for the s_x and s_y modes, are indicated with orange and blue arrows respectively in the polarization maps (Figure 5.7 b). Using the same orientation of the sample these are then transferred to incident angles in the SEM images indicating the axis of the underlying facet.

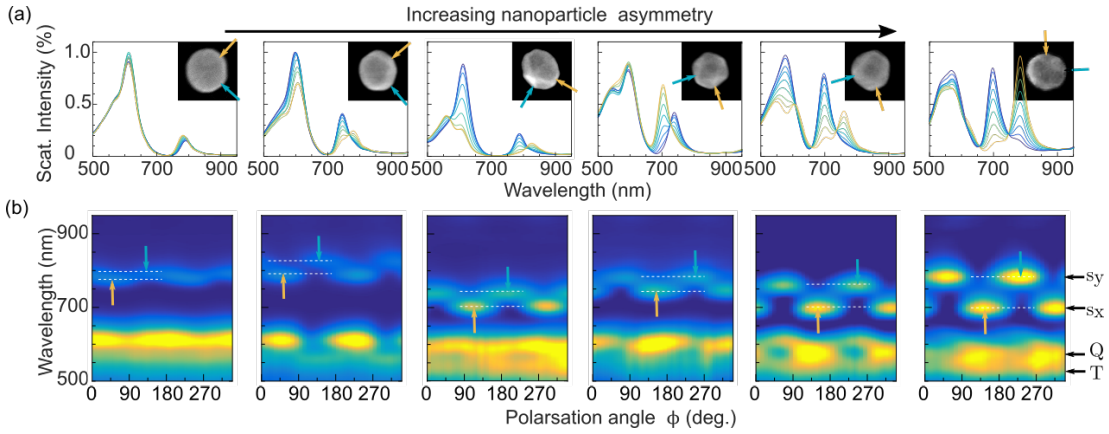

Figure 5.7: **Nanoparticle shape and faceting** (a) Dark-field scattering spectra for 80 nm Au faceted NPoMs correlated with SEM images (insets). Orange and blue arrows in SEMs indicate polarization angle of maximum intensity for the s_x and s_y modes respectively. (b) Polarization maps, which provide optical orientations (orange and blue arrows) used in (a). Dashed white lines mark the spectral splitting, which increases with growing asymmetry (to the right).

The spectral mode separation is emphasized with white dashed lines. Strong variation is seen at longer wavelength s-modes. In agreement with the simulations, the spectral mode splitting increases with increasing particle asymmetry seen in the SEM images (when reading from left to the right). For highly asymmetric particles the increased mode splitting is accompanied by increasing scattering strengths, changing the ratio of the scattering intensities of the T/Q-mode to the s-modes. Furthermore, the intensity ratio of the two split modes becomes more equal, also agreeing with theory.
As a result the splitting can be used as a direct measure of the aspect ratio of the bottom facet, with the spectral eccentricity

$$e = \sqrt{1 - \left(\frac{w_y}{w_x}\right)^2} = \sqrt{1 - \left(\frac{\lambda_y^2 - \lambda_p^2 \varepsilon_\infty}{\lambda_x^2 - \lambda_p^2 \varepsilon_\infty}\right)^2}. \tag{5.1}$$

The extracted distribution of eccentrics e_n for 100 NPoMs is plotted in Figure 5.8 a). The distribution peaks at an average eccentricity $\bar{e} \approx 0.5$, corresponding to elongated NPs with a facet ratio of 2:1 (Figure 5.8 b, inset). The distribution of e_n reveals that virtually all NPs deviate from spheres, giving a polarization splitting.

Extracting the peak positions of the two s-modes, the average resonance position $\bar{\lambda}_s$ which corresponds to the average facet width is calculated. Displaying the variation in mean resonance position $\bar{\lambda}_s$ (Figure 5.8 b) versus the eccentricity, it becomes evident that the facet size is positively correlated with the s-mode splitting (and therefore eccentricity e) - larger facets are thus more asymmetric.
From BEM simulations, increasing one of the facet axis by only one atom (with atomic spacing 0.4 nm[116]) leads to a spectral splitting of $\Delta\lambda$=3 nm. Taking into account the

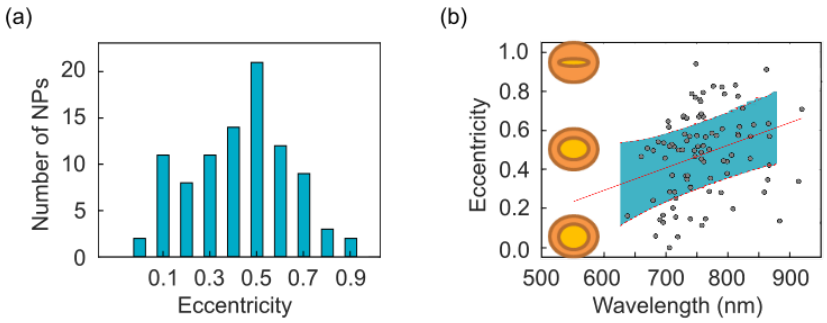

Figure 5.8: **Statistics of nanoparticle faceting and eccentricity** (a) Distribution of extracted facet eccentricity e_n for 100 NPs, plotted in (b) vs mean resonance position $\bar{\lambda}_s = 0.5\left[\lambda(s_x) + \lambda_(s_y)\right]$. The distribution peaks at an average eccentricity $\bar{e} \sim 0.5$, corresponding to elongated NPs with a facet ratio of 2:1.

spectral resolution of the spectrometer this in theory allows morphological changes in the facet ratio to be tracked down to the single atom level.
Combined p- and s- polarized measurements thus allows precise description of the nano-constructs. While p-polarized light couples to the antenna mode that is highly sensitive to NP size and gap distance, s-polarized light is able to access detailed information about the size and shape of the facet at the bottom of each Au nanoparticle, giving a polarimetric plasmon ruler.

However a number of details remain puzzling. In particular, the Q-mode polarization signature. In the experimental data the Q-mode intensity sometimes is strongest whenever the shortest wavelength s-mode has a scattering maxima and other times it aligns with the longer wavelength s-mode. This is shown in Figure 5.9. While the $s_{x,y}$-modes show a consistent 90 degree phase shift the Q-mode is either in phase with the shorter wavelength s-mode (Figure 5.9 a) or the higher s-mode (Figure 5.9 b). In simulations however, the Q-mode only aligns spectrally with the longer wavelength s-mode (Figs.5.4 c). This consistent result shows that an extra mixing is missing in the simple analytical cavity model. Additional factors influencing the optical response, such as orientation and symmetry of the top facet and edge rounding of the facets, need to be included in the model. However, the general trends and the effectiveness of the analytic model verify the correct origin of the observed polarization splitting.

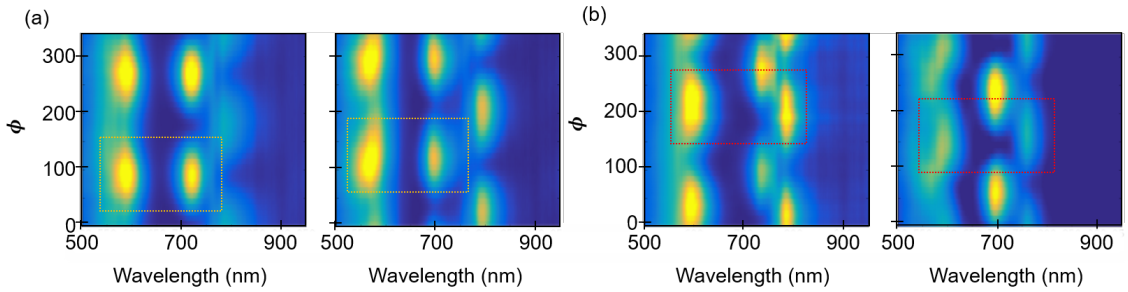

Figure 5.9: **Different alignment of the Q-mode is respect to the gap s-modes as a function of polarization angle** Polarization-dependent dark-field scattering of different 80 nm faceted Au nanoparticle atop a 0.9 nm molecular spacer layer of CB[7] on a Au mirror (NPoM). (a) The Q-mode aligns with the lower wavelength s-mode (orange box) and (b) with the higher wavelength s-mode (red box)

5.3 Conclusion

In this chapter it was shown that polarization-dependent dark-field scattering can be used for non-invasive characterization to probe metallic nano-structures at the sub-nanometer scale. Within coupled systems this method identifies the asymmetry and orientation of plasmonic nano-cavities, which are hidden underneath nanoparticles and which are inaccessible to conventional imaging methods. The simulations imply that s-modes seen in the experiment are tightly-confined odd transverse cavity modes. While usually dark because of their symmetry, these modes become bright and can radiate into the far field due to the rounded edges of the nanoparticle and non-normal illumination on the flat mirror, revealing the detailed morphology of the nano-cavity. Polarization splittings in dark-field scattering can therefore directly be related to the asymmetry of the gap morphology. Comparing experimental results on hundreds of NPoMs to simulations and a simple analytical MIM model reveals the origin of these plasmonic coupled modes and demonstrates their tuneability, making them ideal candidates for ultra-sensitive plasmonic sensing on the nanoscale. Both experiment and simulation show the dramatic influence of the nano-cavity on the coupled system, with spectral shifts λ=3 nm from changes of adding single atoms.

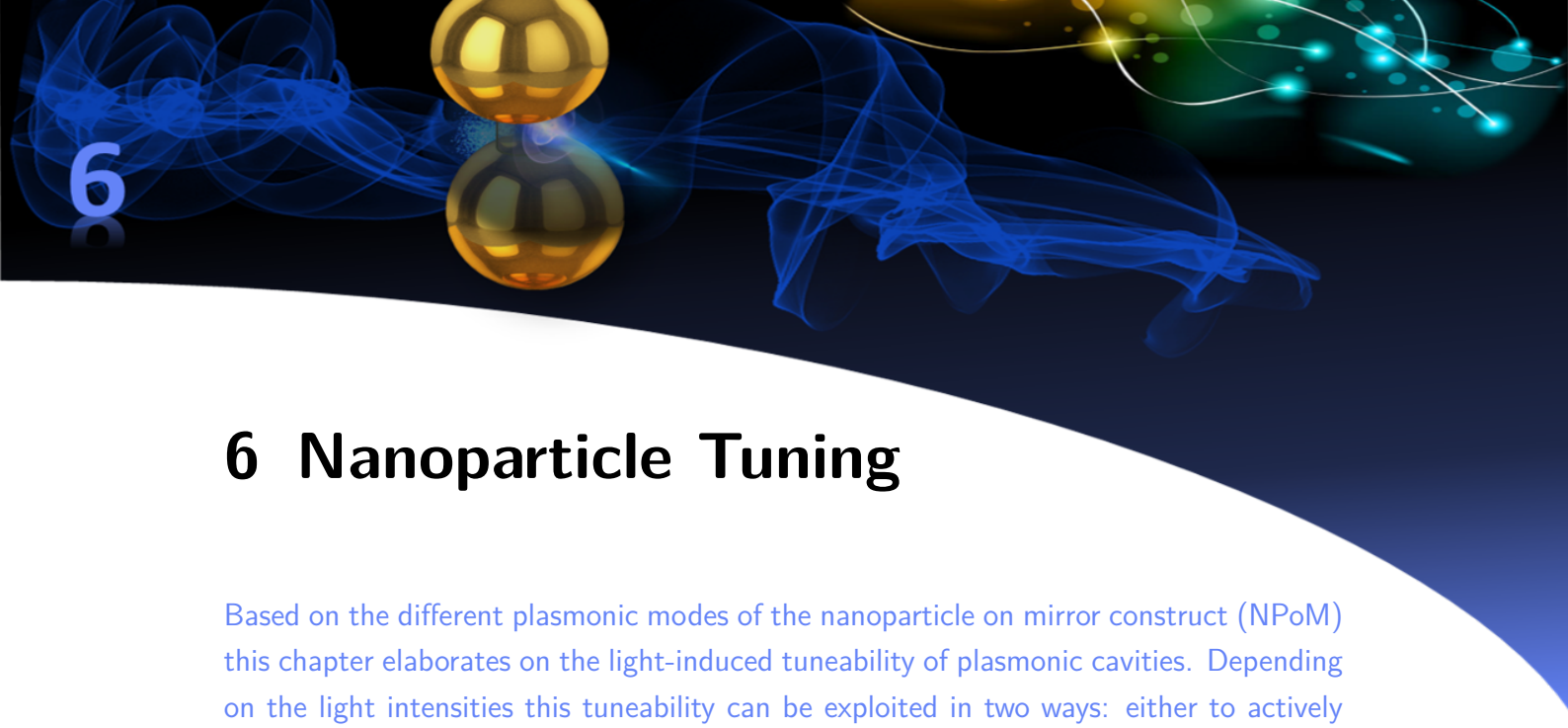

6 Nanoparticle Tuning

Based on the different plasmonic modes of the nanoparticle on mirror construct (NPoM) this chapter elaborates on the light-induced tuneability of plasmonic cavities. Depending on the light intensities this tuneability can be exploited in two ways: either to actively induce modifications of the cavity morphology or for lower light levels as a sensing platform to characterize the cavity. In the first case intense light is used to reshape the cavity morphology, which actively tunes the NPoM resonance wavelength. Such experiments offer exquisite control to re-sculpture individual nanostructures in real-time. In the second case changes of the cavity architecture and its surroundings are tracked in an optical feedback loop. Thus, processes that involve light-induced assembly or growth can be optically monitored, resolving changes on the atomic scale.

Exploiting the low activation energy of gold ad-atoms on the nanoparticle surface, it is shown how blue laser irradiation can be used to re-sculpture the cavity morphology formed in NPoM constructs and nanoparticle dimers. Comparison of different spacer materials such as semiconducting "hard" spacers and molecular "soft" spacers, two regimes can be identified: facet growth or conductive bridge formation. The growth of the facet width is directly linked to spectral red-shifts in the far-field scattering, providing information about the underlying reconstruction process. Polarization dependent dark-field microscopy further reveals the direction of the facet growth and its uniformity. For soft spacers conductive filaments form, bridging the nanogap between the nanoparticle and its underlying mirror. In this regime clear spectral anti-crossings mark the different growth stages. FDTD simulations are used to confirm the growth dynamics and extract the bridge diameter. Finally nanoparticle dimers are used to study the reproducible formation of such filaments [1].

[1] Experimental work was undertaken with J.Mertens and A. Salmon. FDTD simulations were carried out by Angela Demetriadou. Parts of this chapterhave been published in reference [72] and [133]

Designing and tuning nanomaterials with tailored optical properties has potential applications in many areas, such as electronics[147], communications[148], metamaterials, optical and bio sensing[10], nano-imaging[101,149] and energy harvesting[150].
In this context one can distinguish between reversible tuning and permanent reconfiguration[151]. Ultra-fast modification of material properties is used to switch between two states reversibly. Information processing speeds reaching up to 10 Gbits/s[152,153] make this ideal for high throughput data processing and fast optical switches.
In contrast permanent reconfiguration of nanostructures happens on slower scales and plays an important role in high-density data storage and sensing applications, for example when studying processes that involve vibronic or electronic transitions. On one hand sensing techniques such as surface enhanced raman scattering (SERS), tip enhanced raman scattering (TERS) and plasmon enhanced photoluminesenscence (PL) depend exquisitely on matching transition energies of molecules or semiconductors with the plasmonic resonance[85]. On the other hand, to develop nanodevices that are based on selective modification of individual nanostructures such as optical data storage it is essential to understand the underlying mechanisms of nanoscale reconstruction[146]. This becomes especially important in cases where contactless and non-invasive characterization techniques are needed, for example nanoscopic resistive switches called "memoristors". These devices rely on the reproducible formation and rupture of conductive filaments sealed between two electrodes. Optical characterization of the filament growth and dissolution mechanisms offers great insight into the switching dynamics.
This chapter will mainly focus on permanent tuning of plasmonic cavities.

6.1 Laser Induced Tuning of Plasmonic Cavities

The excellent photo-thermal conversion efficiency of plasmonic nanostructures offers a promising new route to selectively re-sculpture nano constructs harvesting light. The low oxidation rate at high temperatures, good plasticity and low activation energy of gold make it a good candidate for laser induced reconstruction[151]. Furthermore, its plasmonic properties make gold superior to other metals. The localized nature of plasmonic heating, which is due to the confined field enhancement, allows for the precise modification of individual nano scale features without damaging the surrounding or underlying substrate[147]. While it has been shown that different shapes and sizes of single nanoparticles tune the plasmon resonance over a broad spectral range, plasmonic coupled structures are predicted to yield the highest field enhancements and tuneability with decreasing inter-particle gap sizes[21,82,133,154–156].The non-resonant lightning rod effect produces extra enhancement and subnanometric localization of electromagnetic fields due to the

presence of atomic-scale features at the interfaces of plasmonic gaps[112]. This can be exploited to re-sculpture nanostructures with atomistic precision. In the following section the experimental realization of such nanometric optical welding is introduced.

Experimental Realization of Nano-welding

UV-laser irradiation is realized through coupling in a 447 nm or a 403 nm CW Cube laser (Coherent) with an additional beamsplitter in the excitation beam path of the dark-field setup (Figure 6.1 a). The UV light coincides with interband transition of the d-band in gold and leads to an effective light-to-heat conversion (Figure 6.1 b). However, equal re-sculpturing behaviour can be observed using laser light below the interband absorption (633 nm, 785 nm). Even though the UV laser is non-resonant to the plasmon, significant field enhancement is still present due to the lightning rod effect at curved metallic surfaces[112,157].

The laser beam is expanded to fill the back aperture of the objective to focus the light into a diffraction limited spot on the sample. The small spot size of 250 nm, enables the irradiation of individual NPoM constructs. Dark-field scattering spectra are used to monitor morphological changes in real time. Long-time irradiation measurements of the order of several hours are carried out on the BX51 setup described in 3.1.2, where software drift compensation and autofocus routines account for thermal and vibrational induced drifts of the sample. Polarization dependent dark-field measurements are carried out on the self-built dark-field microscope described in section 3.1.1. Here, the UV-laser is coupled in to the detection beam path. Laser leakage is filtered out by a 500 nm longpass filter (LP) placed in the detector arm before the spectrometer. Polarization dependent dark-field scans before and after laser irradiation provide additional information on the symmetry of the nanostructure as described in detail in chapter 5.

In the following, two dynamics of nanowelding are discussed for the different types of spacer materials: hard spacer materials consisting of mono -and multilayer TMD materials introduced in section 2.2 and organic, soft spacer materials such as CB[7] and TPT (section 4.1.1). While both cases show active tuning during UV laser irradiation, their growth dynamics differ substantially.

6.1.1 Hard Spacers - Facet Growth

Monolayers of WSe_2 and MoS_2 are incorporated into NPoM constructs using the self-assembly method described in section 4.1.1. As robust spacer layers they prevent charge transfer from the gold nanoparticles to the gold substrate. These materials also posses unique electronic and optical properties. However, this will be discussed in the next

chapter as these are not contributing to the optical tuning of the plasmonic system. 60 nm and 80 nm Au nanoparticles were used with monolayers and bilayers of WSe_2 to tune the plasmon resonance into the visible range.

Figure 6.1 shows sequential dark-field scattering spectra of a NPoM construct with a 0.7 nm monolayer of WSe_2 during irradiation. Each spectra is taken after 0.5 s laser irradiation of 0.1 mW power at the sample. The laser power and exposure time is set sufficiently low to be able to observe tuning without damaging the nanoparticle. While there is very little effect seen on the transverse mode (T, indication that the nanoparticle remains intact), a clear red-shift of the coupled modes at 610 nm and 740 nm is seen during irradiation. These shifts are permanent as they do not reverse when the laser is turned off. The rate of the occurring red-shifts is highly dependent on laser power and the nanoparticle shape. Comparison to BEM simulations and the analyti-

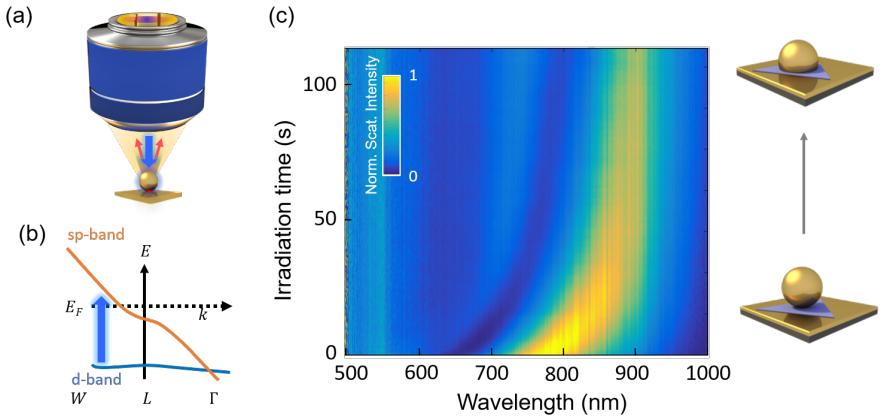

Figure 6.1: **Optical signature showing laser induced surface migration of gold atoms.** (a) Schematic of irradiation setup using a commercial BX51 microscope. Dark-field scattering spectra are measured simultaneously during irradiation. (b) Using a 403 nm and a 447 nm laser the interband transition of gold are efficiently excited. (c) Subsequent dark-field scattering spectra show tuning of the plasmonic modes as a function of irradiation time. Ad-atomic drifts of gold atoms towards the bottom of the nanoparticle cause facet growth (schematics on the right), which red-shifts the plasmonic modes.

cal waveguide model for faceted nanoparticles introduced in chapter 4, reveals that the red-shift of the coupled modes with subsequent laser irradiation can be explained by facet growth. Nanoparticles are highly faceted, which influences the spectral position of plasmonic modes in the NPoM geometry. Mixing of tightly confined gap modes and antenna modes leads to the formation of hybrid modes, which are extremely sensitive to the precise gap morphology. While the gap modes are usually dark they become brighter in the spectral region close to the antenna modes due to mixing (for more details see section 4.3).

During laser irradiation gold atoms move towards the gap region of the NPoM, causing the bottom facet to grow. The increased facet size changes the resonance condition of

the gap modes. While equal red-shifts can be produced by decreasing the spacer thickness this is unlikely to be the cause of the red shifts as the spacer layer remains intact throughout the experiment. This is confirmed by unchanged surface-enhanced Raman scattering (SERS) before and after irradiation (see Figure 7.3). Comparison with the analytical cavity model shows the 150 nm red-shift seen in the experiment can be ascribed to a facet growth of $\sim$30 nm. Each restructuring event has its individual laser power threshold. For laser powers significantly greater than the threshold power, the modes quickly shift to the infra-red, too fast to be measured. For laser powers close to the threshold power the individual rates for the hybrid modes j_1, j_2 vary - longer wavelength modes tend to shift faster. However, all shifting rates decrease with increasing irradiation time. This saturation in the shifting rates can be understood approximating the facet as circular. The facet area scales as $\pi(w/2)^2$ suggesting a quadratic growth rate, that slows down as more atoms are needed to increase the facet area with larger facet width. The decrease in scattering intensity with increasing red shift of the modes is caused by the drop off in detection efficiency in the NIR.
The exact mechanisms whether thermal, optical forces or surface energy are the dominant driving forces of these drifts is still unclear. Yet being able to monitor these changes optically, information about the dynamics of these process can be gained. Imaging techniques such as SEM and TEM are highly invasive, changing the optical properties completely. Furthermore in the case of the NPoM geometry the plasmonic cavity remains hidden underneath the nanoparticle, inaccessible for conventional imaging techniques. The drift of surface atoms towards the bottom facet suggests optical forces and thermal forces as the dominant driving forces as this is where highest field intensities are expected. However due to the large loss associated with plasmonic modes, these two forces are very difficult to separate as the high plasmonic enhancement is always accompanied with heating. Further studies analysing the spectral shifting as a function of Laser peak power and excitation wavelength are needed to gain more insight into the underlying driving forces. Furthermore, using unpolarized light the directionality of the facet growth remains unresolved. This information is gained by s-polarized dark-field microscopy.

Polarization Signature

The directional growth dynamics are probed by subsequent polarization scans of the irradiated constructs. The s-polarized light accesses dark-cavity modes (s-modes) that are highly sensitive to the symmetry and width of the bottom facet (for more details see chapter 5), while larger facets shift the s-modes to higher wavelength, higher eccentricity of the bottom facet leads to an increase in the s-modes splitting (Figure 5.5 c,d).

Two typical polarization responses during irradiation are shown in Figure 6.2 a,b) (85 nm diameter nanoparticle on top of a 0.7 nm WSe_2 layer). Between each subsequent polar-

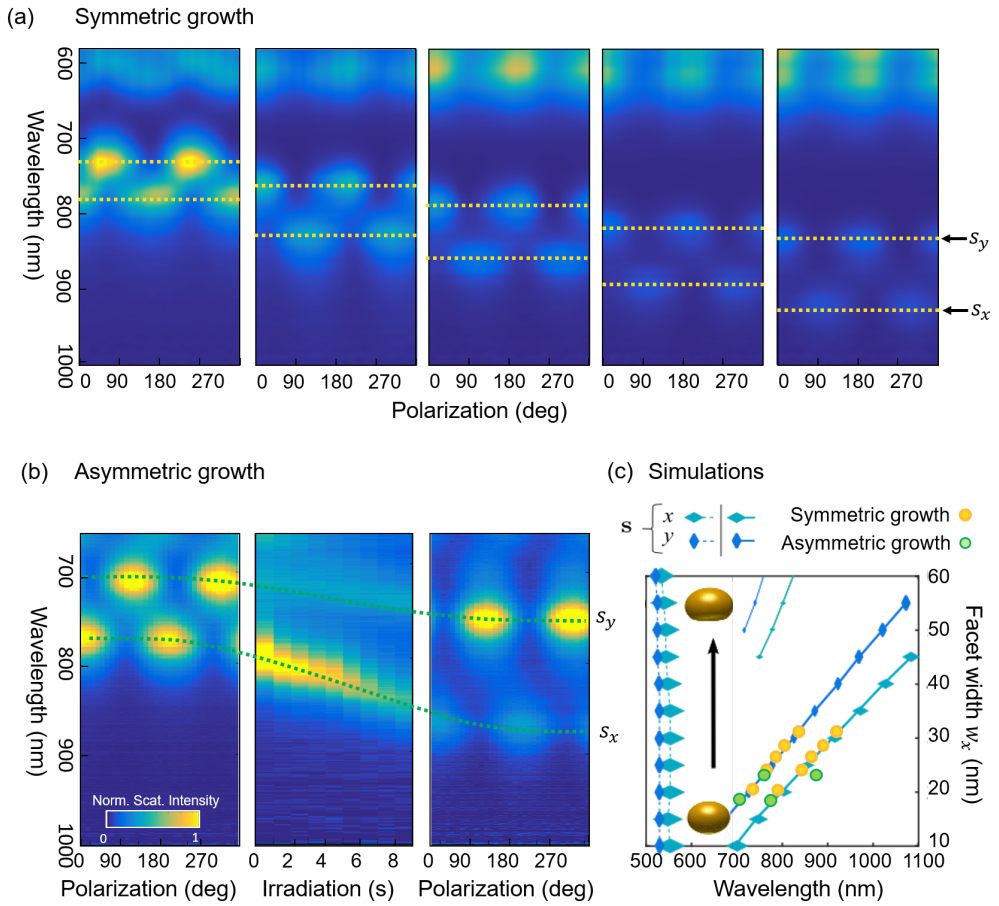

Figure 6.2: **Monitoring facet growth with subsequent polarization scans before and after irradiation of WSe_2 NPoM constructs.** Polarization response reveals different growth dynamics: (a) Symmetric facet growth or (b) asymmetric facet growth. Using the costum build dark-field microscope the NPoM is irradiated for 10 s with 0.1 mW power (at the sample) between each polarization scan (during irradiation the linear incident polarization is set to 45 degrees, middle panel in b). (c) Comparison of boundary element simulations (BEM, blue diamonds) and extracted peak positions from experimental data (round markers). Simulated cavity modes with symmetric facet growth of a 60 x 85 x 85 nm cropped ellipsoid on mirror (along x: blue, vertical diamond and y: turquoise horizontaldiamond). Experimental data: extracted peak positions of s-modes from (a) (orange) and (b) (green).

ization map the NPoMs are irradiated for 10 s with a 403 nm UV laser producing laser powers of 0.2 mW at the sample. During irradiation the polarization is set to 0 degrees with an intensity maxima in the s_x mode and a minima in the s_y mode. This is due to the drop off in intensity for longer wavelength. In order to track the s_x-mode as it shifts into the near infra-red this is set to its maximum intensity. Dashed lines (yellow,green) are overlayed on the dark-field scattering spectra and mark the peak positions of the s_x and s_y modes. Reflected in their polarization signature, the two examples in Figure 6.2 (a,b) demonstrate different facet growth dynamics: Symmetric growth, where the aspect

ratio of the bottom facet remains unchanged and asymmetric facet growth showing an increase in the eccentricity of the bottom facet. In the case of symmetric growth the polarization maps show two clear split modes at 760 nm and 822 nm, corresponding to an initial facet size of ∼21 nm (Figure 6.2 c, orange markers) and an eccentricity e of 0.6 (see equation 5.1). Both modes tune to higher wavelength during irradiation showing similar rates. The shifts in peak position are accompanied by a drop in peak intensity. After 40 s of irradiation a slight increase in the splitting is observed. However, the polarisation angle of the intensity maxima for the s_x and s_y remain unchanged after irradiation, indicating that the orientation of the bottom facet is fixed.
Boundary element simulations (BEM) are carried out to extract the facet width. Best agreement is found for a 60 x 85 x 85 nm cropped ellipsoid (inset, Figure 6.2 c). Increasing the facet width w but keeping the aspect ratio of the facet fixed, the relative splitting is preserved reproducing the trend seen in the experimental data (orange markers). Comparison to BEM simulations thus confirms that the orientation and aspect ratio of the bottom facet remains unchanged during this growth process of the facet width from 21 nm to 32 nm. In contrast during asymmetric growth the relative splitting of the two s-modes changes drastically. The initial mode splitting between 710 nm and 770 nm suggests an eccentricity of 0.6. After 10 s of irradiation the subsequent peak positions show an increased splitting of 125 nm, corresponding to an eccentricity of 0.8 (Figure 6.2 b). BEM simulations show that the increase in the mode splitting (green markers) cannot be reproduced by symmetrical facet growth (blue solid lines). Instead changes in the aspect ratio of the bottom facet lead to a larger mode splitting. The higher eccentricity suggests an inhomogeneous facet growth which dominates in one direction. Thus, monitoring the polarization splittings during irradiation reveals crucial information about the plasmonic cavity hidden underneath the nanoparticle and how atoms move about on these systems. The s-mode peak shifts and splitting ratios can be directly related to the asymmetry of the gap morphology, revealing different facet growth dynamics.

6.1.2 Soft Spacers - Conductive Bridging

NPoM constructs with "soft" self-assembled monolayers are fabricated (for more details see section 4.1.1) and irradiated. The subsequent dark-field scattering spectra during irradiation are shown in a color map in Figure 6.3. To enable long term irradiation, the measurements are carried out on the Olympus BX51 microscope with incorporated drift compensation. A UV-laser power of 0.1 mW and an exposure time of 0.5 s were used.
Initial red-shifts of the modes suggest an early facet growth (bottom of Figure 6.3 a,b). This stage is then abruptly ended by a sudden blue shift after 50 min. Over the time of irradiation several further blue shifts occur. Each shift starts in the infra-red and

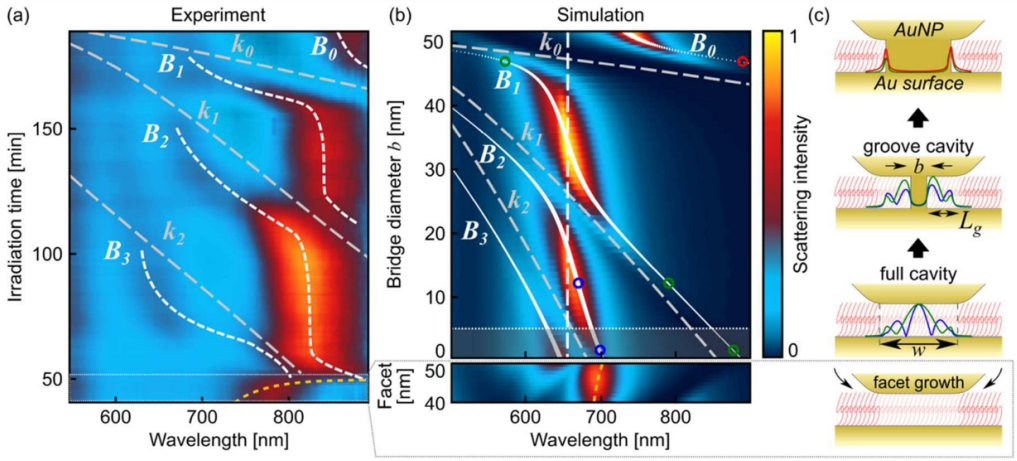

Figure 6.3: **Irradiation of a typical NPoM construct with 1,1',4',1"-terphenyl-4-thiol (TPT) as "soft spacer"** (a) subsequent dark-field scattering spectra of the NPoM system as a function of laser irradiation using a commercial BX51 microscope. White dashed lines highlight the different modes B_n. The cavity modes k_n calculated from the analytical cavity model introduced in section 4.3 are marked with grey dashed lines. (b) Finite-difference time domain simulations reproducing the experimental conditions with increasing bridge diameter depicted in (c). The simulated scattering spectra corresponds to a NPoM with a facet width w=51 nm and a conductive bridge forming at the centre of the cavity with bridge diameter b. (c) Schematic of the conductive bridge formation. Curves show mode intensity distributions in the center of the gap. The corresponding spectral positions of are marked with open circles in (b).

shifts towards visible wavelengths revealing several anti-crossings. White dashed lines are overlayed on the image to guide the eye, indicating the different emerging modes B_n.

This sudden transition can be understood from FDTD simulations. The rapid blue shifts are reproduced by introducing a conductive bridge in the plasmonic cavity which electronically shorts the gap (Figure 6.3 c). The experimental data is matched by simulating an 80 nm nanoparticle with an increasing facet of w=40 nm to w=50 nm in the non-conductive regime. The sharp anti-crossings in the conductive regime are simulated by a steadily growing bridge diameter b in the centre of the bottom facet. The bridge formation not only leads to a charge transfer between the nanoparticle and the underlying mirror, but also modifies the cavity modes.

Four distinct modes B_{0-3} can be identified in the experimental data and simulations. Each of the modes shows a clear blue shift with increasing bridge diameter. The transition of each mode to the next displays an anti-crossing indicating mixing of the different modes.

The anti-crossing can be understood within a perturbed analytical cavity model (for more detail see section 4.3). The new facet length L_g is given by the shortened cavity

formed between the edge of the facet and the bridge: $L_g = (w-b)/2$. The corresponding resonance conditions $L_g = m\lambda_m/2$ and therefore resonance wavelength is:

$$\lambda_m = \frac{w-b}{m+\varphi/(2\pi)} \tag{6.1}$$

with m=0,1,2... being the order of the groove modes and φ a phase factor to account for the different boundary condition at the edge and the bridge in the middle of the facet. Using the MIM waveguide dispersion $k_m = 2\pi/\lambda_m$, the corresponding energies of the groove modes can be calculated and solving the eigenvalue problem $E\Psi = v\Psi$ (E: coupling matrix of cavity and antenna modes, Ψ: eigenvector, v: eigenenergies of the system) the hybrid mode energies v are extracted. The new predicted hybrid modes B_{0-3} are plotted on top of the full simulations with white solid lines (Figure 6.3 b). The width of the plotted hybrid groove modes corresponds to their radiative component (due to coupling to the antenna mode). Dashed grey and white lines in Figure 6.3 a,b) correspond to the cavity modes k_m and the antenna mode respectively. The analytical model captures well the blue shifts and subsequent anti-crossings caused by the reduction of the cavity length with increasing bridge diameter.
Different nanoparticle-on-mirror constructs display different laser power thresholds initiating surface migration of gold atoms. However, the process itself is very reliable: the growth mechanisms always starts with an initial red-shift indicating facet growth followed by the transition to the conductive regime, which is marked by rapid blue shifts. As soon as the laser is turned off the process stops and the conductive bridges remain stable until the laser is turned back on again. Once the threshold laser power is reached, a large variety of bridging events can be observed. The transitioning speed as well as the final bridge diameter show little consistency when the laser power is left constant at the threshold power. To gain further control over the growth dynamics the influence of the laser power is studied.

6.1.2.1 Power Dependent Growth Dynamics

More insight into the dynamics during conductive bridging is gained by employing higher light levels and faster integration times. Linear power series were carried out on the custom built dark-field setup described in section 3.1.1. Here, linear polarized light in the excitation yields s-polarized light with the E-field oscillating parallel to the sample plane. In this configuration plasmonic dimers are preferred over NPoM constructs for two reasons: Firstly, the connection axis of the dimers lies in plane (in contrast to the NPoM geometry, where it lies along the z axis). This allows the use of polarization scans to distinguish between monomers, dimers and aggregates and to map out the orientation of

the dimer (Figure 5.2). Secondly, nanoparticle dimers on glass slides reduce the influence of heating the metallic substrate. Using UV laser irradiation the interband transitions of gold are resonantly pumped. Therefore, the absorption of the gold substrate has a large influence o the re-sculpturing dynamics during irradiation.

Fabrication of nanoparticle dimers

The dimers are fabricated in solution. Here 20 μl CB[7] stock solution is added to 250 μl of 80 nm BBI gold nanoparticle solution to start the aggregation. The aggregation is monitored via extinction spectroscopy (Figure 6.4) and stopped after 9 s by adding 10 μl agrose, which freezes the aggregation. This is confirmed in the extinction spectrum. Instead of a broad red-shifting shoulder that appears in the case of larger growing aggregates the dimer peak does not shift further over time. The solution is then drop-cast on a glass cover slip.

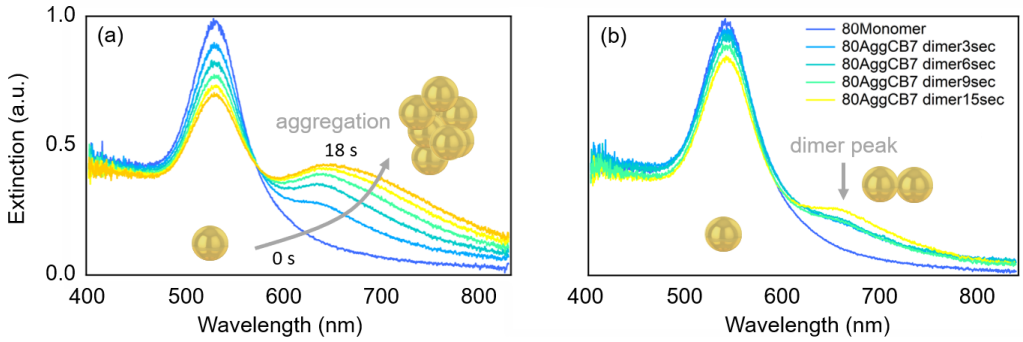

Figure 6.4: **Nanoparticle Dimer Fabrication with CB aggregation.** (a) Extinction spectra of gold aggregating nanoparticles in solution. During aggregation the single nanoparticle peak at 530 nm drops and an additional shoulder arises, shifting towards higher wavelength indicating larger aggregates. (b) Extinction spectra of stopped aggregation. The mode position of the dimer peak is preserved over time.

This method yields $\sim$ 30% dimers with a reliable gap of 0.9 nm. To distinguish between single nanoparticles and dimers, polarization scans are carried out[158]. The typical polarization signature of a 80 nm nanoparticle dimer is shown in (Figure 6.5 a), with a sinusoidal scattering response depending on incident polarization angle.

The optical response of plasmonic dimers and the NPoM geometry are approximately interchangeable, with equivalent field enhancement in the enclosed gap (Figure 4.3). However, there are some differences in the cavity morphology. From studies summarized in section 4.3 it is evident that the edge rounding at the cavity facet can modify the optical response drastically[66,115]. For the NPoM system the edge rounding of the bottom facet facing the substrate dominates the scattering response. The plasmonic dimer cavity

is formed by two facets roughly facing each other[125]. For narrow gap systems $d \leq 1$ nm the different alignment of the dimer facets may lead to higher spatial confinement of the electrical field and an alteration of charge screening in the gap region[123].

Laser Irradiation of Dimers

A representative example of an irradiated nanoparticle dimer is shown in Figure 6.5. The laser power is ramped from 0 to 2 mW in steps of 25 μW at the sample (Figure 6.5 b). Dark-field scattering spectra are recorded simultaneously, with a long pass filter to block out the laser light. Spectra are taken with an integration time of 100 ms.

Overall, the reconstruction process of the nanoparticle dimer shows a large resemblance to the previously discussed NPoM construct. For low laser powers an initial red shift of the dimer mode is seen, typical for facet growth (Figure 6.5 b: Stage I). The response of this mode first increases as the facet starts growing and then decreases for larger facets. At higher laser powers the red shift rate starts to slow down and is followed by a rapid blue shift at a laser power threshold (Stage II). Depending on the individual dimer multiple blue shifts progressively occur during stage II. The number of blue shifting modes largely depends on the final facet size as well as the precise morphology of the gap. A similar anti-crossing behavior as described in section 6.1.2 marks the different phases of the conductive bridging[159,160]. The bridging modes all show comparably narrow linewidths and low scattering strength, suggesting lower coupling efficiencies to the far-field, and tight confinement.

The final irradiation stage (Stage III) is accompanied by the appearance of a high intensity mode approaching from the far infra-red region. This mode increases in intensity as it shifts towards visible wavelengths. Reaching the spectral region close to the initial dimer mode the mode slows down and finally stops shifting all together. Higher laser powers do not initiate further blue or red shifts. Instead, the system remains rather stable at a final wavelength λ_f. At this stage the bridge diameter b reaches diameters on the order of the facet width w. Irradiating many different nanoparticles gives a very consistent behaviour. In contrast to constant laser power irradiation, the slow increase in power shows very reproducible trends suggesting a type of annealing process during irradiation. The growth always starts with an initial facet growth during stage I where it is followed by multiple rapid blue shifts in stage II. The final stage III is initiated with a single mode shifting into the visible region from the infra-red. This mode gains intensity as it reaches its final position, which is always close to the initial dimer mode position, where it stabilizes despite increasing laser power. The three most common irradiation occurrences are shown in the different rows in Figure 6.6. The first row shows bridged dimers with a single anti-crossing and the final stage is reached at laser powers of 0.25 mW. The second row illustrates irradiated dimers with two blue-shifting modes and a slightly higher final laser power threshold of of 0.30 mW. The last row

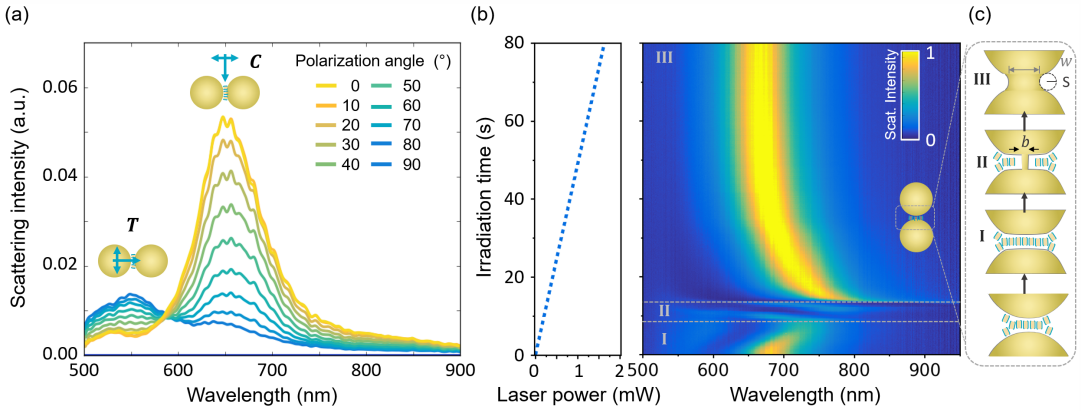

Figure 6.5: **Irradiation of a typical nanoparticle dimer with CB[7] as "soft spacer"** (a) Polarization dependent dark-field scattering spectra revealing the orientation of the dimer axis. (b) Subsequent dark-field scattering spectra during irradiation as a function of laser power shown to the right. (c) Schematic illustration of growth stages (I,II and III) during irradiation. All experimental data was collected using the costum build dark-field microscope.

shows the extreme cases of many simultaneous blue and red-shifts, and here the final stage is not reached until approaching laser powers of almost 0.50 mW.

Extracting the dimer mode positions, the correlation between the final wavelength λ_f at which the system stabilizes and the initial wavelength λ_f is illustrated in Figure 6.7. Apart from minor variations, the final mode position either coincides precisely with the initial wavelength or remains slightly on the red side of λ_i. As demonstrated by the linear slope, larger starting wavelength yield equally larger final wavelengths (Figure 6.7). The termination of the growth dynamics suggests that a final equilibrium state is reached, where further re-construction is energetically unfavourable.

In contrast to dimers in the non-touching regime, where the charge is accumulated in the gap, for bridged dimers the charges pile up within the anti wedge formed at the junction. Romero et al. show that wider wedge angles and therefore smoother junctions are found to cause an increase in linewidth and blue shift of the dimer mode[111]. In this configuration the wedge is assumed as smooth (rounded). However, the curvature of the cusp and therefore rounding effects as well as the sharpness of the edges are expected to highly impact the spectral response. As shown in[125] the rounding of the cusp leads to a read-shift in the spectral response. The experimental data suggests that the final mode position of the irradiated dimer highly depends on its initial state. However, the final spectral response is not only determined by the ratio of the nanoparticle diameter to the final facet width w, which limits the bridge diameter b but also by the wedge angle β and the roundness of the junction. Here, three different scenarios offer plausible explanation of the underlying mechanism (Figure 6.8). Assuming a constant gap distance g fixed by the molecular spacer (0.9 nm for CB[7]) and a given nanoparticle size the

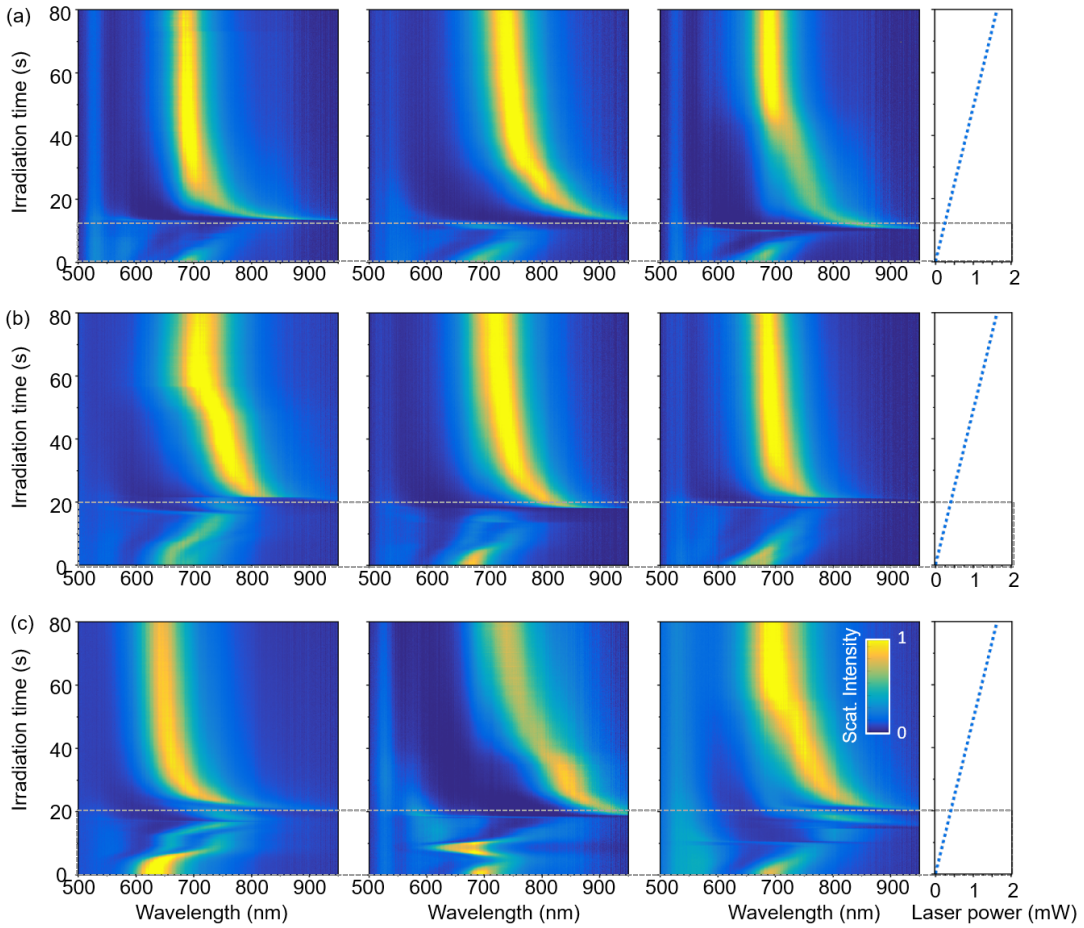

Figure 6.6: **Typical examples of irradiated nanoparticle dimers.** Subsequent dark-field scattering spectra of the nanoparticle dimer system as a function of laser irradiation, shown at the left hand side. Most common irradiation signatures: (a) a single blue shift initiating the conductive bridging at a laser power of 25 mW (b) two rapid blue-shift ending in the final stage *III* at ∼0.3 mW and (c) multiple spectral shifts terminated at a laser power of 50 mW.

initial wavelength λ_i is determined by the facet width to nanoparticle diameter ratio d/w. Larger facet sizes yield a red-shifted spectral response (Figure 6.8 a). This trend is further complicated when considering unequal facet sizes or facets facing each other with an angle rather than plan parallel[123]. Here the mode position is given by an effective facet width as a combination of both facets[123]. During irradiation the marooned bridge diameter b is given by the irradiation time. If the bridge always only grows to a certain diameter until reaching the final state - normally less than facet width - than the final wavelength position λ_f is determined by wedge angle β of the the marooned bridge in the middle. In the case of larger facets (Figure 6.8 a) the wedge angle β is small as the ratio of $b/w \ll 1$ and the bridge is highly marooned. In contrast for smaller facet diameters (smaller λ_i) the bridge fills the entire gap $b/w \sim 1$ yielding larger wedge angles that shift the finale wavelength λ_f to the blue (Figure 6.8 b). The wedge angle is even

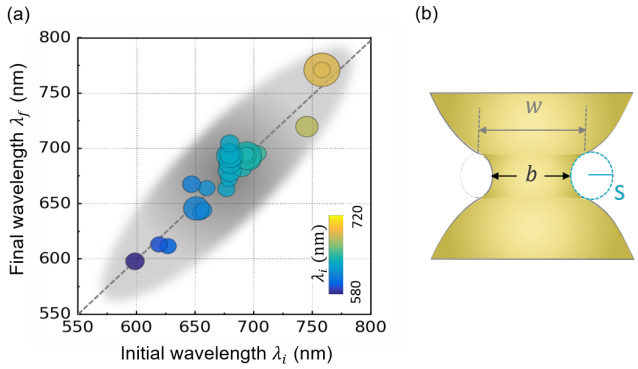

Figure 6.7: **Extracted dimer mode positions.** (a) Final equilibrium dimer mode position λ_f as a function of initial resonance wavelength λ_i. Black dashed line marks the diagonal $\lambda_f = \lambda_i$. The increase in scattering amplitude is reflected in the marker color. (b) Schematic of the dominant parameters determining the final equilibrium dimer mode position: a combination of the facet size w, the subsequent bridge diameter b and wedge angle defined by the rounding parameter s at the dimer junction

further increased for asymmetric dimers such as non-parallel facets facing each other, nanoparticle with an offset in respect to the dimer axis or a facet facing an edge (Figure 6.8 c). Thus, larger facets with larger λ_i yield smaller wedge angles β with larger λ_f and smaller facets or asymmetric dimers with smaller λ_i yield larger β with smaller λ_f.

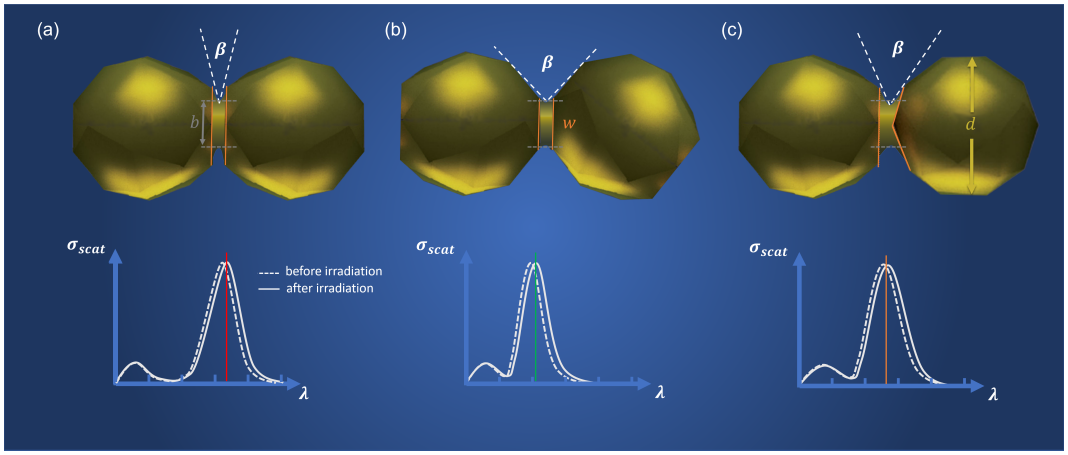

Figure 6.8: **Growth mechanisms** Schematic of the dominant parameters determining the final equilibrium dimer mode position: a combination of the facet size w, the subsequent bridge diameter b and wedge angle β at the dimer junction. (a) Large initial facets yield small wedge angle β at the dimer junction with λ_i and λ_f red-shifted. (b) Small initial facets yield large β as the bridge fills the entire facet with λ_i and λ_f blue-shifted. (c) Asymmetric facets either with facets facing each other non-parallel or and edge facing a facet yield larg β.

However, to identify the exact growth dynamics and assign the observed spectral shifts to a theoretical model, further investigation is needed. In particular the studying the power dynamics with nanoparticle size and gap distance is crucial in understanding the

underlying driving forces. Furthermore, exploiting the plasmon enhancement resonant tuning is expected to be very promising.

6.2 Conclusion

In the persuit of ever increasing field enhancement, plasmonic cavities are slowly reaching the quantum regime with sub-nm gaps where local effects and tunnelling play an important role. Using laser-induced tuning to modify and monitor plasmonic cavities in a feedback loop two regimes were identified as the gap closes: the non-conductive regime and the conductive bridging regime. In the first regime hard spacer materials are used to prevent contact between the nanoparticle and the substrate, limiting the growth dynamics to facet growth. Increasing the facet width allows active tuning of the optical cavity modes accompanied by large field enhancements and small mode volumes. Polarization dependent dark-field scattering is used to identify the facet eccentricity and monitor the growth uniformity during irradiation. In contrast soft spacers materials are penetrable and allow the formation and growth of thin conductive filaments shorting the gap. In this case the optical response changes drastically and the field enhancement in the gap region drops off dramatically as conductive bridges form in the centre of the facet, expelling the field to the edges of the facet[133]. Changes in the optical response can be understood within the metal-insulator-metal waveguide model, where the geometrical change in the the groove cavity length determines the new resonance positions. Using nanoparticle dimers as a model system, consistent growth dynamics as a function of laser power are found. The growth process is initialized by a facet growth stage accompanied by red shifts, while at a second stage this process is overpowered by the formation of a conductive bridge in the gap region. Finally it terminates in an equilibrium state determined by a combination of the facet size, the subsequent bridge diameter and wedge angle at the dimer junction. This provides new information on the surface tension and wetting of noble metals on the nanoscale.

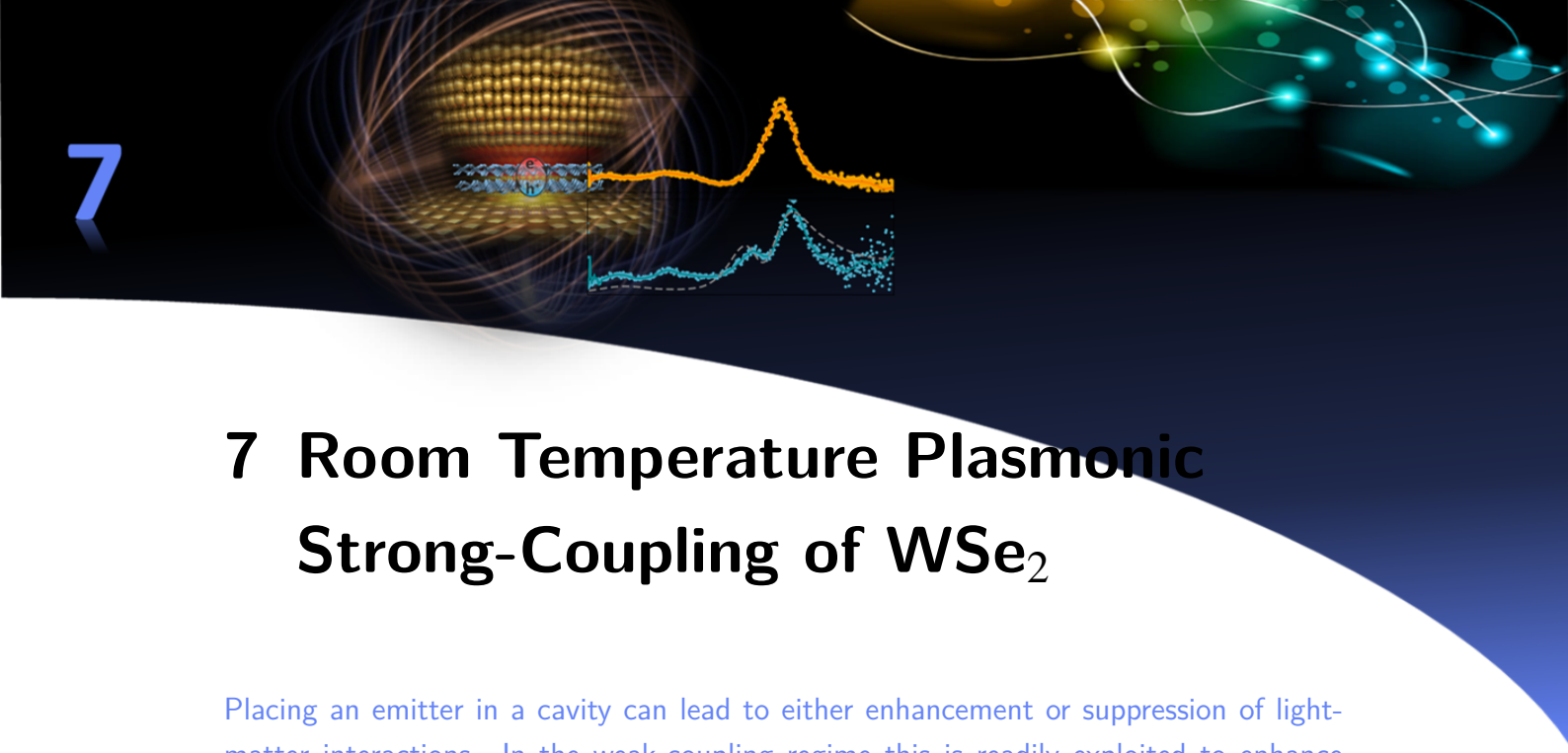

7 Room Temperature Plasmonic Strong-Coupling of WSe_2

Placing an emitter in a cavity can lead to either enhancement or suppression of light-matter interactions. In the weak-coupling regime this is readily exploited to enhance emission from single emitters[21,26,31,33,161–166] but more pronounced effects emerge in the strong-coupling regime, where new mixed states are formed that are highly entangled and give rise to attractive quantum phenomena, such as polariton lasing, Bose-Einstein condensation and all-optical low power switching[58,167–173]. So far all of these phenomena are restricted to cryogenic temperatures. However, 2D materials offer a realistic perspective for exciton devices at room temperature.

While previous chapters mainly discussed the plasmonic aspect of nano-cavities formed by the NPoM construct, this chapter shows a promising example of incorporating Transition Metal Dichalcogenide (TMD) materials in plasmonic cavities to achieve room-temperature strong coupling.
A brief overview on current state of the art examples of room-temperature strong-coupling reviews key requirements in that regime. Furthermore, the unique properties of TMD materials and their stable excitons at room temperature with high oscillator strength are discussed.
After summarising the assembly of WSe_2 NPoM constructs, it is shown how ultra violet (UV) laser irradiation is used to carefully tune the plasmonic modes of the nano-cavity and allow for optimal coupling of the emitters to the cavity. Simulating the different field distributions in the plasmonic cavities and employing different numbers of TMD layers, the importance of emitter alignment is explored. Incorporating WSe_2 multilayers of greater than N_L =7 layers, clear spectral anti-crossings are resolved with Rabi-splittings exceeding 135 meV. Analysing the power dependent photoluminescence (PL) emission of the bare TMD flakes compared to strongly coupled flakes clearly indicates non-linear emission [1].

[1] Parts of this chapter have been previously published in reference[72].Simulations were carried out by Rohit Chikkaraddy, PL measurements were carried out together with Will Deacon and AFM measurements with Dean Kos

7.1 Reaching the Strong-Coupling Regime

As described in section 2.1.3.3, in the strong coupling regime light and matter becomes strongly entangled and new states are formed. These states can neither be described as light or matter, but mixed states, where the energy oscillates continuously between both systems. In this regime coherent phenomena play an important role, giving rise to attractive new physics, such as stimulated emission, gain and polariton lasing[31]. Furthermore, it allows the exploration of Bose-Einstein condensation[168,174] which opens up the route to quantum information technologies and allows one to modify the electromagnetic environment of an emitter.

In order to reach the strong coupling regime, the light-matter coupling needs to over-

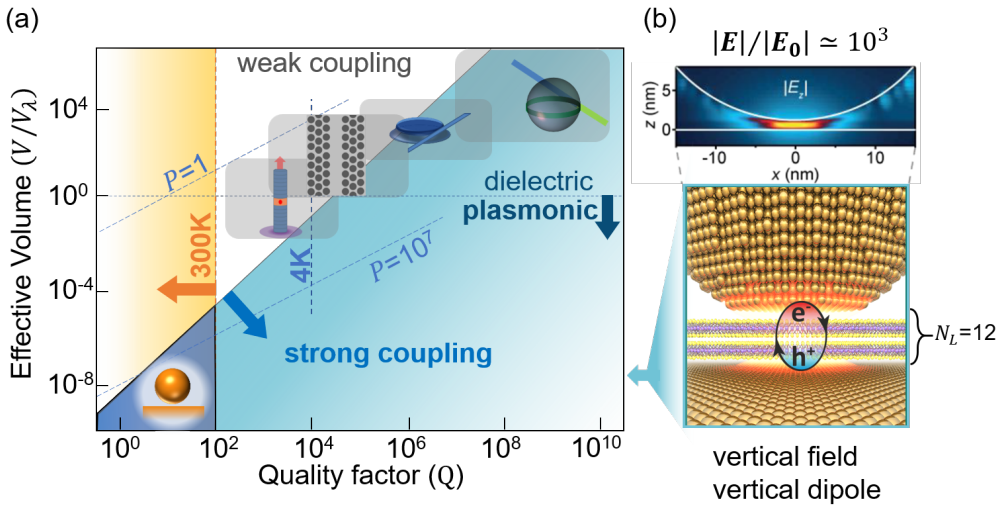

Figure 7.1: **Figure of merit to reach the strong coupling regime** (a) Different optical cavities (right to left: NPoM, micropillars, phonotic crystals, microdisks and whispering gallery spheres) are ranked according to their quality factor Q and effective mode volume V/V_λ. The dark blue corner at the bottom left side indicates the regime where the mode volume is small enough to reach strong coupling at room temperatures (orange area). Purcell enhancement factors P are indicated with dashed lines. (b) Typical field enhancement (top) of a NPoM cavity construct depicted schematically in the bottom with WSe_2 incorporated in the cavity. Adapted and modified from[21]

come the losses of the system. If this is the case then the energy between the cavity and the emitter can cycle back and forth, before being lost due to non-radiative channels of the emitter or leakage of the cavity. The losses due to the emitter dissipation γ are highly temperature dependent and can therefore be reduced at low temperatures. The losses of the cavity κ can be reduced by increasing the quality factor Q. For cryogenic temperatures, the emitter scattering is suppressed and high-quality dielectric cavities are used to boost interaction times and enhance coupling strengths (Figure 7.1 blue area). High $Q \propto \kappa^{-1}$-values, typically requires the use of large cavities such as photonic crys-

tals, microcavities or even whispering gallery modes (Figure 7.1 inset). In these systems, the volume of interaction is large and involves the coupling of many emitters at the same time. Conventional solid state materials such as GaAs, CdTe show Rabi-splittings of the order of 1-10 meV at 10K[174], whereas Bose-Einstein condensation in GaN and ZnO was shown to work at room temperature. On the other hand, most traditional III-V GaAs-based heterostructures posses excitons that ionize at 300K and are therefore only feasible at cryogenic temperatures. The development of realistic excitonic devices functioning at room temperature is highly desirable[175] and requires materials with stable excitons, where exciton binding energies are on the order of thermal energies: $E_b \geq k_b T$. The recently emerged group of two-dimensional (2D) van der Waals materials with exciton binding energies as high as 500 meV[50] are extremely promising candidates. They have attracted a lot of attention during the past decade, due to their unique electronic, mechanical, optical and thermal properties, which are described in more detail in section 2.2,. Vertically-stacked, atomically thin semiconductor TMDs, such as MoS_2 and WSe_2 have strong excitons in the visible and near-infrared (near-IR) with spin-selective excitation into K, K' valleys[176,177], where the spin-selective properties are expected to add valley-controlled functionalities to the strong coupling regime[178].
Furthermore, drastic changes in their properties are expected with increasing number of stacked layers[45,46,52]. A well documented example is the transition from a direct bandgap in MoS_2 and WSe_2, producing strong exciton PL to an indirect bandgap where the PL is suppressed as soon as $N_L \geq 1$[49,51]. It is therefore expected that layers must be spaced separately rather than using multi stacks (for instance with hBN[179]) to retain efficient emission, increasing the cavity volumes and reducing their Rabi coupling. The following section gives a brief overview of the latest developments using 2D materials to achieve room temperature excitonic devices, and addresses the different challenges to overcome.

7.2 Strong Coupling with 2D Atomic Crystals

First promising examples exploring TMDs to achieve strong coupling used optical resonators based on dielectric or metal mirrors. These are mostly assisted by cryogenic cooling of monolayer samples[161,179] where splittings are resolved on the order of $E \geq k_B T$. The use of optical microcavities involves complicated setups which are inherently limited by the diffraction limit, thus resulting in mode volumes on the order of optical wavelength (with minimum volume $V_{min} \approx (\lambda/n)^3$ and refractive index n). Therefore, they couple to many excitons at the same time, requiring very high quality van der Waals monolayers with little disorder. However, at room temperature, spectral line splitting is

barely resolved and on the order of thermal energies[180–183].
Using plasmonic cavities, splittings greater than 100 meV are necessary to exceed the plasmon damping of approximately 90 meV at room temperature. To significantly improve light-matter interactions, cavities with very low mode volumes are needed as $g \propto 1/\sqrt{V}$.
At the same time reducing the size of the cavity to the nanoscale leads to an increase in the electrical field strength, which is expected to result in enhanced light-matter interactions, with strong nonlinearities, large photon forces and enhanced emission and absorption probabilities[171,172].

Room Temperature Strong-Coupling Using Plasmonic Cavities

The prospect of ultra-small mode volumes, way below the diffraction limit and high field enhancement of plasmonic cavities as well as the unique properties of TMDs have triggered interest in plasmon-exciton coupling in 2D materials. Very recent examples of room temperature strong coupling with 2D monolayers are shown in Figure 7.2. Using single plasmonic nanoparticles such as triangles[184] and rods[185,186], Rabi-splittings of 101 meV were achieved. In the case of silver nanorods[185] the field is polarized along the axis of the rod, allowing for parallel alignment of the emitter dipole and field orientation. In that configuration, mode volumes of around 1.92×10^3 nm^3 can be achieved, still coupling to many emitters. However, changing the aspect ratio of the rods reduces the mode volume to 230 nm^3[185], allowing the selective coupling to $\sim$5 excitons[185].
Despite major advances in the field of plasmonic strong coupling, clear proof of reaching the strong coupling regime is still highly debated. A dip in the scattering spectra is not enough to confidently identify the strong coupling regime. In fact, other effects such as exciton induced transparency and absorption may show similar features[187].A clear indication of the strong coupling regime is the anti-crossing of the spectra lines with detuning of the exciton and cavity resonance. Since the excitons in molecules or semiconductors have specific resonances, the cavity resonance needs to be actively tuned to show anti-crossings and allow for optimal coupling. Having the means to actively tune the plasmonic cavity system without complex fabrication processes thus is highly desirable[188].

While microcavities can easily be tuned by changing the incident angle or cavity length, this is challenging at the nanoscale. For example single nanoparticle structures have precise resonances according to their size, shape and dielectric environment as discussed in detail in section 2.1.2.4. Therefore, changing the plasmon resonance involves changing the actual nanostructure and is fabrication intensive. Once the fabrication step is terminated, the plasmon resonance is fixed in most cases and cannot be tuned in-situ. Different attempts showing the emission properties with different detunings of the plasmon and emitter resonance require cycling back and forth between fabrication and

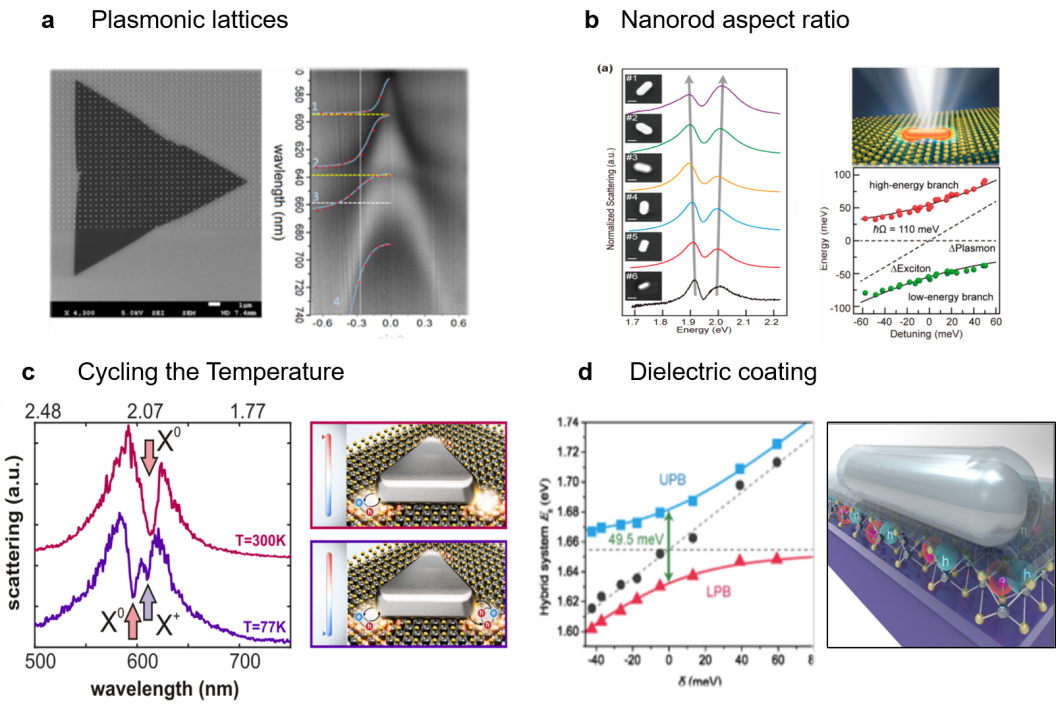

Figure 7.2: **Examples of monolayer TMD strong coupling using plasmonic field enhancement** (a) Detuning of plasmon-exciton strong coupling in plasmonic lattices using angle resolved reflectance measurements at 77 K. (b) Nanorods with different aspect ratios to show plasmon-exciton dispersion, achieving Rabi-splitting up to 91 meV at room temperature. (c) Observation of tunable charged exciton polaritons with temperature using silver nanoprisms. (d) Dielectric tuning of plasmon-exciton dispersion using Al_2O_3 coated silver nanorods. Figures taken from [183–186] respectively

characterization[186]. Coating silver nanorods with different layers of Al_2O_3 and therefore changing the dielectric environment, Zheng et al. demonstrate tuning of the plasmon resonance up to 90 nm (Figure 7.2 d). However, this process is very time consuming and relies on relocating the same nanostructure. It also does not allow in-situ active detuning of the system. Similar to that approach Wen et al.[185] used gold nanorods with different aspect ratios to show the characteristic anti-crossing signature of the strongly coupled system. This involves many different nanoparticles, which may vary in size and aspect ratio and therefore are hard to compare. The different aspect ratio changes the modes and the related mode volume making this approach less comparable. An alternative is provided by plasmonic lattices. Liu et al.[183] demonstrated strong exciton-plasmon coupling in silver nanodisk arrays with an integrated layer of MoS_2 (Figure 7.2 a). The use of a plasmonic array allows them to tune the plasmon resonance by changing the incident angle. Nonetheless, the use of a plasmonic array leads to the excitation of lattice resonances that couple to localized surface plasmon resonances and therefore lead to inhomogeneous broadening as well as very large mode volumes. For many of the key features in the quantum limit, small numbers of coupled emitters are needed and therefore small mode volumes are preferred.

To push the boundaries of plasmon-exciton interactions to the single-emitter level usually complex nanostructures with fabrication expensive architectures are needed[162]. In that case plasmonic coupled structures are very promising[21] due to their scalable small mode volumes as well as their controlled fabrication using electron-beam lithography. Furthermore, they allow polarization selective coupling to the emitter placed in the gap. Nonetheless the limiting factors here remain high fabrication costs and precision as described in detail in section 4.1. A simple alternative is give by the NPoM plasmonic cavities which can be easily fabricated using self-assembly.
In previous work Chikkaraddy et al. showed that using the nanoparticle on mirror system, mode volumes as small as 40 nm^3 can be achieved and in the extreme case of picocavities even 1 nm^3. By overcoming the typical losses of a scattering emitter at room temperature (k_bT) strong coupling down to the single-molecule level was resolved[21]. In this regime, excitons with oscillator strength f give Rabi splitting $\Omega_R \propto \sqrt{(fN_Ln/\lambda^3)}$. However, in such extreme plasmonic cavities the resonant optical field is typically polarised perpendicularly to the layer plane[110,116] and hence poorly coupled to the TMD exciton dipole oriented in-plane[189] (see below). This suggests that strong coupling of TMDs in plasmonic cavities is problematic, in comparison to systems with dipoles oriented out-of-plane[163,190–192]. Therefore, for a successful assembly of plasmonic TMD devices, the field alignment as well as the emitter orientation has to be carefully considered.

7.3 Fabrication and Characterization of WSe_2 NPoM constructs

In the following section the fabrication of the NPoM constructs will be briefly summarized. The exact structure of the sample is characterized by AFM and Raman spectroscopy. Dark-field microscopy in combination with simulations are used to analyse the individual NPoM constructs.

Fabrication of WSe_2 incorporated NPoM constructs

The self-assembled plasmonic cavities are fabricated on multilayer flakes of WSe_2 as described in section 3.3.3. The latter were fabricated by Evgeny Alexeev at the University of Sheffield. Using bulk crystals, single and multilayer flakes of WSe_2 were exfoliated onto a silicon substrate and then transferred onto template-stripped Au substrates. To ensure the detection of individual constructs and to prevent cross-talk between the individual NPoM systems, nanoparticles are assembled with a low density with spacings of

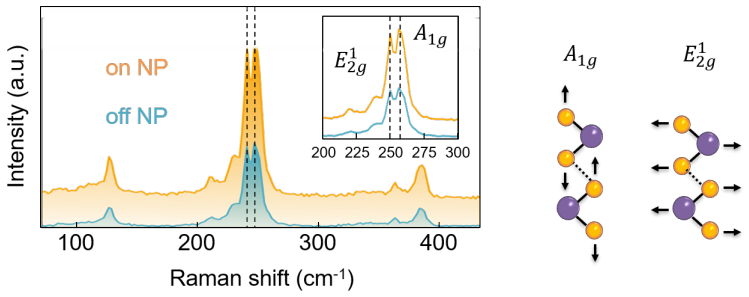

Figure 7.3: **Surface-enhanced Raman spectrum of mulitlayers of WSe_2** The orange and blue line show the SERS spectra of bare WSe_2 flakes on gold substrate and incorporated in a NPoM construct respectively. The inset shows the characteristic vibrational modes at 250 and 257 cm^{-1} depicted on the right-hand side. Pump laser at 633 nm with laser power of 24 μW and focussed to a spot size of $\approx$1.2 μm

$>$5 μm separating them. A major difficulty of the fabrication of plasmonic nanocavities with WSe_2 is the reliable control of the structure. While thicker multilayer flakes can be easily identified using optical brightfield microscopy (Figure 7.5) thinner flakes $N_L \leq 3$ are transparent in the visible and therefore hard to locate on the sample. To ensure the presence of WSe_2 in the plasmonic nanocavities surface-enhanced Raman scattering (SERS) measurements were carried out. The power of the 633 nm CW laser was attenuated to $\leq$24 μW at the sample to prevent damage. In agreement with literature[51], 2 peaks at 250 cm^{-1} and 257 cm^{-1} corresponding to the E^1_{2g} and A_{1g} vibrational modes (Figure 7.3 b) can be identified. The Raman modes are drastically enhanced when incorporated in the NPoM cavity due to the field enhancement (orange). Estimating the laser spot size as 1.2 μm and the plasmonic cavity volume as 40 nm^3, suggests a local field enhancement of 5000 in comparison to the bare flake (blue).

A second problem presented is related to the initial tuning of the different plasmon modes in nanometre-scale gap cavities. While smaller gaps d between the nanoparticle and its underlying mirror result in tighter plasmonic confinement ($V \propto d^2$D for nanoparticles of diameter D), they also lead to a detuning of the cavity mode and the exciton red-tuning rapidly to the infrared. This problem has been known for cube nanoparticle geometries coupled to semiconductor quantum dots[33] or MoS_2[38]. To tune the modes to the visible range, gaps d of the of order 10 nm were used.

Here, the gap size is balanced with the TMD refractive index and spherical nanoparticles of different diameters are used to achieve optimal strong coupling conditions. Therefore, in order to match the plasmon resonance of the coupled system to the exciton resonance of the WSe_2, different nanoparticle sizes varying from D=60-100 nm were drop-cast onto the flakes. As discussed in section 4.3, the coupled plasmon resonance shifts to higher wavelength and faceting effects become more important with increasing nanoparticle size. For NPoMs with a size of D=100 nm, the dominant coupled plasmon

resonance λ_p in the system is beyond 700 nm (Figure 7.4 c); resonances at shorter wavelengths correspond to transverse and quadrupole modes with weaker field confinement and enhancements[126].

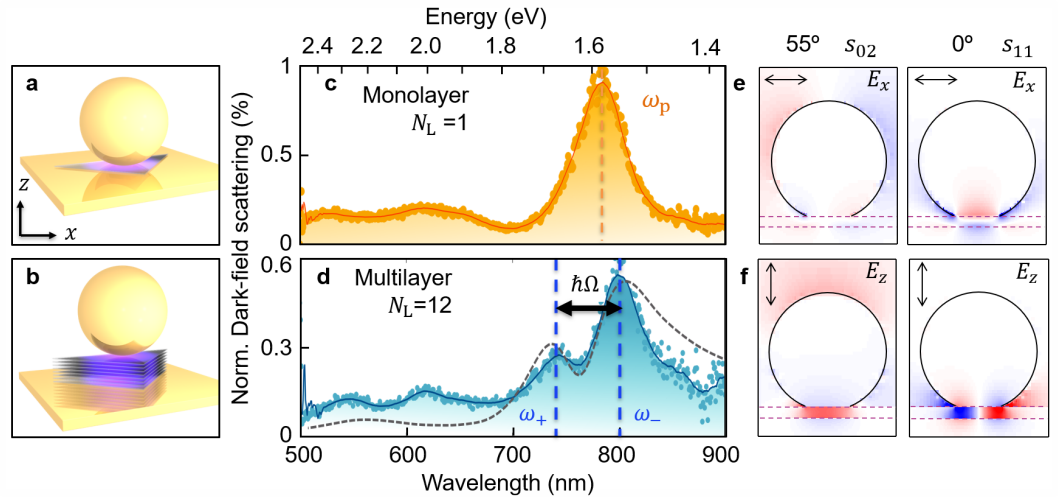

Figure 7.4: **Optical signature of single and multilayer WSe_2 embedded in plasmonic nanocavities** (a,b) Schematic of nanoparticle-on-mirror cavity encapsulating WSe_2 flakes for N_L=1,8. (c,d) Dark-field scattering spectrum of individual NPoMs showing a single plasmon peak for N_L=1, but a mode splitting due to strong coupling for multilayer N_L=12, reproduced by FDTD simulations (dashed line). (e,f) Simulated field distributions $E_(x,z)$ for two plasmon coupled modes (s_{02}, s_{11}) at λ=780 nm with high refractive index material (dashed, n=2.8) in the 10 nm gap. Angles of incidence 55 degrees (left) and 0 degree (right); red-blue colour-scale shows field enhancements of $\pm$30 $|E_0|$.

Characterization of WSe_2 NPoM Constructs

The optical response of the coupled system is measured by dark-field spectroscopy. In the case of a single monolayer incorporated in the nanocavities, field enhancements up to $|E|/|E_0| \approx 70$ should yield Purcell factors sufficient to produce strong coupling, which should result in a mode splitting in the characteristic cavity mode[182].

However, scattering spectra of MoS_2 or WSe_2 monolayers in such nanogaps, exhibit only a single mode around 800 nm indicating weak coupling and enhanced photoluminescence (Figure 7.8 top, 7.4 c). In contrast, incorporating thicker WSe_2 flakes (Figure 7.7 bottom, 7.4 d), results in a clear mode splitting suggesting strong coupling. The splitting of both peaks ω_+ and ω_- exceeds 140 meV in agreement with FTDT simulations (grey dashed line). Carrying out atomic force microscopy (AFM) measurement (Figure7.5 e) the thickness of the flake was determined as 10 nm which corresponds to $N_L = 12$ WSe_2 layers. The difference in the emission characteristic can also be seen in the dark-field image. While the nanoparticles on the flake appear as red dots in Figure7.5 c) arising from infrared plasmonic modes, the NPoM constructs off the flake appear green due to the coupled modes of very small gaps. The small gap is caused by the $\sim$ 1 nm citrate layer that surrounds the nanoparticles to prevent their aggregation. The refractive index

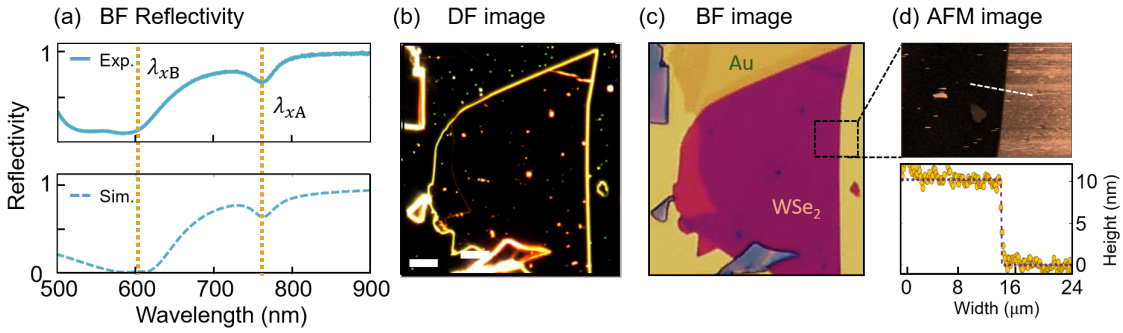

Figure 7.5: **WSe_2 stack properties** (a) Experimental (top) and simulated (bottom) Reflectivity of multilayer flake shown in (b), with A and B exciton indicated by orange dashed line. The multilayer stack is deposited on a gold substrate and the measurements are carried out away from the nanoparticles. Dark-field (b), Bright-field (c), and AFM (d) images of multilayer WSe_2 stack with 10 μm scale bar (solid white line). AFM height profile of flake edge (white dashed line) gives d=10±0.4 nm, corresponding to 12 layers.

of the WSe_2 flake can be extracted by bright-field reflectivity spectra. These spectra show two minima (Figure 7.5 a) that correspond to the A and B excitons at 761 nm and 605 nm respectively[51,176,177,193,194]. The appearance of these peaks at ambient temperatures confirms the room temperature stability of the excitons due to their large exciton binding energies. The high absorption below 600 nm is explained by interband transitions of the Au substrate, as well as the much larger C-exciton TMD absorption.

Bandstructure transition of WSe_2

Many TMDs undergo a transition from direct to indirect band gaps when increasing the number of layers from single to multi layer systems[51]. When increasing the number of layers, changes in the band structure (Figure 7.6 a) lead to competing relaxation processes. The change in band structure with number of layers is indicated with orange and blue bands for the multilayer and monolayer case respectively. The direct band gap transition in a monolayer takes place at the edge of the Brillouin zone at the degenerate K, K points (blue arrow). With increasing layer numbers, the blue-shift of the valence band at the Γ-point results in additional competing indirect transitions, arising from intervalley scattering across Λ - Γ and phonon-assisted transitions across K -Γ. Several factors affect the ratio of direct to indirect transitions and the band structure of TMDs can be engineered by temperature[51,195] or strain[60,196]. Strain and temperature increase the interlayer spacing and decrease the interlayer interactions due to thermal expansion, which dominates along the out-of-plane c-axis.[176,177]. For high temperatures ($\sim$ 300K) this leads to an isolation of the individual layers and reduces the coupling of each layer in the stack[51], therefore increasing the direct transition.

Furthermore, the direct and indirect transition are well separated from each other due to the large blue-shift of the transition at the Γ- point to lower energies.[51]. The K - K'

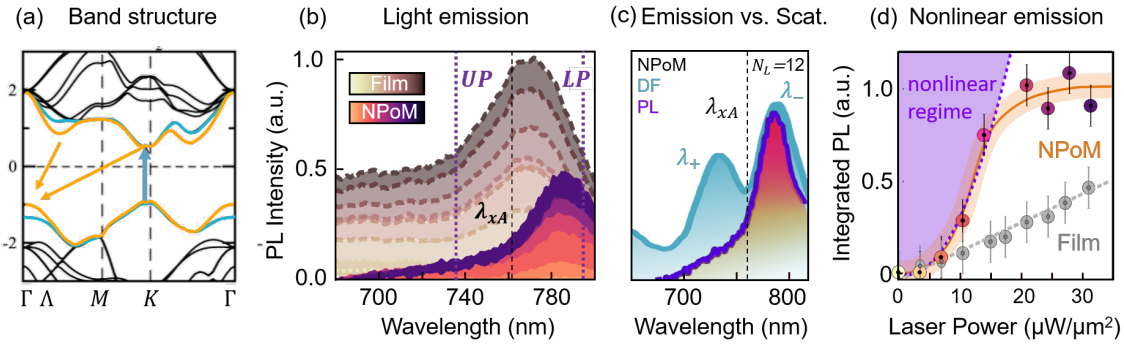

Figure 7.6: **Emission properties of WSe_2 stack** (a) Transition of mono- (blue) to multilayer (orange) of WSe_2 band structure. Competing indirect transition Λ - Γ and K -Γ appear for $N_L \geq 2$ (orange arrows). (b) Power-dependent Photoemission (PL,Input power ranges from 0-30 μWμ m$^{(-2)}$ in steps of 2.5 μW) at room temperature of the multilayer stack (brown) and NPoM (purple). Vertical lines mark the A exciton absorption peak (black) and polariton peaks (purple). (c) Scattering and PL spectra on the same NPoM, the dashed line marks the exciton absorption peak. (d) Scaling of integrated emission intensity with pump power for polaritons in NPoM (orange curve) (background subtracted) and excitons in multilayer on Au substrate (grey). Error bars result from power fluctuations and spatial drifts. The purple shading indicates the nonlinear emission regime. Figure modified from [197]

transition requires an energy of 1.63 eV, while the Γ-K transition energy is significantly lower (1.4 eV). In the case of the bare flake this leads to an increase in the broad phonon assisted emission and a decrease of the direct A exciton emission with number of layers as shown by Zhao et al.[51]. Nonetheless, tuning the plasmon mode into resonance with the direct A exciton allows the selective enhancement of the K- K recombination rates, rebalancing the branching ratios. The large Purcell enhancement in the plasmonic cavity decreases the A exciton lifetime below its undressed radiative recombination time of approximately 200 fs[198]. As a result the A excitons emit before carriers can be scattered into the Γ, Λ valleys by phonon-assisted intervalley relaxation which typically occur on time scales of 30 fs at 300K[198].

Emission Properties of WSe_2 NPoM Constructs

The presence of emission from the direct transition is confirmed by looking at the PL of the bare flake compared to the emission when the flake is incorporated in the plasmonic cavity (Figure 7.6b). The PL is measured using a tuneable Titanium-doped Sapphire laser in combination with an optical parametric oscillator (OPO), which allows the tuning of the pump wavelength (for details see[199]). In order to avoid pumping the interband transitions of the Au substrate, the wavelength is tuned to 633 nm. This is achieved by two band pass filters that cut out the incident light before a grating monochromator used as a spectrometer. Very low powers ($\sim$nJ) are used to prevent laser damage on the sample.

The PL of the bare WSe_2 film with different laser power is shown in blue (Figure 7.6). In comparison, emission of the WSe_2 NPoM construct (after subtracting background emission from the surrounding film) is shifted to longer wavelengths. This becomes even more evident when comparing the PL with the DF scattering spectra of the same NPoM (Figure 7.6 c). The PL peak matches the the lower polariton energy visible in the DF scattering at 785 nm. As typical for strongly coupled systems, less emission is seen from the upper polariton branch, indicating a fast energy relaxation. When taking the relative emission strength on and off the NPoM into account, the PL enhancements exceeds a factor of 100, indicating the speedup of emission compared to non-radiative scattering (see FDTD simulations below). This confirms that the Purcell enhancement decreases the A exciton lifetime so that the re-emission from the A exciton happens before phonon scattering. A further indication is the shift of the NPoM PL to higher wavelength where the polariton emission is expected. Neither exciton nor polariton lines are observed to spectrally shift with increasing laser power. However, light intensities of the NPoM increases superlinearly, compared to the linear increase of the surrounding multilayer film (Figure 7.6 b), which provides a first indication of nonlinear polariton effects (Figure 7.6 d). The intensity saturation seen at higher powers has been previously attributed to exciton-exciton Auger processes[177].

It should be noted that the photoluminescence yield in such gaps is also enhanced off-resonance, while on resonance the yield increases up to a factor of 5. This becomes more evident when tuning the cavity system, which will be discussed in section 7.4. Furthermore, coupling efficiencies vary between the bulk emission and the flakes incorporated in the NPoM depending on the excitation angle. Coupling the laser through the centre of the objective results in low angle excitation which is polarized parallel to the substrate, which favours coupling to the bare flake. Therefore, for optimal coupling to the NPoM construct, high angles with laser polarization along the z axis are required.

7.4 Active Tuning and Evidence of Strong-Coupling

To characterize the reliability of the system, dark-field scattering of many individual NPoM constructs with N_L=12 layers of WSe_2 as a spacer material are measured (Figure 7.7 c). The typical double-peaked spectral features with a characteristic dip at the position of the A exciton is consistently present in all normalised scattering spectra, although changes in the morphology of the individual nanoparticles cause fluctuations in the peak height ratios due to variation in facet size as well as nanoparticle size[41]. The absence of Fano-like lineshapes, which would indicate exciton induced transparency and absorption, corroborate the strong coupling regime[200]. By contrast, WSe_2 monolayer

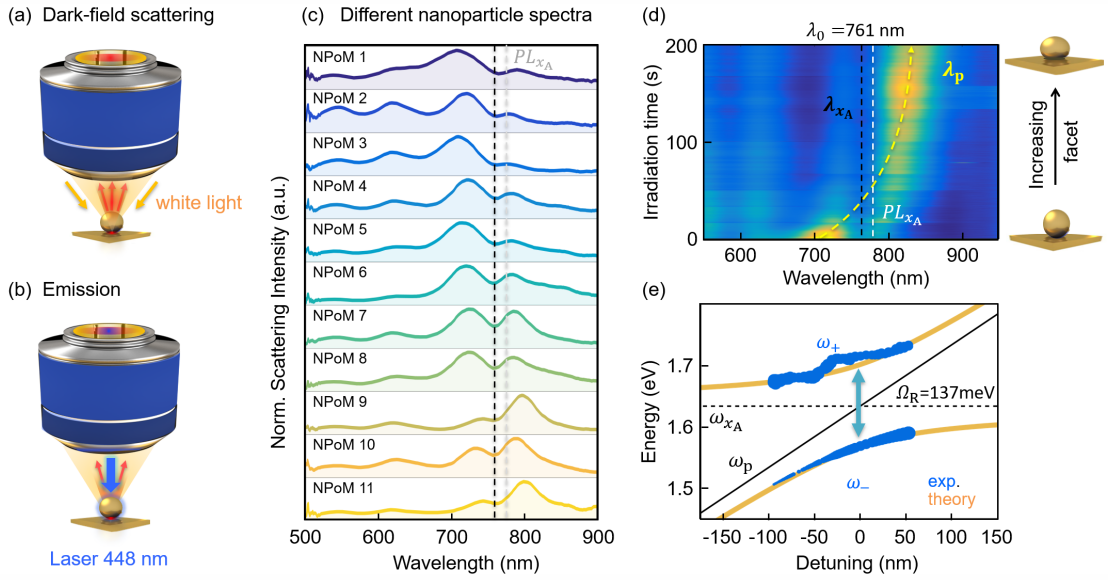

Figure 7.7: **Signature of strong coupling in individual NPoM constructs** (a) Schematic of white-light dark-field scattering and (b) PL/irradiation setups. (c) Normalized dark-field scattering spectra of individual NPoM constructs each with WSe_2 stack of N_L=12 monolayers. The black dashed line shows the A exciton position. (d,e) Laser-induced tuning of NPoM plasmon resonance via growth of lower facet, mapping out the anti-crossing around A exciton. (e) Hybrid plasmon-exciton branches (plexcitons, $\omega_\pm$) with Rabi-spitting of Ω_R=137 meV. Blue dots correspond to extracted experimental values and orange to coupled oscillator model.

constructs (N_L=1), with a scaled total oscillator strength and cavity volume, no such double-peaked spectra (Figure 7.4 c).

To unambiguously prove the strong coupling regime, the dispersive nature of the hybrid states need to be demonstrated. In the strongly coupled case, a clear anti-crossing of spectral lines with detuning is expected, while a crossing of spectral lines indicates the weak coupling regime. This detuning has been achieved by studying different NPoM geometries[185]. However, to demonstrate the anti-crossing for a single strongly coupled system, active control of the plasmonic cavity is needed to tune in-situ across resonance with the A exciton. To this end a blue 448 nm CW laser of 0.1 mW is used to irradiate the NPoM (see section 6 for details). This increases the mobility of gold atoms at the nanoparticle surface which move towards the bottom facet. The induced growth of the bottom facet red-shifts the plasmon resonance, ω_p, as previously studied[133]. As a robust spacer, the WSe_2 layers prevent any conductive bridging effects from NPs onto the bottom mirror, which has been observed for molecular spacers (see section 6 for more details). During the experiment the intactness of the NPoM constructs is verified by SERS and DF scattering spectra. When tuning the plasmon resonance over the A exciton, a clear anti-crossing is seen (Figure 7.7 d,e). Fitting a semi-classical

coupled oscillator model to the experimental data (as described in section 2.1.3), gives the simplified Jaynes Cummings picture[21,31] and tracks the plasmon resonance ω_p:

$$2\omega_{\pm} = (\omega_p + \omega_{xA}) \pm \sqrt{(\Omega_R^2 + \delta^2)}, \tag{7.1}$$

where $\delta = \omega_p - \omega_{xA}$ is the detuning and Ω_R the Rabi frequency. Each plasmon resonance position (black dashed line) is extracted from the two peak positions. The exciton energy is indicated with a black dashed line. At the point of zero detuning, a Rabi splitting Ω_R of 137 meV is extracted from the two hybrid plexciton branches. The Rabi splitting is found to be consistent for all NPoM systems on the same WSe_2 flake, where the cavity volume and oscillator strength are constant. Furthermore, the semi-classical oscillator model (orange, Figure 7.7c) shows good agreement with the experimental results (blue). Extracting the emitter losses γ_x=25 meV and cavity κ=90 meV from reflectivity measurements and dark-field scattering it is evident that for larger N_L the required strong coupling condition of $\Omega_R > (\gamma_x + \kappa)/2$ is fulfilled[31] . In comparison, Figure 7.8 (top) shows the detuning of a NPoM construct formed by a bilayer of WSe_2 where the strong coupling condition is not met. When incorporating monolayers and bilayers of WSe_2, larger NPs are used to match the plasmon resonance with the exciton. While a clear enhancement can be seen when the plasmon resonance coincides with the A exciton, there is no peak splitting in contrast to strongly coupled constructs formed by 12 monolayes of WSe_2 (Figure 7.8, bottom).

7.5 FDTD Simulations

Finite-difference time-domain (FDTD) simulations (described in section 3.2.1) were carried out with Rohit Chicarraddy to calculate the plasmonic modes and their mode volume V as well as the Purcell Factor:

$$F_P = 3/(4\pi^2)(\lambda_0/n)^3 Q/V. \tag{7.2}$$

It should be noted that the refractive index n of TMDs is highly anisotropic in-plane and out-of-plane due to their layered structure which affects the plasmon modes of the cavity system (as discussed in section 4.3). The large out-of-plane refractive index n_z=2.8,[193] red-shifts the lowest l_1 mode to $\lambda \approx 800$ nm even for large 10 nm gaps (Figure7.9 b). To characterize the NPoM cavity, the scattering response of the construct with multilayers of WSe_2 is simulated. The simulations are calculated for non-resonant n, neglecting the two exciton contribution. The result depicted in Figure 7.9 b) shows two different

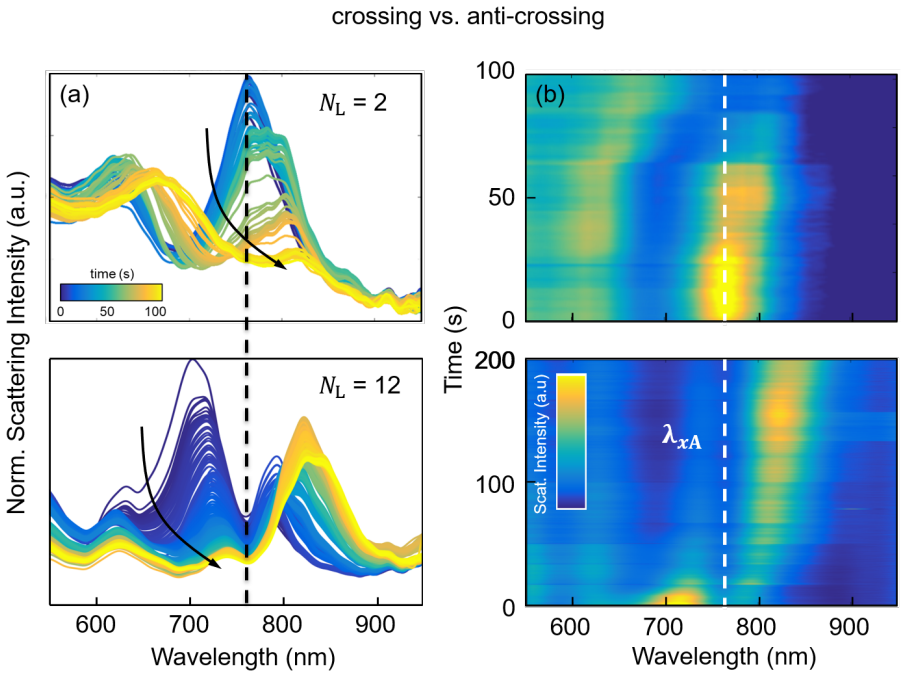

Figure 7.8: **Weak coupling vs. strong coupling regime** Tuning the plasmon resonance via laser-induced growth of the lower NPoM facet allows mapping out the dispersive nature of the coupled system. (a) Individual scattering spectra with increasing irradiation time showing a single peak in the weakly coupled case (top) and a split peak for the strong coupling regime (bottom, reproduced from Figure 7.7). (b) corresponding tuning map with A exciton line indicated (white dashed line)

polarisation selection rules for high angles (z, s_{02}) and normal incidence (x, s_{11}). The calculated near-field of these modes is shown in Figure 7.4 e,f) respectively.

Exciton Coherence Diameter and Mode Coupling

In 2D materials excitons are spatially more delocalized in comparison to excitons in molecules[21] which can be treated as point dipole emitters. In the former case the symmetry of the optical field plays a crucial role in the light-emitter coupling. The exciton coherence diameter d_c is given by[201]:

$$d_c = 8\hbar\sqrt{\frac{\pi}{M\Delta}} \tag{7.3}$$

with the total exciton mass $M = m_e^* + m_h^* = 0.63m_e$[202] and the exciton homogeneous spectral linewidth at room temperature Δ=40 meV[198] which results in d_c = 24 nm for WSe_2. Considering the coherence diameter and the field distribution of the s_{11} mode (Figure 7.9 b), inset), it becomes evident that s_{11} is suppressed. Dipoles at distances smaller than 24 nm apart would be driven with opposite phase within the same excitation as the s_{11} mode has a nodal point in the middle and the phase of the electric field changes from plus to minus. However, the s_{02} mode shows no nodal point in the near-field; therefore, excitons within the coherence diameter are driven with the same phase.

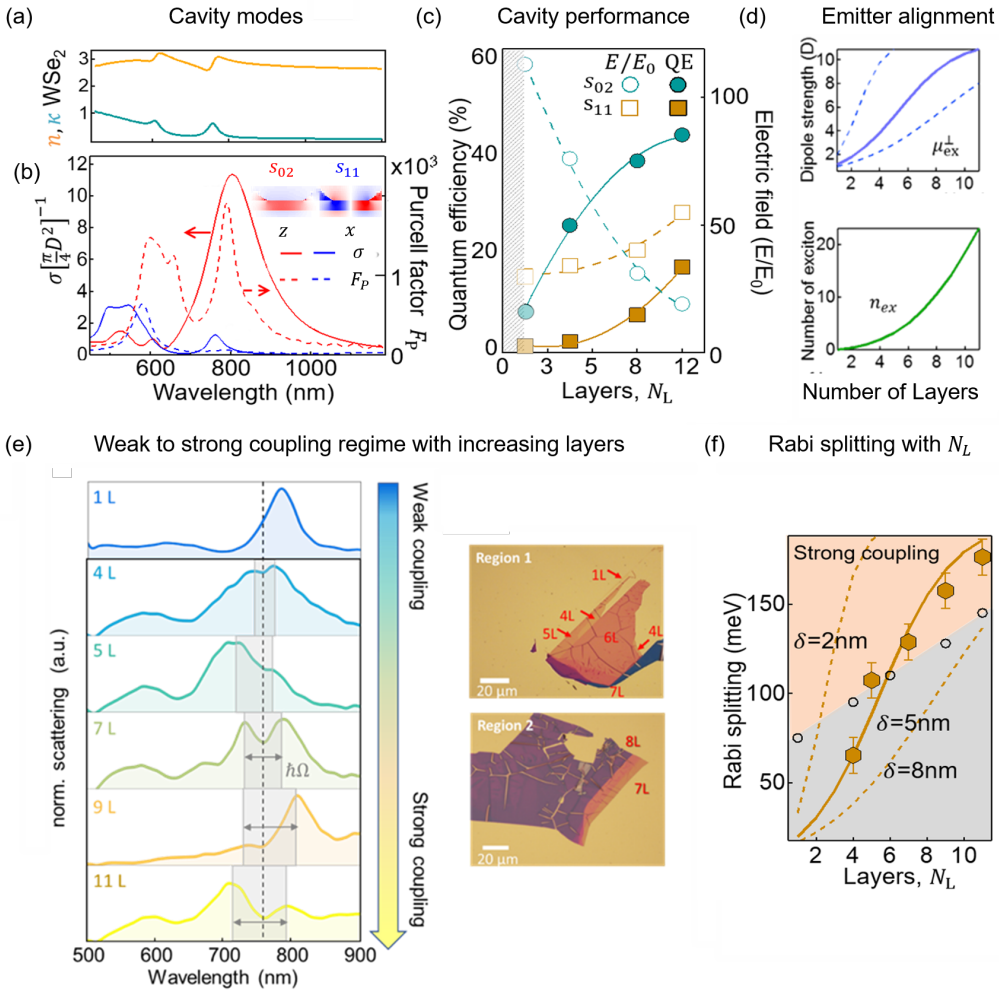

Figure 7.9: **Quantum efficiency and coupling strength as function of layer number**. (a) Effective refractive index $n+i\kappa$ of 12 layers WSe_2. (b) FDTD simulations of the scattering cross section (solid lines) and Purcell factors (dashed) for optical fields along normal (z, red) and in-plane (x, blue) directions. (c) Quantum efficiency (solid lines) and field enhancement (dashed) vs number of monolayers, when keeping s_{02}, s_{11} tuned to A exciton by changing the NP diameter. (d) Analytically calculated z-dipole strength (in Debye) of exciton with increasing N_L for different interlayer coupling lengths δ (solid line 5 nm, dashed 2 nm and 8 nm), maximum dipole contribution is 20% of total exciton strength. (d) Calculated number of excitons within the mode volume. (e) Measured dark-field scattering spectra for NPoMs for different numbers N_L showing clear splittings for $N_L \geq 7$ (different number of layers shown in BF images to the right). (f) Rabi splitting for NPoMs containing different numbers of WSe_2 layers, with fit to model (orange line, see text) depending on exciton interlayer coupling length δ. Black circles are the measured plasmon linewidths (NPoM size changed to retain exciton resonance). The strong coupling regime is shaded orange.

Thus, despite its field orientation along z the s_02 mode is dominating the interaction with the delocalized excitons due to its symmetry.This is further underlined by the calculated Purcell factor plotted in the same graph (Figure 7.9). The large Purcell factor of $F_P \propto$ 2000 near 800 nm confirms sufficient reduction of the K, K' exciton liftimes, thus strong coupling can occur before intra-valley scattering takes place. However, this is not the case for the s_{11} mode. The E_x field strength aligned to the dominant in-plane exciton [193] dipole

orientation are insufficient to retrieve strong coupling. This suggest that the excitons in multi layers have an out-of-plane component coupling to the s_{02} mode. The exciton dipole strength along z can be estimated by taking into account dipole-dipole interactions in multi layers and using the in-plane refractive index $n_x(\lambda)$(which is constrained by fitting the reflectivity of the flake away from NPoMs). The resulting z dipole strength is on the order of 25% of the in-plane component and therefore sufficiently large to reach strong-coupling (Figure 7.9 d). The occurrence of such multilayer-induced mixing can have different origins and has previously been reported using polarisation-dependent in-plane and out-of-plane reflectivity and scattering measurements[193,203,204]. In that context the good agreement of the measured SERS phonon lines with the literature suggests that stress-induced mixing can be ruled out since the lines remain unshifted.

7.6 Layer Dependence and Coupling Efficiency

The lack of strong coupling for monolayers suggests that several factors favour strong coupling in plasmonic cavities for thicker flakes. To gain insight in the optimal number of layers to achieve strong coupling in the NPoM configuration, the quantum efficiency and the field enhancement for different number of layers is calculated (Figure 7.9 c). The plasmon resonance is tuned by reducing the nanoparticle size to match the exciton resonance for fewer WSe_2 layers. Although fewer layers yield a higher quantum efficiency smaller nanoparticles result in smaller field enhancement. Thus, the optimal number of WSe_2 layers is a trade-off and depends on the largest field strength that can be obtained while tuning the lowest plasmon mode into exciton resonance (Figure 7.9 c). This is confirmed experimentally by drop casting larger NPs on thicker multilayers with larger gap sizes, which increases the radiative coupling and the plasmon linewidth κ (grey circles, Figure 7.9 f). Figure 7.9 e,f) show that the Rabi splitting for thicker WSe_2 layers increases, while a clear splitting is only resolved for layers $N_L \geq 5$ (Figure 7.9 e). For larger plasmon linewidths, the strong coupling threshold increases, resulting in a restricted region (orange, Figure 7.9 f), where strong coupling is possible. Considering interlayer dipole-dipole coupling an increasing out-of-plane exciton dipole contribution from $\mu_z = 0$ to 20% can be calculated. When allowing for different vertical coupling distances in multilayers, best agreement with the experimental data is found for delocalized excitons with interlayer coupling distances of 5 nm (solid line, Figure 7.9 f). This corresponds to typical 3D Bohr radii while the 2D exciton in plane radius is expected to be on the order of 1.5 nm.

In the limit of the monolayer it becomes evident that the exciton dipole is entirely in-plane. As a result, they do not couple with the plasmon cavity as the field-enhancement

is for out of plane (E_z). This is not the case for plasmon lattice modes or single nanoparticle rods, which have plasmonic modes allowing for coupling to E_x [183]. However, these modes are less confined and have much larger mode volumes, thus they require coupling to many excitons.
Another reason preventing strong coupling for monolayers NPoM constructs is the character of the plasmonic modes. Smaller gaps realized by single monolayers typically have the fundamental plasmon resonance shifted beyond the exciton into the IR. On the other hand, the higher-order plasmon modes in the visible range possess oscillatory fields in the gap that cannot couple to the delocalised exciton because of destructive interference. This can be counteracted by incorporating monolayers in other materials such as hexagonal boron nitride (hBN). These sandwiched layers form wider plasmon gaps and tune the lowest-energy plasmon back to the exciton resonance [38]. However, in that case the larger cavity volume needs to contain enough exciton oscillator strength to reach strong coupling. For WSe_2 constructs of N_L=7, the exciton Bohr radius indicates there are only 5 non-overlapping excitons (Figure 7.9 d), indicating exciting prospects for exciton nonlinearities. The extreme confinement within the plasmonic cavity here, thus offers a promising system for nonlinear devices.

7.7 Conclusion

In this chapter the latest progress of room temperature plasmonic resonators in the strong coupling regime was summarized. Using WSe_2 NPoM constructs it was successfully shown how ultra-compact plasmonic resonators in combination with TMDs are capable of reaching the strong coupling regime at room temperature with Rabi-splittings exceeding $\Omega_R > 140$ meV. Three parameters have been proven to be crucial:

- The coherence size of the delocalized exciton compared to the plasmonic mode typically prohibits coupling to higher order oscillatory modes.
- With increasing layer thickness the out-of-plane exciton dipole component increases by 25% compared to the monolayer case where this is purely in-plane oriented.
- Careful choice of nanoparticle size and UV laser irradiation enable tuning of the plasmon resonance for optimal coupling with different number of layers, and proves the dispersive nature of the hybrid system.

The optimal number of WSe_2 layers depends on the largest field strength that can be obtained while tuning the lowest plasmon mode into exciton resonance. Despite the indirect transition in multilayers, a drastic Purcell enhancement from the plasmonic cavity is found, which dominates over carrier scattering and phonon-driven intervalley transfer rates. Finally, the simple tuneability of the NPoM geometry allows for optimal coupling in extremely compact cavities with ultrasmall mode volumes.

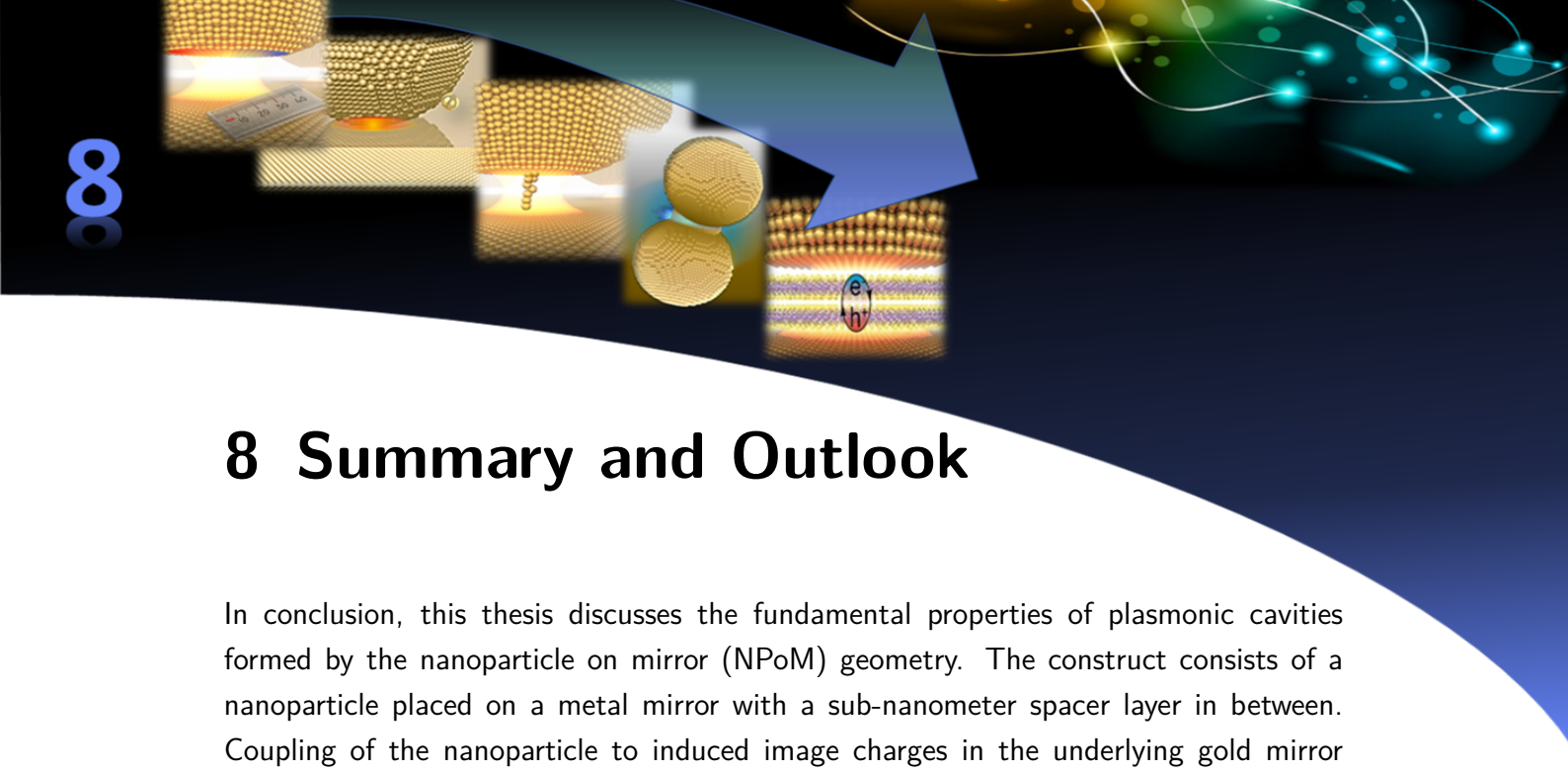

8 Summary and Outlook

In conclusion, this thesis discusses the fundamental properties of plasmonic cavities formed by the nanoparticle on mirror (NPoM) geometry. The construct consists of a nanoparticle placed on a metal mirror with a sub-nanometer spacer layer in between. Coupling of the nanoparticle to induced image charges in the underlying gold mirror creates a plasmonic dimer-like structure with a cavity enclosed in the gap.

As part of this thesis a polarization dark-field microscope has been developed to probe plasmonic nanostructures with atomistic resolution and in real time. The influence of cavity morphology, surrounding environment and spacer material were investigated experimentally. Full automation and variable dark-field configurations were used to determine the correlation of faceting and eccentricity to the optical response of the NPoM system. It was found that spherical nanoparticles are highly faceted, which determines the scattering behaviour for narrow gaps ($<$1 nm). Comparing the findings to boundary element simulations (BEM) two sets of plasmonic modes were identified: tightly confined cavity modes and radiative antenna modes. Mixing of these modes leads to a complex interplay of cavity morphology and plasmonic coupling that shape the optical response of the system. Investigating many NPoMs as a function of incident polarization, a splitting in the spectral response was correlated with the eccentricity and orientation of the nanocavity. While usually hidden under the nanoparticle and inaccessible for conventional, invasive imaging techniques such as SEM and TEM, polarization dependent dark-field scattering demonstrates a dramatic sensitivity to the cavity morphology with spectral shifts of λ=3 nm resulting from morphological changes in the order of a single atom.

Based upon the high sensitivity to atomic scale modifications of the cavity morphology, non-reversible, light-induced reconstruction was demonstrated and monitored in real-time. Ultraviolet (UV) laser irradiation was used to mobilize gold atoms on the nanoparticle surface which re-shape the plasmonic cavity. Studying different spacer materials, experimentally and theoretically, two regimes were identified: a regime of facet growth, which is typically seen for "hard spacers", such as WSe_2 and a conductive bridging regime, which occurs for molecular "soft spacers" such as CB[7] and TPT. For hard

spacers the cavity and spacer material remain intact during irradiation. Solely the growth of the bottom facets results in a red-shift of the plasmonic modes. In contrast, conductive filaments penetrate the soft spacers during irradiation, which shorts the gap. These conductive bridges are accompanied by rapid blue shifts in the spectral response of the NPoM construct marking the different stages for bridging. Laser power series show that the bridging dynamics are highly dependent on incident power. However, the final state is determined by the equilibrium wedge angle at the cusp between the bridge and the facet edge.

In the last part the drastic field enhancement (up to 10^4) in combination with the small mode volumes (as small as 40 nm^3) of plasmonic cavities are exploited to boost light-matter interaction at the nanoscale. Combining the high sensitivity and tuneability of the NPoM cavity it was successfully demonstrated how ultra-compact plasmonic resonators with sandwiched stacks of atomically thin WSe_2 layers are capable of reaching the strong coupling regime at room temperature. Tuning the plasmon resonance over the A exciton resonance of WSe_2 reveals the dispersive nature of the hybrid states with the characteristic anti-crossing and a Rabi-splittings exceeding $\Omega_R > 140$ meV. Despite the expected indirect transition in multilayers of WSe_2, it was found that the drastic Purcell enhancement of the plasmonic cavity dominates over carrier scattering and phonon-driven intervalley transfers.

The ability to control and enhance light-matter interaction on the nanoscale holds exciting new perspectives. The large field enhancement in combination with small mode volumes render the NPoM an ideal platform to study chemistry and quantum phenomena at the single molecule and emitter level[21]. In particular tracking redox reactions in real time and shedding light on the complex mechanisms of catalytic reactions shows great potential. Here, the combination with 2D materials, where defects in the sheets are known to act as active sites[48,205] would allow the creation of a controlled environment for "nanoreactors".

Furthermore, apart from their excellent catalytic properties atomically thin materials offer unique optical properties and stable excitons at room temperature that require further investigation. The ability to selectively enhance direct transitions even for multilayer stacks offers great opportunities for realistic excitonic devices and the possibility to investigate quantum phenomena at room temperature. Electrically gating the NPoM cavity[206] using 2D materials as gap material as well as electrodes exploits their great conductive properties as well as exciton transport in nanophotonic systems[28]. Another

exciting future direction is the promise of highly non-linear optical properties predicted at those scales. Non-linear processes such as SHG, four-wave mixing and photon-blockade are promoted by large field enhancement and likely to exhibit even more interesting behaviour in the strongly coupled regime. Finally, the combination of chiral plasmonics and spin-valley dynamics of TMDs is an interesting recipe for a nanophotonic platform transferring solid-state spin into optical information[178].

The tuneability and high responsivity of the NPoM system render it a sensitive platform to track nanometric changes with atomistic resolution and in real-time. Furthermore, the ability to manipulate nano-objects selectively and tune their optical properties hold great promise. For example, resonantly reshaping individual nanostructures by a tunable incident laser, could enable self-controlled reshaping, where the process is terminated as soon as the plasmon resonance is shifted out of resonance. Another promising example would be polarization selective growth that facilitates directional reshaping of plasmonic nanostructures. Furthermore, initial results have shown a reversible switching behaviour during UV-laser irradiation on very fast time scales ($>$40MHz) showing great potential for all-optical switches.

However, many questions encountered during my PhD have remained unanswered and require further attention in the pursuit of promising future directions. To selectively manipulate nano-objects it is crucial to understand and disentangle the contributions of various forces acting at such small length scales. This is complicated by the fact that strong electromagnetic fields not only lead to optical forces, but can also cause strong thermal forces. Furthermore, van-der-Waals forces and surface charges, as well as the gold binding to the linker molecules, play an important role at these scales. At strongly bonded interfaces, sufficient hybridization of atomic orbitals exists to permit carrier delocalization and therefore charge transfer across the interface[63]. This is not the case for materials interacting solely through van-der-Waals forces like 2D materials, where the atomic and molecular orbitals on the surface and edges are completely saturated, and thus the orbitals at the interface do not undergo hybridization. Understanding and controlling the complicated landscape of charges and forces acting on those scales with different spacer materials evolved will be the challenge and joy of future PhD students.

Bibliography

[1] W. Demtroder. *Experimentalphysik 2*. Springer Berlin Heidelberg, 2007.

[2] S. Maier. *Plasmonics Fundamentals and Applications*. Springer, 2007.

[3] L. Novotny and B. Hecht. *Principles of Nano-Optics*. Cambridge University Press, 2007.

[4] P. B. Johnson and R. W. Christy. Optical constants of the noble metals, 1972.

[5] J. Heckmann, M.-E. Kleemann, N. B. Grosse, and U. Woggon. The dual annihilation of a surface plasmon and a photon by virtue of a three-wave mixing interaction. *Opt. Express*, 21(23), 2013.

[6] E. Ringe, M. R. Langille, K. Sohn, J. Zhang, J. Huang, C.A. Mirkin, R. P. Van Duyne, and L. D. Marks. Plasmon Length: A Universal Parameter to Describe Size Effects in Gold Nanoparticles. *J. Phys. Chem. Lett.*, 3(11), 2012.

[7] C. Deeb, X Zhou, J. Plain, G. P. Wiederrecht, R. Bachelot, M. Russell, and P. K. Jain. Size Dependence of the Plasmonic Near-Field Measured via Single-Nanoparticle Photoimaging. *J. Phys. Chem. C*, 117(20), 2013.

[8] G. Baffou and R. Quidant. Nanoplasmonics for chemistry. *Chem. Soc. Rev.*, 43 (11), 2014.

[9] Teri W. Odom and George C. Schatz. Introduction to Plasmonics. *Chem. Rev.*, 111(6), 2011.

[10] J. N. Anker, W. P. Hall, O. Lyandres, N. C. Shah, J. Zhao, and R. P. Van Duyne. Biosensing with plasmonic nanosensors. *Nat. Mater.*, 7(6), 2008.

[11] A. J. Haes, C. L. Haynes, A. D. McFarland, G. C. Schatz, R. P. Van Duyne, and S. Zou. Plasmonic Materials for Surface-Enhanced Sensing and Spectroscopy. *MRS Bull.*, 30(05), 2005.

[12] D. Jin, P. Xi, B. Wang, L. Zhang, J. Enderlein, and A. M. van Oijen. Nanoparticles for super-resolution microscopy and single-molecule tracking. *Nat. Methods*, 15 (6), 2018.

[13] W. Li. Physics Models of Plasmonics: Single Nanoparticle, Complex Single Nanoparticle, Nanodimer, and Single Nanoparticle over Metallic Thin Film. *Plasmonics*, 13(3), 2018.

[14] P. Nordlander and E. Prodan. Plasmon hybridization in nanoparticles near metallic surfaces. *Nano Lett.*, 4(11), 2004.

[15] E. Prodan. A Hybridization Model for the Plasmon Response of Complex Nanostructures. *Science*, 302(5644), 2003.

[16] S.-C. Yang, H. Kobori, C.-L. He, M.-H. Lin, H.-Y. Chen, C. Li, M. Kanehara, T. Teranishi, and S. Gwo. Plasmon Hybridization in Individual Gold Nanocrystal Dimers: Direct Observation of Bright and Dark Modes. *Nano Lett.*, 10(2), 2010.

[17] P. K. Jain, W. Huang, and M. A. El-Sayed. On the universal scaling behavior of the distance decay of plasmon coupling in metal nanoparticle pairs: A plasmon ruler equation. *Nano Lett.*, 7(7), 2007.

[18] X. Ben and H. S. Park. Size Dependence of the Plasmon Ruler Equation for Two-Dimensional Metal Nanosphere Arrays. *J. Phys. Chem. C*, 115(32), 2011.

[19] W. Zhu, R. Esteban, A. G. Borisov, J. J. Baumberg, P. Nordlander, H. J. Lezec, J. Aizpurua, and K. B. Crozier. Quantum mechanical effects in plasmonic structures with subnanometre gaps. *Nat. Commun.*, 7, 2016.

[20] H. Cha, D. Lee, J. H. Yoon, and S. Yoon. Plasmon coupling between silver nanoparticles: Transition from the classical to the quantum regime. *J. Colloid Interface Sci.*, 464, 2016.

[21] R. Chikkaraddy, B. De Nijs, F. Benz, S. J. Barrow, O. A. Scherman, E. Rosta, A. Demetriadou, P. Fox, O. Hess, and J. J. Baumberg. Single-molecule strong coupling at room temperature in plasmonic nanocavities. *Nature*, 535(7610), 2016.

[22] K. J. Vahala. Optical microcavities. *Nature*, 424(6950), 2003.

[23] T. Volz, A. Reinhard, M. Winger, A. Badolato, K. J. Hennessy, E. L. Hu, and A. Imamoglu. Ultrafast all-optical switching by single photons. *Nat. Photonics*, 6 (9), 2012.

[24] S. Sanvitto, D. Këna-Cohen. The road towards polaritonic devices. *Nat. Mater.*, 15(10), 2016.

[25] J. A. Hutchison, T. Schwartz, C. Genet, E. Devaux, and T. W. Ebbesen. Modifying Chemical Landscapes by Coupling to Vacuum Fields. *Angew. Chemie Int. Ed.*, 51 (7), 2012.

[26] J. T. Hugall, A. Singh, and N. F. van Hulst. Plasmonic Cavity Coupling. *ACS Photonics*, 5(1), 2018.

[27] Z.-J. Yang, T. J. Antosiewicz, and T. Shegai. Role of material loss and mode volume of plasmonic nanocavities for strong plasmon-exciton interactions. *Opt. Express*, 24(18), 2016.

[28] D. G. Baranov, M. Wersaell, J. Cuadra, T. J. Antosiewicz, and T. Shegai. Novel Nanostructures and Materials for Strong Light-Matter Interactions. *ACS Photonics*, 5(1), 2018.

[29] A. Boca, R. Miller, K. M. Birnbaum, A. D. Boozer, J. McKeever, and H. J. Kimble. Observation of the Vacuum Rabi Spectrum for One Trapped Atom. *Phys. Rev. Lett.*, 93(23), 2004.

[30] N. Kongsuwan, A. Demetriadou, R. Chikkaraddy, F. Benz, V. A Turek, U. F Keyser, J. J Baumberg, and O. Hess. Suppressed Quenching and Strong-Coupling of Purcell-Enhanced Single-Molecule Emission in Plasmonic Nanocavities. *ACS Photonics*, 5(1), 2018.

[31] P. Törmä, W. L. Barnes, H.K. Drexhage, and et Al. Strong coupling between surface plasmon polaritons and emitters: a review. *Rep. Prog. Phys.*, 78(1), 2015.

[32] R. Jurga, S. D'Agostino, F. Della Sala, and C. Ciracì. Plasmonic Nonlocal Response Effects on Dipole Decay Dynamics in the Weak- and Strong-Coupling Regimes. *J. Phys. Chem. C*, 121(40), 2017.

[33] G. M. Akselrod, C. Argyropoulos, T. B. Hoang, C. Ciracì, C. Fang, J. Huang, D. R. Smith, and M. H. Mikkelsen. Probing the mechanisms of large Purcell enhancement in plasmonic nanoantennas. *Nat. Photonics*, 8(11), 2014.

[34] D. S. Dovzhenko, S. V. Ryabchuk, Yu. P. Rakovich, and I. R. Nabiev. Light-matter interaction in the strong coupling regime: configurations, conditions, and applications. *Nanoscale*, 10(8), 2018.

[35] L. Novotny. Strong coupling, energy splitting, and level crossings: A classical perspective. *Am. J. Phys.*, 78(11), 2010.

[36] R. Thomas, A. Thomas, S. Pullanchery, L. Joseph, S. M. Somasundaran, R. S. Swathi, S. K. Gray, and K. G. Thomas. Plexcitons: The Role of Oscillator Strengths and Spectral Widths in Determining Strong Coupling. *ACS Nano*, 12 (1), 2018.

[37] C. Sauvan, J. P. Hugonin, I. S. Maksymov, and P. Lalanne. Theory of the spontaneous optical emission of nanosize photonic and plasmon resonators. *Phys. Rev. Lett.*, 110(23), 2013.

[38] G. M. Akselrod, T. Ming, C. Argyropoulos, T. B. Hoang, Y. Lin, X. Ling, D. R. Smith, J. Kong, and M. H. Mikkelsen. Leveraging Nanocavity Harmonics for Control of Optical Processes in 2D Semiconductors. *Nano Lett.*, 15(5), 2015.

[39] J. Mertens, M.-E. Kleemann, R. Chikkaraddy, Prineha Narang, and J. J. Baumberg. How Light Is Emitted by Plasmonic Metals. *Nano Lett.*, 17(4), 2017.

[40] R. Chikkaraddy, V. A. Turek, N. Kongsuwan, F. Benz, C. Carnegie, T. van de Goor, B. de Nijs, A. Demetriadou, O. Hess, U. F. Keyser, and J. J. Baumberg. Mapping Nanoscale Hotspots with Single-Molecule Emitters Assembled into Plasmonic Nanocavities Using DNA Origami. *Nano Lett.*, 18(1), 2018.

[41] F. Benz, B. de Nijs, C. Tserkezis, Rohit Chikkaraddy, D. O. Sigle, L. Pukenas, S. D. Evans, J. Aizpurua, and J. J. Baumberg. Generalized circuit model for coupled plasmonic systems. *Opt. Express*, 23(26), 2015.

[42] URL `https://cen.acs.org/articles/95/i22/2-D-world.html`.

[43] A. K. Geim and I. V. Grigorieva. Van der Waals heterostructures. *Nature*, 499 (7459), 2014.

[44] P. R. Wallace. The Band Theory of Graphite. *Phys. Rev.*, 71(9), 1947.

[45] K. S. Novoselov, A. Mishchenko, A. Carvalho, and A. H. Castro Neto. 2D materials and van der Waals heterostructures. *Science*, 353(6298), 2016.

[46] S. Manzeli, D. Ovchinnikov, D. Pasquier, O. V. Yazyev, and A. Kis. 2D transition metal dichalcogenides. *Nat. Rev. Mater.*, 2(8), 2017.

[47] A. Castellanos-Gomez. Why all the fuss about 2D semiconductors? *Nat. Photonics*, 10(4):202–204, 2016.

[48] M. Chhowalla, H. S. Shin, G. Eda, L. J. Li, K. P. Loh, and H. Zhang. The chemistry of two-dimensional layered transition metal dichalcogenide nanosheets. *Nat. Chem.*, 5(4), 2013.

[49] Q. H. Wang, K. Kalantar-Zadeh, A. Kis, J.N. Coleman, and M. S. Strano. Electronics and optoelectronics of two-dimensional transition metal dichalcogenides. *Nat. Nanotechnol.*, 7(11), 2012.

[50] K. Fai Mak and J. Shan. Photonics and optoelectronics of 2D semiconductor transition metal dichalcogenides. *Nat. Photonics*, 10(4), 2016.

[51] W. Zhao, R. M. Ribeiro, M. Toh, A. Carvalho, C. Kloc, A. H. Castro Neto, and G. Eda. Origin of Indirect Optical Transitions in Few-Layer MoS_2 , WS_2 , and WSe_2. *Nano Lett.*, 13(11), 2013.

[52] P. Liu and B. Xiang. 2D hetero-structures based on transition metal dichalcogenides: fabrication, properties and applications. *Sci. Bull.*, 62(16), 2017.

[53] K. S. Novoselov, V. I. Falko, L. Colombo, P. R. Gellert, M. G. Schwab, and K. Kim. A roadmap for graphene. *Nature*, 490(7419), 2012.

[54] L. K. Tan, B. Liu, J. H. Teng, S. Guo, H. Y. Low, and K. P. Loh. Atomic layer deposition of a MoS_2 film. *Nanoscale*, 6(18), 2014.

[55] A. Splendiani, L. Sun, Y. Zhang, T. Li, J. Kim, C.-Y. Chim, G. Galli, and F. Wang. Emerging Photoluminescence in Monolayer MoS_2. *Nano Lett.*, 10(4), 2010.

[56] Ar. Raja, A. Chaves, J. Yu, G. Arefe, H. M. Hill, A. F. Rigosi, T. C. Berkelbach, P. Nagler, C. Schüller, T. Korn, C. Nuckolls, J. Hone, L. E. Brus, T. F. Heinz, D. R. Reichman, and A. Chernikov. Coulomb engineering of the bandgap and excitons in two-dimensional materials. *Nat. Commun.*, 8, 2017.

[57] K. Hao, J. F Specht, P. Nagler, L. Xu, K. Tran, A. Singh, C. K. Dass, C. Schüller, T. Korn, M. Richter, A. Knorr, X. Li, and G. Moody. Neutral and charged inter-valley biexcitons in monolayer $MoSe_2$. *Nat. Commun.*, 8, 2017.

[58] Z.-Wei Li, Y.-H. Hu, Y. Li, and Zh.-Y. F. Light-matter interaction of 2D materials: Physics and device applications. *Chinese Phys. B*, 26(3), 2017.

[59] H. Zeng, J. Dai, W. Yao, D. Xiao, and X. Cui. Valley polarization in MoS_2 monolayers by optical pumping. *Nat. Nanotechnol.*, 7(8), 2012.

[60] S. B. Desai, G. Seol, J. S. Kang, H. Fang, C. Battaglia, R. Kapadia, J. W. Ager, J. Guo, and A. Javey. Strain-Induced Indirect to Direct Bandgap Transition in Multilayer WSe_2. *Nano Lett.*, 14(8), 2014.

[61] P. Johari and V. B. Shenoy. Tuning the Electronic Properties of Semiconducting Transition Metal Dichalcogenides by Applying Mechanical Strains. *ACS Nano*, 6 (6), jun 2012.

[62] M. Kang, B. Kim, S. H. Ryu, S. W. Jung, J. Kim, L. Moreschini, C. Jozwiak, E. Rotenberg, A. Bostwick, and K. S. Kim. Universal Mechanism of Band-Gap Engineering in Transition-Metal Dichalcogenides. *Nano Lett.*, 17(3), 2017.

[63] D. Jariwala, T. J. Marks, and M. C. Hersam. Mixed-dimensional van der Waals heterostructures. *Nat. Mater.*, 16(2), 2017. ISSN 1476-1122.

[64] E. M. Alexeev, A. Catanzaro, O. V. Skrypka, P. K. Nayak, S. Ahn, S. Pak, J. Lee, J. Inn Sohn, K. S. Novoselov, H. S. Shin, and A. I. Tartakovskii. Imaging of Interlayer Coupling in van der Waals Heterostructures Using a Bright-Field Optical Microscope. *Nano Lett.*, 17(9), 2017.

[65] P. K. Jain, X. Huang, I. H. El-Sayed, and M. A. El-Sayed. Review of Some Interesting Surface Plasmon Resonance-enhanced Properties of Noble Metal Nanoparticles and Their Applications to Biosystems. *Plasmonics*, 2(3), 2007.

[66] R. Chikkaraddy, X. Zheng, F. Benz, L. J. Brooks, B. de Nijs, C. Carnegie, M. Kleemann, J. Mertens, R. W. Bowman, Guy A. E. Vandenbosch, V. V. Moshchalkov, and J. J. Baumberg. How Ultranarrow Gap Symmetries Control Plasmonic Nanocavity Modes: From Cubes to Spheres in the Nanoparticle-on-Mirror. *ACS Photonics*, 4(3), 2017.

[67] M. W Knight, J. Fan, F. Capasso, and N. J Halas. Influence of excitation and collection geometry on the dark field spectra of individual plasmonic nanostructures. *Opt. Express*, 18(3), 2010.

[68] K. Lindfors, T. Kalkbrenner, P. Stoller, and V. Sandoghdar. Detection and Spectroscopy of Gold Nanoparticles Using Supercontinuum White Light Confocal Microscopy. *Phys. Rev. Lett.*, 93(3), 2004.

[69] T. Stangner, H. Zhang, T. Dahlberg, K. Wiklund, and M. Andersson. Step-by-step guide to reduce spatial coherence of laser light using a rotating ground glass diffuser. *Appl. Opt.*, 56(19), 2017.

[70] R. Rottenfusser. Proper alignment of the microscope. *Methods Cell Biol.*, 114, 2013.

[71] Olympus. Reseach system Microscope BX51/BX61, 2018. URL `https://static1.olympus-lifescience.com/data/olympusmicro/brochures/pdfs/bx51motorized.pdf?rev=3DDC`.

[72] M.-E. Kleemann, R. Chikkaraddy, E. M. Alexeev, D. Kos, C. Carnegie, W. Deacon, A. Casalis De Pury, C. Große, B De Nijs, J. Mertens, A. I. Tartakovskii, and J. J. Baumberg. Strong-coupling of WSe_2 in ultra-compact plasmonic nanocavities at room temperature. *Nat. Commun.*, 8(1), 2017.

[73] U. Hohenester and A. Trueger. MNPBEM - A Matlab toolbox for the simulation of plasmonic nanoparticles. *Comput. Phys. Commun.*, 183(12), 2012.

[74] F J. Garcia de Abajo and A Howie. Retarded field calculation of electron energy loss in inhomogeneous dielectrics. *Phys. Rev. B*, 65(11), 2002.

[75] U. Hohenester. Simulating electron energy loss spectroscopy with the MNPBEM toolbox. *Comput. Phys. Commun.*, 185(3), 2014.

[76] J. Waxenegger, A. Trügler, and U. Hohenester. Plasmonics simulations with the MNPBEM toolbox: Consideration of substrates and layer structures. *Comput. Phys. Commun.*, 193, 2015.

[77] G.A.E. Vandenbosch and A.R. Van de Capelle. Mixed-potential integral expression formulation of the electric field in a stratified dielectric medium-application to the case of a probe current source. *IEEE Trans. Antennas Propag.*, 40(7), 1992.

[78] M.-E. Kleemann, J. Mertens, X. Zheng, S. Cormier, V. Turek, F. Benz, R. Chikkaraddy, W. Deacon, A. Lombardi, V. V. Moshchalkov, G. A.E. Vandenbosch, and J. J. Baumberg. Revealing Nanostructures through Plasmon Polarimetry. *ACS Nano*, 11(1), 2017.

[79] Felix Benz. *Few molecule vibrational Spectroscopy in Plasmonics.* 2016.

[80] R. G. Nuzzo and D. L. Allara. Adsorption of Bifunctional Organic Disulfides on Gold Surfaces. *J. Am. Chem. Soc.*, 105(13), 1983.

[81] R. Maoz and J. Sagiv. On the formation and structure of self-assembling monolayers. I. A comparative atr-wettability study of Langmuir-Blodgett and adsorbed films on flat substrates and glass microbeads. *J. Colloid Interface Sci.*, 100(2), 1984.

[82] F. Benz, R. Chikkaraddy, A. Salmon, H. Ohadi, B. de Nijs, J. Mertens, C. Carnegie, R. W. Bowman, and J. J. Baumberg. SERS of Individual Nanoparticles on a Mirror: Size Does Matter, but so Does Shape. *J. Phys. Chem. Lett.*, 7(12), 2016.

[83] T.-C. C. Lee and O. A. Scherman. Formation of dynamic aggregates in water by cucurbit[5]uril capped with gold nanoparticles. *Chem. Commun.*, 46(14), 2010.

[84] R. W. Taylor, T.-C. C. Lee, O. A. Scherman, R. Esteban, J. Aizpurua, F. M. Huang, J. J. Baumberg, and S. Mahajan. Precise subnanometer plasmonic junctions for SERS within gold nanoparticle assemblies using cucurbit[n]uril "glue". *ACS Nano*, 5(5), 2011.

[85] S.-Y. Ding, J. Yi, J.-F. Li, B. Ren, D.-Y. Wu, R. Panneerselvam, and Z.-Q. Tian. Nanostructure-based plasmon-enhanced Raman spectroscopy for surface analysis of materials. *Nat. Rev. Mater.*, 1(6), 2016.

[86] R. Zhang, Y. Zhang, Z. C. Dong, S. Jiang, C. Zhang, L. G. Chen, L. Zhang, Y. Liao, J. Aizpurua, Y. Luo, J. L. Yang, and J. G. Hou. Chemical mapping of a

single molecule by plasmon-enhanced Raman scattering. *Nature*, 498(7452), jun 2013.

[87] B. de Nijs, F. Benz, S. J. Barrow, D. O. Sigle, R. Chikkaraddy, A. Palma, C. Carnegie, M. Kamp, R. Sundararaman, P. Narang, O. A. Scherman, and J. J. Baumberg. Plasmonic tunnel junctions for single-molecule redox chemistry. *Nat. Commun.*, 8(1), 2017.

[88] H. Wei and H. Xu. Hot spots in different metal nanostructures for plasmon-enhanced Raman spectroscopy. *Nanoscale*, 83(21), 2013. ISSN 2040-3364.

[89] F. Hao, C. L. Nehl, J. H. Hafner, and P. Nordlander. Plasmon Resonances of a Gold Nanostar. *Nano Lett.*, 7(3), 2007.

[90] J. Xie, Q. Zhang, J. Y. Lee, and D. I. C. Wang. The Synthesis of SERS-Active Gold Nanoflower Tags for In Vivo Applications. *ACS Nano*, 2(12), 2008.

[91] X. Tian, Y. Zhou, S. Thota, S. Zou, and J. Zhao. Plasmonic Coupling in Single Silver Nanosphere Assemblies by Polarization-Dependent Dark-Field Scattering Spectroscopy. *jJ. Phys Chem. C*, 118(25), 2014.

[92] J. A. Fan, K. Bao, J. B. Lassiter, J. Bao, N. J. Halas, P. Nordlander, and F. Capasso. Near-Normal Incidence Dark-Field Microscopy: Applications to Nanoplasmonic Spectroscopy. *Nano Lett.*, 12(2817), 2012.

[93] L. O Herrmann, V. K. Valev, C. Tserkezis, J. S Barnard, S. Kasera, O. A Scherman, J. Aizpurua, and J. J Baumberg. Threading plasmonic nanoparticle strings with light. *Nat Commun*, 5, 2014.

[94] T. Maurer, P.-M. Adam, and G. Lévêque. Coupling between plasmonic films and nanostructures: from basics to applications. *Nanophotonics*, 4, 2015.

[95] K. J. Savage, M. M. Hawkeye, R. Esteban, A. G. Borisov, J. Aizpurua, and J. J. Baumberg. Revealing the quantum regime in tunnelling plasmonics. *Nature*, 491 (7425), 2012.

[96] S. Kim, J. Jin, Y.-J. Kim, I.-Y. Park, Y. Kim, and S.-W. Kim. High-harmonic generation by resonant plasmon field enhancement. *Nature*, 453(7196), 2008.

[97] N. Zohar, L. Chuntonov, and G. Haran. The simplest plasmonic molecules: Metal nanoparticle dimers and trimers. *J. Photochem. Photobiol. C Photochem. Rev.*, 21, 2014.

[98] D. Punj, R. Regmi, A. Devilez, R. Plauchu, S. B. Moparthi, B. Stout, N. Bonod, H. Rigneault, and J. Wenger. Self-Assembled Nanoparticle Dimer Antennas for Plasmonic-Enhanced Single-Molecule Fluorescence Detection at Micromolar Concentrations. *ACS Photonics*, 2(8), 2015.

[99] Zh. Nie, D. Fava, E. Kumacheva, S. Zou, G. C. Walker, and M. Rubinstein. Self-assembly of metal-polymer analogues of amphiphilic triblock copolymers. *Nat. Mater.*, 6(8), 2007.

[100] C. Sönnichsen, B. M. Reinhard, J. Liphardt, and A P. Alivisatos. A molecular ruler based on plasmon coupling of single gold and silver nanoparticles. *Nat. Biotechnol.*, 23(6), 2005.

[101] L. Novotny and N. van Hulst. Antennas for light. *Nat. Photonics*, 5(2), 2011.

[102] V. V. Thacker, L. O. Herrmann, D. O. Sigle, T. Zhang, T. Liedl, J. J. Baumberg, and U. F. Keyser. DNA origami based assembly of gold nanoparticle dimers for surface-enhanced Raman scattering. *Nat. Commun.*, 5(1), 2014.

[103] S. M Douglas, H. Dietz, T. Liedl, B. Hogberg, F. Graf, and W. M. Shih. Self-assembly of DNA into nanoscale three-dimensional shapes. *Nature*, 459(7245), 2009.

[104] Chunxiao Xi, Paula Facal Marina, Haibing Xia, and Dayang Wang. Directed self-assembly of gold nanoparticles into plasmonic chains. *Soft Matter*, 11(23), 2015.

[105] N. Hüsken, R. W. Taylor, D. Zigah, J. C. Taveau, O. Lambert, O. A. Scherman, J. J. Baumberg, and A. Kuhn. Electrokinetic assembly of one-dimensional nanoparticle chains with cucurbit[7]uril controlled subnanometer junctions. *Nano Lett.*, 13(12), 2013.

[106] N. Pazos-Perez, F. J. Garcia De Abajo, A. Fery, and R. A. Alvarez-Puebla. From nano to micro: Synthesis and optical properties of homogeneous spheroidal gold particles and their superlattices. *Langmuir*, 28(24), 2012.

[107] C. Hanske, M. Tebbe, C. Kuttner, V. Bieber, V. V Tsukruk, M. Chanana, T. A. F. Koenig, and A. Fery. Strongly Coupled Plasmonic Modes on Macroscopic Areas via Template-Assisted Colloidal Self-Assembly. *Nano Lett.*, 14(12), 2014.

[108] S. J. Barrow, A. M. Funston, D. E. Gómez, T.J. Davis, and P. Mulvaney. Surface Plasmon Resonances in Strongly Coupled Gold Nanosphere Chains from Monomer to Hexamer. *Nano Lett.*, 11(10), 2011.

[109] I Hussain M. et al. and Brust. Controlled step growth of molecularly linked gold nanoparticles: from metallic monomers to dimers to polymeric nanoparticle chains. *Langmuir*, 25(1934), 2009.

[110] B. de Nijs, R. W Bowman, L. O Herrmann, F. Benz, S. J. Barrow, J. Mertens, D. O. Sigle, R. Chikkaraddy, A. Eiden, A. Ferrari, O. A. Scherman, and J. J. Baumberg. Unfolding the contents of sub-nm plasmonic gaps using normalising plasmon resonance spectroscopy. *Faraday Discuss.*, 178, 2015.

[111] I. Romero, J. Aizpurua, G. W. Bryant, and F. J. García De Abajo. Plasmons in nearly touching metallic nanoparticles: singular response in the limit of touching dimers. *Opt. Express*, 14(21), 2006.

[112] M. Urbieta, M. Barbry, Y. Zhang, P. Koval, D. Sánchez-Portal, N. Zabala, and J. Aizpurua. Atomic-Scale Lightning Rod Effect in Plasmonic Picocavities: A Classical View to a Quantum Effect. *ACS Nano*, 12(1), 2018.

[113] G. Wulff. XXV. Zur Frage der Geschwindigkeit des Wachsthums und der Auflösung der Krystallflächen. *Zeitschrift für Kristallographie - Crystalline Materials*, 34(1-6), 1901.

[114] M. Grzelczak, J. Pérez-Juste, P. Mulvaney, and L. M. Liz-Marzán. Shape control in gold nanoparticle synthesis. *Chem. Soc. Rev.*, 37(9), 2008.

[115] C. Tserkezis, R. Esteban, D. O. Sigle, J. Mertens, L. O. Herrmann, J. J. Baumberg, and J. Aizpurua. Hybridization of plasmonic antenna and cavity modes: Extreme optics of nanoparticle-on-mirror nanogaps. *Phys. Rev. A - At. Mol. Opt. Phys.*, 92(5), 2015.

[116] D. O. Sigle, J. Mertens, L. O. Herrmann, R. W. Bowman, S. Ithurria, B. Dubertret, Y. Shi, H. Y. Yang, C. Tserkezis, J. Aizpurua, and J. J. Baumberg. Monitoring Morphological Changes in 2D Monolayer Semiconductors Using Atom-Thick Plasmonic Nanocavities. *ACS Nano*, 9(1), 2015.

[117] C.-Z. Huang, M.-J. Wu, and S.-Y. Chen. High Order Gap Modes of Film-Coupled Nanospheres. *J. Phys. Chem. C*, 119(24), 2015.

[118] J. Mertens, A. L. Eiden, D. O. Sigle, A. Huang, F.and Lombardo, Z. Sun, R. S. Sundaram, Al. Colli, C. Tserkezis, J. Aizpurua, S. Milana, A. C. Ferrari, and J. J. Baumberg. Controlling subnanometer gaps in plasmonic dimers using graphene. *Nano Lett.*, 13(11), 2013.

[119] J.-H. Huh, J. Lee, and S. Lee. Comparative Study of Plasmonic Resonances between the Roundest and Randomly Faceted Au Nanoparticles-on-Mirror Cavities. *ACS Photonics*, 5(2), 2017.

[120] Felix Benz, Mikolaj K Schmidt, Alexander Dreismann, Rohit Chikkaraddy, Yao Zhang, Angela Demetriadou, Cloudy Carnegie, Hamid Ohadi, Bart de Nijs, Ruben Esteban, Javier Aizpurua, and Jeremy J Baumberg. Single-molecule optomechanics in "picocavities". *Science*, 354(6313), 2016.

[121] M. J. Crow, K. Seekell, and A. Wax. Polarization mapping of nanoparticle plasmonic coupling. *Opt. Lett.*, 36(5), 2011.

[122] L. Black, Y. Wang, C. H. de Groot, A. Arbouet, and O. L. Muskens. Optimal Polarization Conversion in Coupled Dimer Plasmonic Nanoantennas for Metasurfaces. *ACS Nano*, 8(6), 2014.

[123] P. S. Popp, J. F. Herrmann, E.-C. Fritz, B. J. Ravoo, and C. Höppener. Impact of the Nanoscale Gap Morphology on the Plasmon Coupling in Asymmetric Nanoparticle Dimer Antennas. *Small*, 12(12), 2016.

[124] L. Weller, V. V. Thacker, L. O. Herrmann, E. A. Hemmig, A. Lombardi, U. F. Keyser, and J. J. Baumberg. Gap-Dependent Coupling of Ag-Au Nanoparticle Heterodimers Using DNA Origami-Based Self-Assembly. *ACS Photonics*, 3(9), 2016.

[125] R. Esteban, G. Aguirregabiria, A. G Borisov, Y. M. Wang, P. Nordlander, G. W. Bryant, and J. Aizpurua. The Morphology of Narrow Gaps Modifies the Plasmonic Response. *ACS Photonics*, 2(2), 2015.

[126] F. Benz, C. Tserkezis, L. O Herrmann, B. de Nijs, A. Sanders, D. O Sigle, L. Pukenas, S. D. Evans, J. Aizpurua, and J. J Baumberg. Nanooptics of Molecular-Shunted Plasmonic Nanojunctions. *Nano Lett.*, 15(1), 2015.

[127] E. Ringe, B. Sharma, A.-I. Henry, L. D. Marks, and R. P. Van Duyne. Single nanoparticle plasmonics. *Phys. Chem. Chem. Phys.*, 15(12), 2013.

[128] S. Y. Chen, J. J. Mock, R. T. Hill, A. Chilkoti, D. R. Smith, and A. A. Lazarides. Gold nanoparticles on polarizable surfaces as raman scattering antennas. *ACS Nano*, 4(11), 2010.

[129] D. Y. Lei, A. I. Fernández-Domínguez, Y. Sonnefraud, K. Appavoo, R. F. Haglund, J. B. Pendry, and S. A. Maier. Revealing Plasmonic Gap Modes in Particle-on-Film Systems Using Dark-Field Spectroscopy. *ACS Nano*, 6(2), 2012.

[130] J. J. Mock, Ryan T. Hill, A. Degiron, S. Zauscher, A. Chilkoti, and D. R. Smith. Distance-Dependent Plasmon Resonant Coupling between a Gold Nanoparticle and Gold Film. *Nano Lett.*, 8(8), 2008.

[131] L. Tong, H. Wei, S. Zhang, Z. Li, and H. Xu. Optical properties of single coupled plasmonic nanoparticles. *Phys. Chem. Chem. Phys.*, 15(12), 2013.

[132] N. Grillet, D. Manchon, F. Bertorelle, C. Bonnet, M. Broyer, E. Cottancin, J. Lermé, M. Hillenkamp, and M. Pellarin. Plasmon coupling in silver nanocube dimers: Resonance splitting induced by edge rounding. *ACS Nano*, 5(12), 2011.

[133] J. Mertens, A. Demetriadou, R. W. Bowman, F. Benz, M. E. Kleemann, C. Tserkezis, Y. Shi, H. Y. Yang, O. Hess, J. Aizpurua, and J. J. Baumberg. Tracking Optical Welding through Groove Modes in Plasmonic Nanocavities. *Nano Lett.*, 16(9), 2016.

[134] G.-C. Li, Y.-L. Zhang, and D. Y. Lei. Hybrid plasmonic gap modes in metal film-coupled dimers and their physical origins revealed by polarization resolved dark field spectroscopy. *Nanoscale*, 8(13), 2016.

[135] Q. Zhang, G.-C. Li, T. W. Lo, and D. Y. Lei. Polarization-resolved optical response of plasmonic particle-on-film nanocavities. *J. Opt.*, 20(2), 2018.

[136] T. Chen, M. Pourmand, A. Feizpour, B. Cushman, and B. M. Reinhard. Tailoring Plasmon Coupling in Self-Assembled One-Dimensional Au Nanoparticle Chains through Simultaneous Control of Size and Gap Separation. *J. Phys. Chem. Lett.*, 4(13), 2013.

[137] L. V. Brown, H. Sobhani, J. B. Lassiter, P. Nordlander, and N. J. Halas. Heterodimers: Plasmonic properties of mismatched nanoparticle pairs. *ACS Nano*, 4 (2), 2010.

[138] L. S. Slaughter, Y. W., B. A. Willingham, P. Nordlander, and S. Link. Effects of symmetry breaking and conductive contact on the plasmon coupling in gold nanorod dimers. *ACS Nano*, 4(8), 2010.

[139] O. Schubert, J. Becker, L. Carbone, Y. Khalavka, T. Provalska, I. Zins, and C. Sönnichsen. Mapping the polarization pattern of plasmon modes reveals nanoparticle symmetry. *Nano Lett.*, 8(8), 2008.

[140] A. C Bhasikuttan, H. Pal, and J. Mohanty. Cucurbit[n]uril based supramolecular assemblies: tunable physico-chemical properties and their prospects. *Chem. Commun.*, 47(36), 2011.

[141] L. Chuntonov and G. Haran. Trimeric plasmonic molecules: The role of symmetry. *Nano Lett.*, 11(6), 2011.

[142] P. R. Wiecha, L.-J. Black, Y. Wang, V. Paillard, C. Girard, O. L. Muskens, and A. Arbouet. Polarization conversion in plasmonic nanoantennas for metasurfaces using structural asymmetry and mode hybridization. *Sci. Rep.*, 7, 2017.

[143] S. Zhang and H. Xu. Tunable Dark Plasmon in Metallic Nanocube Dimer: Toward Ultimate Sensitivity Nanoplasmonic Sensors. *Nanoscale*, 8(28), 2016.

[144] H. Kang, B. Jia, and M. Gu. Polarization characterization in the focal volume of high numerical aperture objectives. *Opt. Express*, 18(10), 2010.

[145] R.F. Egerton, P. Li, and M. Malac. Radiation damage in the TEM and SEM. *Micron*, 35(6):399–409, 2004.

[146] G. Di Martino, S. Tappertzhofen, S. Hofmann, and J. J. Baumberg. Nanoscale Plasmon-Enhanced Spectroscopy in Memristive Switches. *Small*, 12(10), 2016.

[147] M. I Stockman, K. Kneipp, S. I Bozhevolnyi, S. Saha, A. Dutta, J. Ndukaife, N. Kinsey, H. L. Reddy, N. F. van Hulst, and M. F. et Al. Kling. Roadmap on plasmonics. *J. Opt.*, 20(4), 2018. ISSN 2040-8978.

[148] N. Kinsey, M. Ferrera, V. M. Shalaev, and A. Boltasseva. Examining nanophotonics for integrated hybrid systems: a review of plasmonic interconnects and modulators using traditional and alternative materials [Invited]. *J. Opt. Soc. Am. B*, 32(1), 2015.

[149] J. A. Schuller, E. S. Barnard, W. Cai, Y. C. Jun, J. S. White, and M. L. Brongersma. Plasmonics for extreme light concentration and manipulation. *Nat. Mater.*, 9(3), 2010.

[150] H. A. Atwater and A. Polman. Plasmonics for improved photovoltaic devices. *Nat. Mater.*, 9(3), 2010.

[151] S. V. Makarov, A. S. Zalogina, M. Tajik, D. A. Zuev, M. V. Rybin, A. A. Kuchmizhak, S. Juodkazis, and Y. Kivshar. Light-Induced Tuning and Reconfiguration of Nanophotonic Structures. *Laser Photon. Rev.*, 11(5), 2017.

[152] N. Large, M. Abb, J. Aizpurua, and O. L. Muskens. Photoconductively loaded plasmonic nanoantenna as building block for ultracompact optical switches. *Nano Lett.*, 10(5), 2010.

[153] M. Abb, P. Albella, J. Aizpurua, and O. L. Muskens. All-Optical Control of a Single Plasmonic Nanoantenna-ITO Hybrid. *Nano Lett.*, 11(6), 2011.

[154] C. Ciraci, R. T. Hill, J. J. Mock, Y. Urzhumov, a. I. Fernandez-Dominguez, S. a. Maier, J. B. Pendry, A. Chilkoti, and D. R. Smith. Probing the Ultimate Limits of Plasmonic Enhancement. *Science*, 337(6098), 2012.

[155] O. L. Muskens, V. Giannini, J. A. Sánchez-Gil, and J. Gómez Rivas. Strong Enhancement of the Radiative Decay Rate of Emitters by Single Plasmonic Nanoantennas. *Nano Lett.*, 7(9), 2007.

[156] W. Zhu and K. B. Crozier. Quantum mechanical limit to plasmonic enhancement as observed by surface-enhanced Raman scattering. *Nat Commun*, 5, 2014.

[157] D. Lee and S. Yoon. Effect of Nanogap Curvature on SERS: A Finite-Difference Time-Domain Study. *J. Phys. Chem. C*, 120(37), 2016.

[158] J. H. Yoon, F. Selbach, L. Langolf, and S. Schlücker. Ideal Dimers of Gold Nanospheres for Precision Plasmonics: Synthesis and Characterization at the Single-Particle Level for Identification of Higher Order Modes. *Small*, 14(4), 2018.

[159] H. Jung, H. Cha, D. Lee, and S. Yoon. Bridging the Nanogap with Light: Continuous Tuning of Plasmon Coupling between Gold Nanoparticles. *ACS Nano*, 9 (12), 2015.

[160] S. Lerch and B. M. Reinhard. Spectral signatures of charge transfer in assemblies of molecularly-linked plasmonic nanoparticles. *Int. J. Mod. Phys. B*, 31(24), 2017.

[161] Z. Wang, Z. Dong, Y.-H. Gu, Y.and Chang, L. Zhang, L.-J. Li, W. Zhao, G. Eda, W. Zhang, G. Grinblat, S. A. Maier, J. K. W. Yang, C.-W. Qiu, and A. T. S. Wee. Giant photoluminescence enhancement in tungsten-diselenide-gold plasmonic hybrid structures. *Nat. Commun.*, 7, 2016.

[162] K. Santhosh, O. Bitton, L. Chuntonov, G. Haran, K. Hennessy, C. Monroe, H. K. Lo, H. F. Chau, H. J. Kimble, P. B. Johnson, R. W. Christy, and A. F. et Al. Koenderink. Vacuum Rabi splitting in a plasmonic cavity at the single quantum emitter limit. *Nat. Commun.*, 7, 2016.

[163] J. Huang, G. M. Akselrod, T. Ming, J. Kong, and M. H. Mikkelsen. Tailored Emission Spectrum of 2D Semiconductors Using Plasmonic Nanocavities. *ACS Photonics*, 5(2), 2018.

[164] K. J. Russell, T.-L. Liu, S. Cui, and E. L. Hu. Large spontaneous emission enhancement in plasmonic nanocavities. *Nat. Photonics*, 6(7), 2012.

[165] A. E. Schlather, N. Large, A. S. Urban, P. Nordlander, and N. J. Halas. Near-Field Mediated Plexcitonic Coupling and Giant Rabi Splitting in Individual Metallic Dimers. *Nano Lett.*, 13(7), 2013.

[166] S. Savasta, R. Saija, A. Ridolfo, O. Di Stefano, P. Denti, and F. Borghese. Nanopolaritons: Vacuum Rabi Splitting with a Single Quantum Dot in the Center of a Dimer Nanoantenna. *ACS Nano*, 4(11), 2010.

[167] M. Ruggenthaler, N. Tancogne-Dejean, J. Flick, H. Appel, and A. Rubio. From a quantum-electrodynamical light-matter description to novel spectroscopies. *Nat. Rev. Chem.*, 2018.

[168] J. Kasprzak, M. Richard, S. Kundermann, A. Baas, P. Jeambrun, J. M. J. Keeling, F. M. Marchetti, M. H. Szymańska, R. André, J. L. Staehli, V. Savona, P. B. Littlewood, B. Deveaud, and Le Si Dang. Bose-Einstein condensation of exciton polaritons. *Nature*, 443(7110), 2006.

[169] G. Christmann, R. Butté, E. Feltin, J.-F. Carlin, and N. Grandjean. Room temperature polariton lasing in a GaN/AlGaN multiple quantum well microcavity. *Appl. Phys. Lett.*, 93(5), 2008.

[170] S. Wu, S. Buckley, J. R. Schaibley, L. Feng, J. Yan, Da. G. Mandrus, F. Hatami, W. Yao, J. Vučković, A.a Majumdar, and X. Xu. Monolayer semiconductor nanocavity lasers with ultralow thresholds. *Nature*, 520(7545), 2015.

[171] D. N. Basov, M. M. Fogler, and F. J. Garcia de Abajo. Polaritons in van der Waals materials. *Science*, 354(6309), 2016.

[172] T. Fryett, A. Zhan, and A. Majumdar. Review article Cavity nonlinear optics with layered materials. *Nanophotonics*, 7(2), 2017.

[173] P. Vasa and C.h Lienau. Strong Light-Matter Interaction in Quantum Emitter/Metal Hybrid Nanostructures. *ACS Photonics*, 5(1), 2018.

[174] T. Byrnes, N. Y. Kim, and Y. Yamamoto. Exciton-polariton condensates. *Nat. Phys.*, 10(11), 2014.

[175] J. Xiao, M. Zhao, Y. Wang, and X. Zhang. Excitons in atomically thin 2D semiconductors and their applications. *Nanophotonics*, 6(6), 2017.

[176] H. Zeng and X. Cui. An optical spectroscopic study on two-dimensional group-VI transition metal dichalcogenides. *Chem. Soc. Rev.*, 44(9), 2015.

[177] M. Palummo, M. Bernardi, and J. C. Grossman. Exciton radiative lifetimes in two-dimensional transition metal dichalcogenides. *Nano Lett.*, 15(5), 2015.

[178] S. Gong, F. Alpeggiani, B. Sciacca, E. C Garnett, and L. Kuipers. Nanoscale chiral valley-photon interface through optical spin-orbit coupling. *Science*, 359(6374), 2018.

[179] S Dufferwiel, S Schwarz, F Withers, A A P Trichet, F Li, M Sich, O Del Pozo-Zamudio, C Clark, A Nalitov, D D Solnyshkov, G Malpuech, K S Novoselov, J M Smith, M S Skolnick, D N Krizhanovskii, A I Tartakovskii, O Del Pozo-Zamudio, C Clark, A Nalitov, D D Solnyshkov, G Malpuech, K S Novoselov, J M Smith, M S Skolnick, D N Krizhanovskii, and A I Tartakovskii. Exciton-polaritons in van der Waals heterostructures embedded in tunable microcavities. *Nat. Commun.*, 6, 2015.

[180] N. Lundt, S. Klembt, E. Cherotchenko, S. Betzold, O. Iff, A. V Nalitov, M. Klaas, C. P Dietrich, A. V Kavokin, S. Höfling, and C. Schneider. Room-temperature Tamm-plasmon exciton-polaritons with a WSe_2 monolayer. *Nat. Commun.*, 7, 2016.

[181] L. C. Flatten, Z. He, D. M. Coles, A. A. P. Trichet, A. W. Powell, R. A. Taylor, J. H. Warner, and J. M. Smith. Room-temperature exciton-polaritons with two-dimensional WS_2. *Sci. Rep.*, 6(1), 2016.

[182] X. Liu, T. Galfsky, Z. Sun, F. Xia, E. Lin, Y.-H. Lee, S. Kéna-Cohen, and V. M. Menon. Strong light-matter coupling in two-dimensional atomic crystals. *Nat. Photonics*, 9(1), 2015.

[183] W. Liu, B. Lee, C. H. Naylor, H.-S. Ee, J. Park, A. T. C. J., and R. Agarwal. Strong Exciton-Plasmon Coupling in MoS_2 Coupled with Plasmonic Lattice. *Nano Lett.*, 16(2), 2016.

[184] J. Cuadra, D. G. Baranov, Ma. Wersäll, R. Verre, T. J. Antosiewicz, and T. Shegai. Observation of tunable charged exciton polaritons in hybrid monolayer WS_2 plasmonic nanoantenna system. *Nano Lett.*, 18(3), 2017.

[185] J. Wen, H. Wang, W. Wang, Z. Deng, C. Zhuang, Y. Zhang, F. Liu, J. She, J. Chen, H. Chen, S.i Deng, and N. Xu. Room-temperature vacuum Rabi splitting with active control in two-dimensional atomic crystals. *Nano Lett.*, 17(8), 2017.

[186] D. Zheng, S. Zhang, Q. Deng, M. Kang, P. Nordlander, and H. Xu. Manipulating coherent plasmon-exciton interaction in a single silver nanorod on monolayer WSe_2. *Nano Lett.*, 17(6), 2017.

[187] W. Zhao, S. Wang, B. Liu, I. Verzhbitskiy, S. Li, F. Giustiniano, D. Kozawa, K. P. Loh, K. Matsuda, K. Okamoto, R. F. Oulton, and G. Eda. Exciton-Plasmon Coupling and Electromagnetically Induced Transparency in Monolayer Semiconductors Hybridized with Ag Nanoparticles. *Adv. Mater.*, 28(14), 2016.

[188] A. J. Moilanen, T. K. Hakala, and P. Törmä. Actice Control of Surface PLasmon-Emitter Strong Coupling. *ACS Photonics*, 5(1), 2018.

[189] J. A. Schuller, S. Karaveli, T. Schiros, K. He, S. Yang, I. Kymissis, J. Shan, and R. Zia. Orientation of luminescent excitons in layered nanomaterials. *Nat. Nanotechnol.*, 8(4), 2013.

[190] Gülis Zengin, Göran Johansson, Peter Johansson, Tomasz J. Antosiewicz, Mikael Käll, and Timur Shegai. Approaching the strong coupling limit in single plasmonic nanorods interacting with J-aggregates. *Sci. Rep.*, 3, 2013.

[191] E.-M. Roller, C. Argyropoulos, A. Högele, T. L., and M. Pilo-Pais. Plasmon-Exciton Coupling Using DNA Templates. *Nano Lett.*, 16(9), 2016.

[192] D. Melnikau, R. Esteban, D. Savateeva, A. Sánchez-Iglesias, M. Grzelczak, M. K. Schmidt, L. M. Liz-Marzán, J. Aizpurua, and Y. P. Rakovich. Rabi Splitting in Photoluminescence Spectra of Hybrid Systems of Gold Nanorods and J-Aggregates. *J. Phys. Chem. Lett.*, 7(2), 2016.

[193] W. Y. Liang, A. R. Beal, H. P. Knights, J. Hughes, and S. C. Bayliss. Optical anisotropy in layer compounds. *J. Phys. C Solid State Phys*, 6(3), 1973.

[194] A. Arora, M. Koperski, K. Nogajewski, J. Marcus, C. Faugeras, and M. Potemski. Excitonic resonances in thin films of WSe_2: From monolayer to bulk material. *Nanoscale*, 7(23), 2015.

[195] S. Zhu, D. Li, Y.n Hu, J. Wang, X. Wang, and W. Lu. Enhancement of direct and indirect exciton emissions in few-layer WSe_2 at high temperatures. *Mater. Res. Express*, 5(6), 2018.

[196] Krishna P. Dhakal, Shrawan Roy, Houk Jang, Xiang Chen, Won Seok Yun, Hyunmin Kim, JaeDong Lee, Jeongyong Kim, and Jong-Hyun Ahn. Local Strain Induced Band Gap Modulation and Photoluminescence Enhancement of Multilayer Transition Metal Dichalcogenides. *Chem. Mater.*, 29(12):5124–5133, 2017.

[197] A. Kumar and P K Ahluwalia. Semiconductor to metal transition in bilayer transition metals dichalcogenides MX 2 (M = Mo, W; X = S, Se, Te). *Model. Simul. Mater. Sci. Eng.*, 21(6), 2013.

[198] M. Selig, G. Berghäuser, A. Raja, P. Nagler, C. Schüller, T. F. Heinz, T. Korn, A. Chernikov, E. Malic, and A. Knorr. Excitonic linewidth and coherence lifetime in monolayer transition metal dichalcogenides. *Nat. Commun.*, 7, 2016.

[199] A. Lombardi, A. Demetriadou, L. Weller, P. Andrae, F. Benz, R. Chikkaraddy, J. Aizpurua, and J. J. Baumberg. Anomalous Spectral Shift of Near- and Far-Field Plasmonic Resonances in Nanogaps. *ACS Photonics*, 3(3), 2016.

[200] J. A. Faucheaux, J. Fu, and P. K. Jain. Unified Theoretical Framework for Realizing Diverse Regimes of Strong Coupling between Plasmons and Electronic Transitions. *J. Phys. Chem. C*, 118(5), 2014.

[201] G. Peter, E. O. Gobel, P. Dawson, K. Moore, C. Foxon, and R. J. Elliott. Linewidth Dependence of Radiative Exciton Lifetimes in Quantum Wells. *Phys. Rev. Lett.*, 59(20), 1987.

[202] H. Shi, H. Pan, Y.-W. Zhang, and B. I. Yakobson. Quasiparticle band structures and optical properties of strained monolayer MoS_2 . *Phys. Rev. B*, 87(15), 2013.

[203] G. Wang, C. Robert, M. M. Glazov, F. Cadiz, E. Courtade, T. Amand, D. Lagarde, T. Taniguchi, K. Watanabe, B. Urbaszek, and X. Marie. In-Plane Propagation of Light in Transition Metal Dichalcogenide Monolayers: Optical Selection Rules. *Phys. Rev. Lett.*, 119(4), 2017.

[204] K. D. Park, T. Jiang, G. Clark, X. Xu, and M. B. Raschke. Radiative control of dark excitons at room temperature by nano-optical antenna-tip Purcell effect. *Nat. Nanotechnol.*, 13(1), 2018.

[205] D. Deng, K. S. Novoselov, Q. Fu, N. Zheng, Z. Tian, and X. Bao. Catalysis with two-dimensional materials and their heterostructures. *Nat. Nanotechnol.*, 11(3), 2016.

[206] C. Lumdee, S. Toroghi, and P. G. Kik. Post-fabrication voltage controlled resonance tuning of nanoscale plasmonic antennas. *ACS Nano*, 6(7), 2012.

[207] J. Fontana, N. Charipar, S. R. Flom, J. Naciri, A. Piqué, B. R. Ratna, A. Pique, and B. R. Ratna. Rise of the Charge Transfer Plasmon: Programmable Concatenation of Conductively Linked Gold Nanorod Dimers. *ACS Photonics*, 3(5), 2016.

[208] M. Grzelczak and L. M. Liz-Marzán. The relevance of light in the formation of colloidal metal nanoparticles. *Chem. Soc. Rev.*, 43(7), 2014.

[209] F. Herrera and F. C. Spano. Theory of Nanoscale Organic Cavities: The Essential Role of Vibration-Photon Dressed States. *ACS Photonics*, 5(1), 2018.

[210] H. Hu, H. Duan, J. K. W. Yang, and Z. X. Shen. Plasmon-Modulated Photoluminescence of Individual Gold Nanostructures. *ACS Nano*, 6(11), 2012.

[211] N. Jiang, X. Zhuo, and J. Wang. Active Plasmonics: Principles, Structures, and Applications. *Chem. Rev.*, 118(6), 2018.

[212] Y. Li, Z. Li, C. Chi, H. Shan, L. Zheng, and Z. Fang. Plasmonics of 2D Nanomaterials: Properties and Applications. *Adv. Sci.*, 4(8), 2017.